Winter 2016

Mineral Complexities as Evidence for Open-system Processes in Formation of Intermediate Magmas of the Mount Baker Volcanic Field, Northern Cascade Arc

Ricardo D. (Ricardo Daniel) Escobar-Burciaga
Western Washington University, escobarricardo89@gmail.com

MINERAL COMPLEXITIES AS EVIDENCE FOR OPEN-SYSTEM PROCESSES IN FORMATION OF INTERMEDIATE MAGMAS OF THE MOUNT BAKER VOLCANIC FIELD, NORTHERN CASCADE ARC

By

Ricardo Daniel Escobar-Burciaga

Accepted in Partial Completion
of the Requirements for the Degree
Master of Science
Geology

Kathleen L. Kitto, Dean of Graduate School

ADVISORY COMMITTEE

Chair, Dr. Susan M. DeBari

Dr. Rachel Teasdale

Dr. Jackie Caplan-Auerbach

Dave Tucker

MASTER'S THESIS

In presenting this thesis in partial fulfillment of the requirements for a master's degree at Western Washington University, I grant to Western Washington University the non-exclusive royalty-free right to archive, reproduce, distribute, and display the thesis in any and all forms, including electronic format, via any digital library mechanisms maintained by WWU.

I represent and warrant this is my original work, and does not infringe or violate any rights of others. I warrant that I have obtained written permissions from the owner of any third part copyrighted material included in these files.

I acknowledge that I retain ownership rights to the copyright of this work, including but not limited to the right to use all or part of this work in future works, such as articles or books.

Library users are granted permission for individual, research and non-commercial reproduction of this work for educational purposes only.

Any further digital posting of this document requires specific permission from the author. Any copying or publication of this thesis for commercial purposes, or for financial gain, is not allowed without my written permission.

Ricardo Daniel Escobar-Burciaga

February 18, 2016

MINERAL COMPLEXITIES AS EVIDENCE FOR OPEN-SYSTEM PROCESSES IN FORMATION OF INTERMEDIATE MAGMAS OF THE MOUNT BAKER VOLCANIC FIELD, NORTHERN CASCADE ARC

A Thesis
Presented to
The Faculty of
Western Washington University

In partial Fulfillment
Of the Requirements for the Degree
Master of Science

By
Ricardo Daniel Escobar-Burciaga
2016

Abstract

To better understand the complex history of open system differentiation in intermediate subduction zone magmas, complex crystal populations from andesites in the Mount Baker volcanic field (MBVF) in the northern Cascade arc were analyzed. Previous studies have suggested that open-system processes play a dominant role in the petrogenesis of these andesites; however, the studies relied heavily on bulk rock compositions and overlooked complex mineral textures and compositions. This study focuses on establishing mineral and crystal clot populations in four andesite flow units, from which co-crystallizing assemblages were identified. The flow units are the medium-K andesites of Swift Creek (*asw*; 55-56% SiO_2), Dobbs Creek (*ado*; 56-57% SiO_2), and Dobbs Cleaver (*adb*; 58-60% SiO_2), and the high-K andesite of Coleman Pinnacle (*acp*; 58-65% SiO_2).

Mineral compositions of co-crystallizing assemblages were used to identify their likely parental compositions and are labeled as follows: B (basalt to high-magnesium basaltic-andesite), BA (basaltic andesitic magmas), A (andesitic magmas) and D (dacitic magmas). The andesites of Swift Creek (~48 ka) and Dobbs Creek (~119 ka) both contain a mafic crystal assemblage (B1) that is nearest in equilibrium with the bulk rock Mg#, suggesting that the other, more differentiated, crystal assemblages (BA1, A1 and D1) come from incorporation of liquid-poor crystal mushes. The *asw* flow unit contains an additional mafic assemblage (B2), which is not present in the other flow units, and is interpreted to have been crystallized from the same or similar magma as the B1 assemblage; however, with a distinct crystallization history. The andesite of Dobbs Cleaver (~105 ka) contains the same B1, A1 and D1 crystal assemblages present in *asw* and *ado*; however, an additional, more liquid-rich magmatic component (BA2) is responsible for the higher SiO_2-content of the *adb* flow unit (evidenced from microscopic magma mingling textures). As a result, the native B1 assemblage in *adb* is slightly out of Mg-equilibrium with the bulk rock composition. The BA2 assemblage of *adb* is distinct from the BA1 assemblage of *asw* and *ado* in that it contains megacrystic phenocrysts and crystal clots. Across all the medium-K flow units, a B1, A1 and D1 assemblage are identified. The high-K, hornblende-bearing andesite of Coleman Pinnacle (~305 ka) hosts the BA3 crystal assemblage, unique to this flow unit, which is nearest in Mg-equilibrium to the bulk rock. The compositions of augites in the BA3 assemblage are more calcic-rich than all augites of the medium-K andesites, suggesting they crystallized from a distinct parental component. Despite a distinct parental component, the same felsic D1 crystal assemblage described above is also observed in the *acp* flow unit.

I interpret the crystal clots, present in all flow units, to represent cumulate material entrained in the erupting host magma and that related phenocrysts are disaggregates of crystal clots. The existence of common, multiple phenocryst and crystal clot populations in each flow unit of different age and SiO_2 content provides strong evidence that intermediate magmas of MBVF are a result of complex, open system processes involving passage through multiple crystal mushes. They are more than just the end product of mixing between two magmas. Furthermore, we suggest that most phenocrysts do *not* represent equilibrium products of their host liquid, evident from wide compositional ranges of ferromagnesian minerals (e.g., augite core Mg# 69-85). The most mafic phenocryst populations (B1 and B2 assemblages) show the least amount of disequilibrium textures. Given the fact that the SiO_2 content of the magmas are in the basaltic-andesite to andesite range, the B1 and B2 assemblages are interpreted to have fractionated from a high-magnesium basaltic andesitic magma, as opposed to a basaltic magma.

Identification of parental magmas for these medium K andesites utilizes their distinctive, most Mg-rich mineral compositions. The olivine (Fo_{85-87}) and augite (Mg# 81-85) core compositions of the B1 and B2 assemblage are some of the most mafic crystal assemblages observed at MBVF. The only near-primary flow unit at MBVF that carries such mafic equilibrium olivine and augite is the high-Mg basaltic andesite of Tarn Plateau. Similar whole rock trace element patterns (e.g., steep REE patterns) of the medium-K flow units and the high-Mg basaltic andesite of Tarn Plateau supports their co-genetic relationship. The high-K *acp* flow unit must be derived from a distinct parental component, as the BA3 assemblage lacks olivine and contains augite that is more calcic in composition than any augite population in the medium-K flow units, and has a distinctive REE pattern. Despite the wide age range among the four flow units of this study, mineral compositions and textures observed in all flow units suggest that at least two types of parental magmas to the andesites in this study tapped a similar range of cumulate material on their way up to the surface.

Acknowledgments

Sincere appreciation is extended to the Mount Baker Volcano Research Center, Western Washington University's Geology Department and Western Washington University's Advance for Research Program for the funding of this project, as well as travel to and from professional meetings. Bernard Housen, Chris Sutton, Kathleen Kitto and Michael Barr, without your generous support, this project and my growth in the scientific community would not have been possible.

A warm and heartfelt thank you goes out to my advisor Susan M. DeBari, whose guidance and encouragement throughout this process cultivated my scientific and critical thinking skills. Your humility, intellectuality and benevolence make you a role model in the eyes of many. I am incredibly fortunate and eternally grateful to have had you as my advisor.

To my committee members: your time and commitment to this project is greatly appreciated. To Rachel Teasdale, at Chico State University, thank you for your insightful and intriguing comments/suggestions. You made long-distance advising appear instinctive. To Jackie Caplan-Auerbach, thank you for teaching me how to convey my ideas/interpretations in a lucid fashion. You've taught me to become a more capable writer. To David Tucker, your knowledge of the Mount Baker volcanic field was an incredible asset to this project. Your expertise and skills in the field are unmatched and deserve recognition. Additionally, I'd like to thank George Mustoe, Charles Wandler, Julie Filer, Dr. Russ Burmester, Dr. Michael Clynne of the USGS, Dr. Scott Kuehner at University of Washington, and Dr. Keith Putirka at California State University, Fresno for sharing their scientific knowledge. Your dedication to conducting quality research is highly respected.

To my fellow petrologists/colleagues – Eliza Andrews, Mai Sas, Luan Heywood and Rebecca Morris - for showing me how to have a good time while doing good research. To my fellow students of color and student organizations at WWU – Ethnic Student Center, Latino Student Union, MEChA and SACNAS – for you kept me sane and moving forward at my lowest points. *Son familia ustedes.*

Special thanks goes out to Dr. Verónica Vélez, Dr. Kristen French and Dr. Regina Barber DeGraaff for being incredibly real about the graduate student of color experience. Thank you for being that extra support I so desperately needed throughout this process. The world needs more beautiful and empowering individuals like you three.

My entire academic journey would not have been possible without the support of family and close friends. Mamá y papá, thank you for teaching my sisters and I that *la educación es la mejor arma*. Paula and Mónica, you never ceased to serve as a source of love and inspiration. Cindy, you were always there to provide mental, physical and emotional support despite the distance between us. *Los amo a todos.*

Finally, I want to acknowledge all marginalized and oppressed people of the community, the nation and the world. Many of you have given up everything, left your homes and families, and even risked your lives to give the future generation a chance at a better life. We are nothing without your courage, strength and resilience. *La lucha sigue.*

Historical Note

In the present thesis, I use the name *Mount Baker* in reference to the highest peak in the North Cascades, a stratovolcano of the Garibaldi volcanic belt in northwestern Washington. I am well aware that *Mount Baker* is the Eurocentric name assigned to the conspicuous stratocone in honor of the European explorer Lieutenant Joseph Baker, who spotted the peak in 1792. Such Eurocentric practices are deeply embedded in historical and modern scholarship and often dismiss indigenous history and culture. Before the arrival of Europeans in western North America, *Mount Baker* was known as *Koma-Kulshan* by the Nooksack, Skagit and Lummi people, and more simply as *Kulshan* by the Lummi people as well, to name a few. I use the name *Mount Baker* strictly out of convention, not as a chauvinistic claim that European explorers had exclusive ownership of the nomenclature of geographical discoveries.

Table of Contents

LIST OF TABLES

List of Figures

Introduction

The petrogenesis of intermediate magmas in arcs, along with their contribution to crustal growth, remains an area of active research among petrologists (e.g., GeoPRISMS, 2010). The simplest hypothesis for differentiation is fractional crystallization, where a magma system undergoes the separation of the solid (crystals) from the melt (liquid), resulting in a more evolved (siliceous) magma composition. Intermediate magmas have also commonly been interpreted to result from mixing of mafic magmas with more felsic differentiated magmas or crustal melts. Recharge mixing (Kent et al., 2010) may occur when a basaltic magma that is too dense to erupt mixes with a dacitic magma (of unspecified origin) that is too viscous to erupt. Upon mixing, the magmas overcome these barriers, promoting efficient mixing to produce an andesitic lava eruption (Kent et al., 2010). In continental arcs, fractional crystallization may be accompanied by crustal contamination (Grove and Kinzler, 1986), which, depending on the rate of assimilation, could significantly affect the geochemical signature of a magma. Hildreth and Moorbath (1988) propose a more complex model involving a combination of the above processes to produce a MASH (Melting, Assimilation, Storage and Homogenization) zone where andesites can be generated. Building on the MASH model, Annen et al (2006) have shown that andesites can also be produced in deep crustal hot zones by mixing of residual melts after fractional crystallization of H_2O-rich basalt with deep crustal partial melts. In contrast to these differentiation processes, some andesites have been proposed to originate through primary melting of subducted basalt and subsequent interaction with the mantle wedge (Yogodzinski and Kelemen, 1998).

The application of the hypotheses described above for interpreting petrogenetic processes is typically based on detailed whole rock geochemical analyses (major elements, trace elements, and isotopes), but with less emphasis on the information provided by in-situ mineral geochemical analyses as recorders of magmatic processes (e.g. Baggerman and DeBari, 2011; Gross, 2012). Mineral studies are essential for understanding the evolution of arc systems as they preserve the complex history of magmatic processes through their various textures and compositions (e.g., Ginibre et al., 2007). Many studies use mineral compositions in conjunction with whole rock chemistry to discern the evolution of a magmatic system, however, they often lack the critical information that can be gleaned from mineral textures. Utilizing the combination of mineral textures and compositions with whole rock chemistry, though adding complexity to the study, is critical to unraveling the complicated history of magmatic systems (Streck, 2008).

Other often ignored, but rich recorders of magmatic processes are crystal clots (two or more mineral phases occurring in clusters) that are commonly found in calc-alkaline lavas worldwide (Wilkinson et al., 1964; Stewart, 1975; Garcia and Jacobson, 1979; Arculus and Wills, 1980; Gill, 1981). Crystal clots have high interpretive value because they represent co-crystallizing mineral assemblages and thus provide crucial geochemical and textural information. They commonly contain minerals that are out of equilibrium with the liquid, and can therefore give insight into earlier stages of magmatic conditions that would otherwise be undetectable or overseen through individual phenocrysts (Conrad et al., 1983). Furthermore, crystal clots can provide evidence of wall rock assimilation, magma mixing, pre-eruption crystallization conditions and possible

magmatic sources (Gill, 1981). Jerram et al. (2003) have also stressed the importance of studying crystal clots, referring to them as the "building blocks" of igneous rock textures.

This study proposes an origin for crystal clots and utilizes a rich dataset of crystal clot analyses, in combination with individual phenocryst data, to elucidate processes occurring in the arc plumbing system beneath the Mount Baker volcanic field (MBVF). I use them to provide further insight into pre-eruption crystallization conditions, magma mixing scenarios, crustal assimilation and possible magmatic sources. The MBVF serves as the ideal natural lab setting for such a study due to its predominance of andesite and its abundance of crystal clots. Previous work shows that open-system processes play a critical role in the generation of andesites at MBVF (Baggerman and DeBari, 2011; Gross, 2012). However, these authors focus largely on whole rock data to provide magma-mixing scenarios and lack interpretations of sources/origins for the various populations of individual phenocrysts and crystal clots analyzed.

The primary objectives of this study are to 1) identify and characterize phenocryst populations and crystal clots within individual flow units, 2) infer the origin of phenocrysts and/or crystal clots and the relationships between them, and 3) interpret the sub-crustal processes that these crystal populations suggest for andesite petrogenesis. In this study hornblende-bearing andesites are described and discussed separately from hornblende-free andesites, as their whole rock chemistry is strikingly different.

The combination of mineral compositions and textures, in conjunction with whole rock chemistry, is used to establish a phenocryst and crystal clot population framework that produces a data-rich picture of the petrogenetic processes occurring at MBVF. As a result, this study goes to show that whole rock data of mixed magmas alone limits the

extent of interpretations for intermediate magma generation. Given the diversity of andesites in age and character in this study, I also consider whether or not the same processes are producing all intermediate magmas of MBVF.

Geologic Background and Tectonic Setting

The Cascade volcanic arc is composed of more than 2,300 Quaternary volcanoes extending 1,250 km from Lassen Peak in northern California to Mt. Meager in southern British Columbia (Hildreth, 2007). Volcanism in the Cascade arc results from subduction of the Juan de Fuca plate. The hot, young Juan de Fuca plate subducts obliquely westward beneath the North American plate at a rate of approximately 3-4 cm/yr (Heaton and Kanamori, 1984; McCrory et al, 2004; Figure 1). Guffanti and Weaver (1988) defined five Cascade arc segments on the basis of vent distribution, subduction geometry, and volcanic front orientation: 1) the Garibaldi Volcanic Belt (GVB), 2) Mount Rainier to Mount Hood, 3) the Oregon Cascades, 4) the Mount Shasta region, and 5) the Lassen region. More recently, Schmidt et al. (2008) used the addition of primitive magma type distribution and their Sr and Nd isotopic data to redefine these into four segments, but the Garibaldi segment, which includes the MBVF, remains the same. The GVB of the Cascade volcanic arc exhibits a shift in arc trend from N-S to NW-SE with decreased mafic output (Borg and Clynne, 1998).

Mount Baker, the second southernmost volcano of the Garibaldi Volcanic Belt, is the only andesitic stratovolcano of the northern Cascade arc (Glacier Peak, Mount Garibaldi, Mount Cayley and Mount Meager being more silicic). It is a young cone (~40 ka) that is part of the Mount Baker volcanic field (MBVF), a multi-vent Quaternary

volcanic system that has been continuously active for the last 1.3 Ma (Hildreth et al., 2003) and includes Kulshan caldera and the Black Buttes stratocone. Mount Baker lies on the margin of the 1.15 Ma Kulshan caldera, which is the oldest *eruptive* episode at MBVF, with pre-caldera activity at 1.15-1.3 Ma (Hildreth et al., 2003). McCrory et al. (2004) propose a subducting slab depth of ~90-100 km beneath MBVF and Green and Harry (1999) propose a slab age of 19-20 Ma beneath MBVF.

The volcanic field is underlain by Paleozoic to Mesozoic tectono-stratigraphic terranes accreted during the Cretaceous and redistributed by extensional and strike-slip faulting throughout the Paleogene (Misch, 1966; Brown, 1987; Tabor et al., 2003). The stratocone itself emerges through a structural feature referred to as the "Mount Baker window" (Tabor et al., 2003), which resulted in exposures of the accreted terranes. The principle rocks through which the volcanic field emerges are the marine clastic and volcaniclastic rocks of the Nooksack Formation and Wells Creek volcanics (Tabor et al., 2003) and the Devonian to Permian Chilliwack Group (Brown et al., 1981; Danner, 1966). The Nooksack Formation and Wells Creek volcanics are significant in that they are interpreted to be constituents of the Harrison terrane and Gambier Group of British Columbia, which are overlap assemblages on the Wrangellia terrane (Monger and Journeay, 1994).

The Wrangellia terrane is thought to underlie MBVF. Evidence for this comes from (1) the correlation of the overlying Nooksack Formation and Wells Creek volcanics with the Gambier Group and Harrison terrane of southern British Columbia, which are underlain by Wrangellia; (2) seismic and gravity studies, and (3) isotopic studies. Geologic observations of Journeay and Friedman (1993), Brown et al. (2000), Monger

and Price (2006) and Monger and Nokleberg (1996) report that products of the Gambier group and Harrison terrane extend from northwestern Washington, north along the coast of British Columbia, and into Alaska. Since the Gambier and Harrison rock units were constructed atop Wrangellia, it is likely Wrangellia lies underneath wherever these are exposed (Mullen, 2011). Seismic studies also indicate Wrangellia underlies MBVF based on reflection and refraction profiles (Ramachandran et al., 2004. 2005; Dash et al., 2007), seismic velocity profiles (Christensen and Mooney, 1995) and gravity anomaly modeling (Ramachandran et al., 2004). More recently, Mullen (2011) reported that the isotopic signatures of silicic magmas at MBVF and Wrangellia samples are consistent with generation by partial melting of Wrangellia. Mullen (2011) goes on further to suggest that stacking ~10 km of terranes (e.g., Gambier and Harrison) atop the 25-30 km thick Wrangellia (Greene et al., 2006) coincides with the proposed crustal thickness of 40-45 km above MBVF proposed by Bostock and VanDecar (1994) and Ramachandran et al. (2006).

Hildreth et al. (2003) published the foundational study of the eruptive chronology of MBVF (K-Ar and $^{40}Ar/^{39}Ar$) along with major element data for most flow units. Their geologic map of the main eruptive components with descriptions and ages of individual units (Figure 2) provides the framework for this thesis. Major element data for approximately 500 well-dated samples are provided but with limited interpretations, providing an ideal starting point for more in-depth geochemical studies such as Moore and DeBari (2012), Baggerman and DeBari (2011), Shaw (2011), Gross (2012) and Sas (2015). Though these studies have provided much insight into the magmatic processes of

MBVF, none have focused on the origin and possible source(s) of its voluminous intermediate magmas (54-60 wt. % SiO_2).

Andesites comprise 45-55% of the cumulative erupted volume at MBVF and have been identified and mapped as over thirty distinct units (Hildreth et al., 2003). However, with the end of the Kulshan episode (0.99 Ma), MBVF has seen the genesis of predominantly intermediate lavas, with approximately 92% andesites. Though termed "andesite", the true geochemical composition of the units identified ranges from basaltic-andesite to dacite. This study focuses on four "true" intermediate (54-60 wt. % SiO_2) flow units erupted from the Mid- to Late-Pleistocene, with their geochemical compositions ranging from basaltic-andesite to trachydacite (Le Maitre et al, 1989). The names and abbreviations of the four flow units are those assigned by Hildreth et al. (2003) and were selected using major element whole rock data of Hildreth et al. (2003). An overview of each is presented below.

The andesite of Swift Creek (*asw*) is an intracanyon lava flow with remnants in the Swift Creek canyon and eastward adjacent creeks (e.g., Fourth of July Creek) (Figure 3a). Several of the exposures form cliffs along Swift Creek, making them difficult to access without stream travel (Figure 3b). The flow unit typically exhibits sets of 7 to 9 m tall divergent, curving columns (typical of sub-glacial eruptions) (Figure 3c), along with blocky and pillow-like flows that generally underlie the columnar sets. Two of the samples collected lie outside of the mapped region of Hildreth et al. (2003), though the chemistry and texture of the samples are identical to those in the mapped region. Although the source vent is not known, the flow was most likely fed by a dike near the

SE margin of Kulshan Caldera. Hildreth et al. (2003) reported a K-Ar age of 48 ± 18 ka for *asw*.

The andesite of Dobbs Cleaver (*adb*) and andesite of Dobbs Creek (*ado*) are also both intracanyon flow units. Together, they form a steep, platy outcrop along the eastern edge of Cougar Divide, roughly 4.25 km long and 0.75 km wide at its widest outcrop (Figure 4a). Both flows are densely vegetated (Figure 4c) and not visible from any trail or road, therefore, intense bushwhacking is required. In addition, *ado* crops out beneath *adb* and cannot be accessed by descending. Instead, access to *ado* requires uphill travel along loose rubble and forested slopes of the cleaver (Figure 4b). Hildreth et al. (2003) reported a K-Ar age of 119 ± 23 ka for *ado* and 105 ± 8 ka for *adb*.

The andesite of Coleman Pinnacle (*acp*), accessible from the Ptarmigan Ridge trail is 3.75 km long and 0.75 km wide at its widest outcrop (Figure 5a). The flow forms a cap on Ptarmigan Ridge with minimally vegetated exposures right along the trail, resulting in easy access but intensely weathered surfaces. Intermingled with the mapped exposures of *acp* are outcrops of the andesite of Table Mountain (Hildreth et al., 2003) but these are easily distinguishable by their plagioclase-rich porphyritic texture compared to the hornblende-rich Coleman Pinnacle flow unit. Exposures of *acp* vary from blocky outcrops to glassy, vertically oriented polygonal columns, indicative of subglacial eruptions (Figure 5b). Columns range in size from 5 to 20 cm wide and reach up to 15 m high. The pinnacle itself is composed of massive, blocky outcrops of andesite that are, ironically, more vegetated and weathered than outcrops at lower elevations. The *acp* flow unit is the only unit in this study that exhibits inclusions (mafic appearing) observable in the field (Figure 5c). This flow yields a K-Ar age of 305 ± 6 ka (Hildreth et al., 2003).

Analytical Methods

Sample collection and preparation

Twenty-five samples were collected (5-7 per flow unit) to increase representation of each flow unit as mapped by Hildreth et al. (2003). Hand-size samples were collected, weathered surfaces were discarded, and the remainder was broken down into chips with a rock hammer in the lab. Chips that exhibited weathering and/or hammer markings were discarded to avoid contamination. Rock chips were then further crushed in a chipmunk equipped with tungsten-carbide plates.

XRF and ICP-MS analyses

Of the twenty-five samples collected, twenty-three were analyzed for 10 major element oxides and 19 trace elements (Ni, Cr, Sc, V, Ba, Rb, Sr, Zr, Y, Nb, Ga, Cu, Zn, Pb, La, Ce, Th, Nd, U) using a Thermo-ARL automated X-ray fluorescence spectrometer at the Geoanalytical Lab of Washington State University (WSU). Samples for XRF analysis were prepared at Western Washington University (WWU) following the single bead low-dilution fusion technique (Johnson et al., 1999). Rock chips are ground in a tungsten-carbide grinding vessel in a shatterbox for approximately 5 minutes. Glass beads were then prepared by mixing dry rock powder and dry dilithium tetraborate flux with a 1:2 ratio (3.5 g and 7 g) and fusing them in a muffle oven in carbon crucibles at 1000° C for 10 minutes. Glass beads were then cooled and reground in the tungsten-carbide shatterbox and re-fused to ensure complete homogeneity. At WSU, glass beads were ground on a 600 silicon carbide grit and a 600 grit glass plate with alcohol to remove

metal contamination. Lastly, the beads are washed in an ultrasonic bath, rinsed with alcohol and dried before being loaded into the XRF spectrometer.

Rare earth elements (REEs) and other trace elements (Ba, Th, Nb, Y, Hf, Ta, U, Pb, Rb, Cs, Sr, Sc, Zn) were analyzed from the same twenty-three samples as above, using an Agilent 7700 inductively coupled plasma mass spectrometer (ICP-MS) at WSU. Samples for ICP-MS analyses were prepared in the same manner as for XRF but with a 1:1 ratio of dry rock to dry dilithium-tetraborate flux ratio (2 g each) and no regrinding or re-fusing of the glass bead due to potential Nb contamination from WWU's tungsten-carbide grinding vessel. Single fused ICP-MS glass beads were reground and re-fused at WSU using an alumina-ceramic grinding vessel. Duplicate analyses show that Nb concentrations from XRF and ICP-MS analyses differ by 17%, with elevated XRF measurements. Rb concentrations from XRF analyses are also elevated, differing by 8% from ICP-MS analyses. Values reported for Sc, Ba, Sr, Zr and Y are from ICP-MS analyses, but are similar to XRF within error (<5%).

Electron Microprobe

Samples for electron microprobe analyses were selected using the major element data and abundance of crystal clots seen in thin section. Two samples from each flow were selected for microprobe analysis in order to represent the most Si-rich and Si-poor members of each flow. Due to limited funding only one thin section from *acp* was analyzed.

Analyses were executed at the University of Washington (UW) using a JEOL 733 Superprobe electron microprobe (EMP) equipped with four wavelength dispersive

spectrometers (WDS). Elements were calibrated using a standard set of natural and synthetic minerals and glasses. Minerals analyzed include olivine, augite, orthopyroxene, Fe-Ti oxides and plagioclase, with the addition of hornblende in the *acp* sample. The accelerating voltage was set at 15kV for all analyses. Beam specifications were set at a current of 15nA and a diameter of <1 μm for olivine, pyroxenes and Fe-Ti oxides. For plagioclase and hornblende, a beam current of 10nA and beam diameter of 0.20 μm was used. Peak counting times for elements ranged from 20 to 40 seconds, depending on which minerals were being analyzed.

Results

Petrography and Mineral Chemistry

The following sections describe the textures, zoning and chemistry of phenocrysts, microphenocrysts and crystal clots observed in each flow unit. Mineral modes, along with textures, zoning patterns and compositions, are summarized in Table 1. Complete mineral data is presented in Tables 3-8. In addition, plagioclase and pyroxene compositions are presented in Figure 6. The first three units described are hornblende-free, the last, Coleman Pinnacle, is hornblende bearing. Unique characteristics of each flow unit are summarized and displayed in Figure 7 and described more fully in the text below.

Due to the great amount of variation in textures and chemistry observed in a single mineral phase in a given flow unit, I have described populations of minerals for each flow unit. In the paragraphs below for each flow unit, populations of a given mineral are assigned numbers in order of their geochemical "primitiveness" (i.e., Mg# 81-85 of augite is considered the most primitive, as is An_{59-69}), with population 1 in each flow unit

as the most primitive. In addition, figures for each mineral phase in each flow unit show petrographic and/or backscattered electron (BSE) images, core-to-rim diagrams and when necessary, variation plots to display chemical differences among populations of a given mineral phase. In addition, crystal clots are described separately to distinguish between populations of crystal clots, though their phases are included in the descriptions of populations of minerals.

Andesite of Swift Creek (asw)

The andesite of Swift Creek is porphyritic with 15-20% phenocrysts of plagioclase, augite, orthopyroxene, olivine and Fe-Ti oxides in a pilotaxitic, hypocrystalline groundmass composed of plagioclase microlites, oxides and rare glass. Some of the samples exhibit strong flow lineation, especially with elongate phenocrysts. A distinct characteristic of *asw* is the occasional oxidation reaction textures along crystal edges of all mineral phases, including olivine, which is commonly completely reacted (Figure 7a).

Plagioclase is the most abundant mineral phase (75-80% of phenocryst population) of *asw* and forms subhedral to euhedral microphenocrysts and phenocrysts that range in size from 0.25 to 3.75 mm. Composition of plagioclase ranges from An_{41-69}, with a core range of An_{46-69} (Table 2). Four populations of plagioclase are identified on the basis of chemistry and texture (Figure 8, Table 2). The first and most calcic population of plagioclase, forms subhedral phenocrysts (1.2-1.5 mm) that exhibit a fine-sieved outer zone, followed by rounded overgrowth rims (Figure 8a). Two grains in different thin sections from this population were analyzed, both with a core composition of An_{69} (Figure 8e). Also, this population typically displays patchy zoning in BSE. The second

population of plagioclase (the most abundant) forms subhedral individual and crystal clot phenocrysts (0.5-1.25 mm). Core compositions of this population range from An_{57-66} with middle and rim sections displaying oscillatory zoning patterns (Figure 8e). This population commonly contains inclusions of oxides and apatite in a reacted core (Figure 8b). Population 3 of plagioclase forms euhedral microphenocrysts (0.25-0.5 mm) that have a core composition of An_{52} (Figure 8e). A unique characteristic of this population is the blebby coarse-sieved mid-zone, which contains inclusions of apatite (Figure 8c). Population 4 of plagioclase shares characteristics of population 1 and 3, but is much more sodic in composition (Figure 8e). Only one grain (1.25 mm) of population 4 was analyzed with a core composition of An_{46}. This population is euhedral and exhibits blebby coarse-sieves scattered throughout, similar to population 3 (Figure 8d). Fine-sieved outer zones with overgrowth rims are also characteristic of this population, similar to population 1 but not rounded. In summary, all plagioclase populations show some level of disequilibrium. The two most sodic populations (An_{46-52}) have blebby coarse-sieves throughout. The two most calcic populations (An_{57-69}) display less disequilibrium with fine sieves and slightly reacted cores.

Augite (8-12% of the total phenocryst population) occurs as anhedral to euhedral microphenocrysts and phenocrysts that range in size from 0.3 to 2.25 mm. The compositional range of augite in *asw* is Mg# 72-85, with cores spanning the same range (Table 4). Five populations of augite are identified on the basis of texture, zoning and chemistry (Figure 9). The first population of augite has elevated Al_2O_3 concentrations (4.2-4.9 wt. %) and forms weak normal-zoned microphenocrysts (0.3-0.5 mm) that are anhedral (intercumulus in clots) and euhedral (phenocryst) (Figure 9a, g). Core

compositions range from Mg# 81 to 85 with one normal-zoned rim analysis of Mg# 84 (Figure 9f). This population contains minimal oxide inclusions and displays "undulatory-type" extinction, characteristic of augites with elevated Al_2O_3 concentrations (per this study). Population 2 is characterized as anhedral and subhedral microphenocrysts and phenocrysts (0.3-1.5 mm) found in crystal clots and as individual phenocrysts. Anhedral augite is generally intercumulus in the clots, whereas subhedral augites are located along edges of the clots. Population 2 is normally zoned with compositions ranging from core Mg# 79 to 83 and with an analyzed rim of Mg# 75 (Figure 9f). This population sometimes contains slight-sieved cores with inclusions of plagioclase and rarely oxides and pyroxenes. Patchy zoning in BSE is also characteristic of augite population 2, especially in individual phenocrysts (Figure 9b). Population 3 of augite forms anhedral to euhedral microphenocrysts and phenocrysts (0.3- 0.75 mm). This population differs from population 2 in that the grains are oscillatory, reverse-zoned rather than normal zoned and is absent in crystal clots. They have similar core compositions of Mg# 78-83 but rim compositions of Mg# 80-84 (Figure 9c, f). Most augites of population 3 are unsieved, but few exhibit fine-sieves. Populations 4 and 5 are the least abundant and only one grain from each population was analyzed. The fourth population of augite (0.4 mm) forms an anhedral microphenocryst that is embayed. This normal-zoned grain has a core composition of Mg# 75 and rim Mg# 72 (Figure 9f). The slight-sieved core contains minimal oxide inclusions and the embayment contains an intergrowth of plagioclase (Figure 9d). Augite population 5 (0.6 mm) is a reverse-zoned, subhedral phenocryst with an embayment (Figure 9e). Composition of the analyzed augite is core Mg# 72 and rim Mg# 81 (Figure 9f). The core of this population contains minimal oxide inclusions. In

summary, the two most Mg-poor augite populations (Mg# 72-75) contain embayments and sieves. The most Mg-rich augite population (Mg# 81-85) has high levels of Al_2O_3 (>4 wt. %) and lacks disequilibrium textures. The other two populations of augite (Mg# 78-83) display a variety of disequilibrium textures, however, less exaggerated than the Mg-poor populations.

Orthopyroxene (3-8% of total phenocryst population) forms anhedral to subhedral microphenocrysts and phenocrysts (0.25-1.5 mm) that range in composition from Mg# 65 to 79 (Table 5). Five populations of orthopyroxene are identified based on texture, zoning and geochemistry (Figure 10). Population 1 of orthopyroxene forms microphenocrysts (0.3-0.4 mm) that are subhedral as individual crystals and anhedral in crystal clots. This population exhibits oscillatory normal zoning with core Mg# 77-79 and rim Mg# 74 (Figure 10e). The absence of inclusions is characteristic of this population, along with occasional sieved cores (Figure 10a). The second orthopyroxene population is most likely a subpopulation of population 1, but observed only in crystal clots and with nearly double the amount of Al_2O_3 concentration (1.7-2.1 wt.%) (Figure 10b, f). Population 2 forms intercumulus anhedral to subhedral microphenocrysts and phenocrysts (0.25-0.8 mm). Core analyses are Mg# 75-79 (Figure 10e). Absence of inclusions and disequilibrium textures is also characteristic of population 2. Populations 3 and 4 are rare and only one crystal from each population was analyzed. The population 3 orthopyroxene is a subhedral microphenocryst (0.4 mm). This population is reverse-zoned with core Mg# 72 and rim Mg# 75 with minimal core exsolution (Figure 10a, e). The orthopyroxene of population 4 is normal zoned with core Mg# 68 and rim Mg# 67 (Figure 10e). This phenocryst (0.9 mm) is subhedral and displays exsolution in its core as

well (Figure 10c). The fifth population of orthopyroxene forms subhedral phenocrysts (0.6-1.1 mm) that may contain oxide inclusions and minimal exsolution in core. Patchy zoning is noticeable in BSE for this population, although it is not observed in all phenocrysts. This population is strongly reverse-zoned with core Mg# 65-68 and rim Mg# 73-79 (Figure 10d, e). In summary, the two most Mg- poor populations of orthopyroxene (Mg# 65-68) contain exsolution in cores but display different zoning patterns. The intermediate orthopyroxene, population 3, also displays minor exsolution but is significantly more Mg-rich (Mg# 72) than the Mg-poor orthopyroxenes. The two most Mg-rich populations of orthopyroxene share a similar range of core compositions (Mg# 75-79 and 78-79). However, one population contains sieved cores and the other lacks disequilibrium textures and has elevated Al_2O_3 concentrations (> 1.5 wt. %).

Olivine (5-8% of the total phenocryst population) forms subhedral to euhedral phenocrysts that range in size from 0.5 to 2.5 mm. There is only one population, with core compositions Fo_{85-87}, normally zoned, with rims as fayalitic as Fo_{69} (Table 6, Figure 11c, d). Resorbed cores and inclusions of chromite are characteristic of *asw* olivine, and larger crystals commonly contain large embayments (Figure 11a, b). Olivine is abundant both as individual phenocrysts and in crystal clots.

Fe-Ti oxides form equant, non-exsolved subhedral microphenocrysts that make up ≤1 % of the total phenocryst population. Fe-Ti oxides are rare in the groundmass and occur mostly as inclusions or microphenocrysts in crystal clots. Ulvospinel crystals have compositions of 69.6-72.2 wt. % FeO^T and 17.3-22.9 wt. % TiO_2. Ferrian ilmenite has compositions of 45.8-48.0 wt. % FeO^T and 47.5-49.5 wt. % TiO_2. Compositions are presented in Table 7.

Crystal clots

Crystal clots are abundant in samples of *asw* and comprise 3-7% of the sample. Two types of crystal clots are identified in *asw* in terms of texture and chemistry (Figure 12).

Crystal clot type A (Figure 12a) (1.5-5.0 mm wide) consists of augite, plagioclase, ±olivine and ±orthopyroxene and is represented by five analyzed clots (Table 8). Augite (Mg# 79-83), the dominant phase, occurs as anhedral and subhedral crystals that commonly have sieved cores and secondary reaction zones. Augites may contain inclusions of plagioclase and may be incorporated into larger, euhedral plagioclase. Augite of clot type A is phenocryst augite population 2 described above. Plagioclase (An_{57-66}) forms two texturally distinct populations in crystal clots. One population is characterized as having a coarse-sieved core with secondary reaction spots. This population is generally subhedral and wide. The second plagioclase population is unsieved and forms slender, tabular sub-euhedral crystals. Both plagioclases span the same An content and are plagioclase population 2 described above. Orthopyroxene (Mg# 75-79) forms anhedral to subhedral crystals with occasional sieved cores and inclusions of plagioclase. Secondary reaction zones are common, as well as oxide inclusions. The orthopyroxene of this clot is orthopyroxene population 2 described above. Olivine (Fo_{85}) forms anhedral to subhedral crystals that commonly display secondary reaction textures, and are sometimes completely reacted. They contain inclusions of chromite and may also contain embayments. One analyzed clot (Figure 12b) is likely a subpopulation of clot type A due to its similar compositions of orthopyroxene and plagioclase, though olivine and augite are absent. In addition, orthopyroxene is population 1 and plagioclase is

population 1 described above, which are subpopulations of the phenocrysts making up clot type A.

Crystal clot type B in *asw* is represented by one analyzed clot (Table 8, Figure 12c). This clot (0.9 mm) consists of augite and plagioclase. Augite (Mg# 81-82) forms anhedral crystals with scattered sieves and oxide inclusions. Though similar to augites in clot type A, augites of clot type B have elevated Al_2O_3 concentrations (4.2-4.9 wt. %) and exhibit undulatory-type extinction. Augite of this clot is augite population 1 described above. Plagioclase (An_{65}) forms sub-euhedral, unsieved crystals with minimal oxide inclusions. Plagioclase of clot type B is plagioclase population 2 described above.

In summary, crystal clots represent the most mafic endmember of phenocrysts. The differences in size, textures and concentrations of Al_2O_3, make clot type A and clot type B likely unrelated, even though core compositions of augite and plagioclase are similar.

Andesite of Dobbs Creek (ado)

The andesite of Dobbs Creek (*ado*) is porphyritic with 20-28% phenocrysts of plagioclase, augite, orthopyroxene, olivine and Fe-Ti oxides in a holocrystalline, pilotaxitic groundmass. The groundmass is composed of plagioclase microlites and microphenocrysts of pyroxenes, oxides and possible olivine. All *ado* samples display strong phenocryst flow lineation (Figure 7b).

Plagioclase is the dominant mineral phase in *ado* and constitutes 65-80% of the total phenocryst population. Plagioclase microphenocrysts and phenocrysts range in size from 0.4 to 4.25 mm and compositions range from An_{43-70} (Table 3). Four distinct populations

are identified on the basis of texture and mineral chemistry (Figure 13). The first population (40%) consists of subhedral crystals (0.4-2.0 mm) with finely sieved rims and overgrowth rims that are found in crystal clots as well. This population contains channelized groundmass material in the sieved region (Figure 13a). Core compositions are An_{59-64} (Figure 13e). The second population (40% of the plagioclase phenocryst population) is characterized as blebby coarse-sieved, rounded subhedral to euhedral phenocrysts (0.5- 4.25 mm). This population commonly displays patchy zoning in BSE and contains inclusions of apatite, oxides, occasional pyroxene and groundmass inclusions (Figure 13b). Core compositions have a range of An_{54-59} (Figure 13e). The third population of plagioclase (15%) is characterized as subhedral phenocrysts (1.0-1.2 mm) with rounded edges (Figure 13c) and occasional inclusions of groundmass material along the rim. Weak, patchy zoning is noticeable in BSE. Although similar in texture to population 1, this population is more albitic with a narrow core compositional range of An_{47-48} (Figure 13e). Population 4 (5% of plagioclase population) (2.25 mm) is the most albitic in composition and the most euhedral. This population of plagioclase has a core composition of An_{45} (Figure 13e). In addition, inclusions of pyroxene clots are common in the population (Figure 13d). In summary, the most sodic plagioclase (An_{45}) lacks disequilibrium textures. Populations 1 (An_{59-64}) and 3 (An_{47-48}) share similar (minimal) disequilibrium textures (e.g., overgrowth rims on fine sieves with channelized groundmass) but have strikingly different compositions. In between this wide range, population 2 (An_{54-59}) displays the most extensive disequilibrium features.

Augite (7-10 % of the total phenocryst population) occurs as subhedral to euhedral crystals and commonly displays disequilibrium textures (e.g., sieves and embayments).

Augite ranges in size from 0.5 to 2.75 mm, although they can reach up to 4.5 mm in size in crystal clots. Compositions of augite range from Mg# 70 to 87 (Table 4). Four distinct populations of augite are identified in terms of texture, zoning and chemistry (Figure 14). The first population of augite is rare and has the highest concentration of Al_2O_3 (4.1 wt. %) (Figure 14f). This population forms equant, anhedral to subhedral microphenocrysts (0.4 mm) that lack disequilibrium textures (Figure 14d). This population has both a core composition of Mg# 84 and rim composition of Mg# 83 (Figure 14e). Augite population 2 is rare and only one phenocryst was analyzed. This population has coarsely sieved cores along with oxide inclusions and exhibits "patchy" zoning in BSE and "undulatory-type" extinction (Figure 14b). The analyzed phenocryst (0.9 mm) is subhedral and reverse-zoned with core Mg# 82 and rim Mg# 87 (Figure 14e). The third population of augite forms subhedral phenocrysts (1.0 mm) that contain inclusions of oxides and occasional pyroxene in the core (Figure 14c). This population lacks zonation with both core and rim compositions of Mg# 75 (Figure 14e) and has a resorbed core. The fourth population of augite forms subhedral, oscillatory reverse-zoned phenocrysts (0.5-1.0 mm). This population contains oxide inclusions and often exhibits minor embayments and fine sieves (Figure 14d). Compositions range from core Mg# 70 to 73 and rim Mg# 73 to 80 (Figure 14e). In summary, the most Mg-rich augite (Mg# 83) has high concentrations of Al_2O_3 (Figure 14f) and lacks disequilibrium textures. The next two intermediate populations of augite (Mg# 75-82) show the most extensive disequilibrium textures (e.g., resorbed core and coarse sieves) (Figure 14b-c). The most Mg-poor augite (Mg# 70-73) is fine-sieved and has minor embayments (Figure 14d).

Orthopyroxene makes up 5-7% of the total phenocryst population and ranges in size from 0.3 to 2.0 mm. Orthopyroxene phenocrysts are generally more slender and tabular and contain fewer inclusions than augite, and are more abundant in crystal clots than as individual phenocrysts. Compositions of orthopyroxene range from Mg# 68 to 74 (Table 5). On the basis of texture, zoning and chemistry, two populations of orthopyroxene are identified (Figure 15). Population 1 of orthopyroxene forms subhedral, weak normal-zoned microphenocrysts and phenocrysts (0.4-1.5 mm). Compositions range from 72 to 74 core Mg# and 71 to 74 rim Mg# (Figure 15d). No disequilibrium textures or inclusions are observed in this population (Figure 15a). The second population of orthopyroxene is characterized as weak reverse-zoned subhedral microphenocrysts and phenocrysts (0.3-1.3 mm). Inclusions of oxides (Figure 15b) and faint reaction rims are commonly observed in the larger crystals of this population. Compositions range from 69 to 70 core Mg# and 69 to 70 rim Mg# (Figure 15d). In summary, the most Mg-rich orthopyroxene (Mg# 72-74) lacks disequilibrium textures. The felsic population has a narrow core composition range (Mg# 68-70) and displays minimal disequilibrium textures.

Olivine in *ado* occurs as equant anhedral to subhedral microphenocrysts and phenocrysts that range in size from 0.25 to 1.25 mm and Fo 66 to 73 in composition (Table 6). Olivine in *ado* is easily distinguished in thin section due to the weathering fractures that display a rusty color in plane polarized light (Fig. 7b). Olivine constitutes 3-7% of the total phenocryst population and is identified as two distinct populations (Figure 16). The first population of olivine (Fo_{72-73}) forms anhedral to subhedral phenocrysts (1.0-1.25 mm) that are embayed and occasionally display resorbed cores (Figure 16a, c). The second population of olivine (Fo_{67-68}) forms anhedral to subhedral microphenocrysts

and phenocrysts (0.25-0.75 mm) (Figure 16b, c). This population is generally mantled by indiscernible groundmass pyroxene, as evident in Figure 16b. In summary, the most forsteritic olivine (Fo_{72-73}) shows extensive disequilibrium, while the more fayalitic olivine (Fo_{67-68}) lacks disequilibrium textures. Both populations of olivine display heavily oxidized rims in both BSE and plane polarized light, along with an abundance of chromite inclusions.

Fe-Ti oxides make up 3-8% of the total phenocryst population and occur as equant anhedral to subhedral phenocrysts and microphenocrysts. Their size ranges from 0.2 to 1.0 mm and are abundant in the groundmass. The larger phenocrysts are commonly observed as individual crystals with rare inclusions of groundmass of pyroxenes and paired next to pyroxenes. Smaller phenocrysts are generally scattered and abundant in the groundmass. Ulvospinel crystals have compositions of 67.3-80.3 wt. % FeO^T and 7.1-18.1 wt. % TiO_2. Ferrian ilmenite has compositions of 39.6-49.1 wt. % FeO^T and 47.4-52.6 wt. % TiO_2. Compositions of Fe-Ti oxides are presented in Table 7.

Crystal clots

Crystal clots (1.25-2.5 mm wide) are less abundant in *ado* and comprise 1-2% of the sample. Four distinct types are identified based on crystal textures and chemistry, however; only two were analyzed (Figure 17).

Crystal clot type A (Figure 17b; Table 8) contains orthopyroxene ± augite ± plagioclase and oxides. Orthopyroxene (Mg# 69-70) forms subhedral phenocrysts and microphenocrysts with rare inclusions of oxides. Augite (Mg# 71), larger than orthopyroxene, forms equant, subhedral phenocrysts with oxides along crystal edges. Plagioclase (An_{45}) occurs as a host to orthopyroxene. The plagioclase host is a large

(2mm) euhedral phenocryst with scattered oxide inclusions. The mineral phases present in clot type A are orthopyroxene population 2, augite population 4, and plagioclase population 4, which are all described above.

Crystal clot type B (Figure 17a; Table 8) (2.5 mm) consists of orthopyroxene, plagioclase and oxides (Table 9). Orthopyroxene (Mg# 72-73) forms subhedral, elongate and equant phenocrysts with no inclusions and are population 1 orthopyroxene described above. Plagioclase (An_{59}) forms subhedral phenocrysts that are sieved along crystal edges and represent plagioclase population 1 described above. Oxides, although rare, are observed as inclusions in plagioclase.

A third type of crystal clot exists and consists of large anhedral olivine with oxide inclusions and interstitial plagioclase that is 1.25 mm wide. Minerals in this population were not chemically analyzed. A fourth, unanalyzed, clot type exists but is most likely xenocrystic due to its texture. The clot consists of microphenocrystic, granular olivine with oxide inclusions that range in size from 0.5 to 1.25mm wide.

In summary, the analyzed crystal clots of *ado* are much less abundant than in *asw*. However, felsic crystal clots are present in *ado*, whereas they are absent in *asw* (Table 8). Crystal clot type A contains the most felsic endmember of phenocrysts, whereas crystal clot type B contains the most mafic end member of phenocrysts and is similar in composition to the mafic crystal clots of *asw*.

Andesite of Dobbs Cleaver (adb)

The andesite of Dobbs Cleaver (*adb*) is porphyritic, with 20-30% phenocrysts of plagioclase, augite, orthopyroxene, olivine and Fe-Ti oxides in a hypocrystalline

groundmass. Microlitic plagioclase constitutes the majority of the microphenocrysts in the groundmass, which lacks disequilibrium textures. There is some evidence of microscopic magma mingling in this unit as exemplified by sample *adb*-07, which exhibits two distinct shades of groundmass (darker being more glassy) (Figure 7c). The samples are not vesicular, with the exception of samples collected near the margin of the flow (i.e., *adb*-01), which has 10-15% vesicles (Figure 7d). It is important to note that orthopyroxene is more abundant in crystal clots, whereas augite is more commonly observed as individual phenocrysts, similar to the *ado* flow unit.

Plagioclase is the most abundant phenocryst (68-75% of phenocryst population) observed in *adb*. Plagioclase phenocrysts range from 0.5 to 3.0 mm in size and An_{42-63} in composition (Table 3). Four populations of plagioclase are identified based on the combination of texture and chemistry (Figure 18). The first population is only found in a crystal clot and is the most calcic in composition, with cores of An_{60-61} (Figure 18e). This population is anhedral, entirely sieved and spans a wide size range (0.5-1.25mm) (Figure 18a). The second population of plagioclase is euhedral and free of inclusions and disequilibrium textures (Figure 18b). This population is slightly less calcic in composition (An_{56-57}) and much smaller in size (0.5-0.6 mm) (Figure 18e). The third and largest (0.8-3.0 mm) population (An_{46-54}) consists of oscillatory-zoned, subhedral to euhedral crystals with rounded edges that are occasionally finely sieved (Figure 18c, e). These crystals make up roughly 40% of the total plagioclase population and commonly contain inclusions of apatite and occasional Fe-Ti oxides and pyroxenes. The fourth population (0.5-1.2 mm) is also subhedral to euhedral but free of inclusions with occasional scattered sieves throughout (Figure 18d). This population is the most sodic in

composition with core compositions of An_{42-43} (Figure 18e). In summary, the most calcic plagioclase (An_{60-61}) occurs in clots and shows the most extensive disequilibrium features. The next most calcic composition (An_{56-57}) occurs only as microphenocrysts and lacks disequilibrium textures. The other two populations are more sodic, and show some level of disequilibrium.

Augite (6-10% of total phenocryst population) ranges from 0.4 to 2.0 mm in size and has a compositional range of Mg# 71-86 (Table 4). Four distinct populations of augite are identified based on texture, zoning and chemistry (Figure 19). The first and third populations of augite are scarce and only one phenocryst from each population was analyzed. Augite population 1 (0.5 mm) has the most primitive core, Mg# 81, and the highest Al_2O_3 concentration (3.9 wt. %) (Figure 19e). This population is normal-zoned (rim Mg# 78) and subhedral with coarse sieves and several oxide inclusions (Figure 19a, d). In addition, only this population displays an "undulatory-type" extinction, which appears as patchy zonation in BSE. The second population of augite also spans a wide range in size (0.5-2 mm) and exhibits normal zoning as well. This population forms subhedral phenocrysts with core Mg# 75-77 and rim Mg# 73 (only one rim analysis was done) (Figure 19b, d). In terms of texture, it is the most stable population as it lacks disequilibrium textures and rarely contains inclusions of plagioclase (only observed in clots). The third population (1 mm) is subhedral, oscillatory, reverse-zoned augite with a fine sieved core (Figure 19c, d). With a core Mg# 75 and rim Mg# 79, it is the only population of augite that contains exsolution textures of orthopyroxene, suggesting a slow-cooling origin as a cumulate (Figure 19c). Interestingly, one augite from this population has the most Mg-rich composition of the flow unit, with a mid-zone

composition of Mg# 86, hence the description as oscillatory reverse zoning. Population 4, the most abundant, forms strong, oscillatory, reverse-zoned subhedral and euhedral phenocrysts and microphenocrysts with core Mg# 71-74 and rim Mg# 75-82 (Figure 19a, d). A wide range in size is observed (0.4-1.7 mm) and disequilibrium textures are very common, e.g., embayments and fine-grained sieves, along with occasional inclusions of oxides (Figure 19b). In summary, the most primitive augite (Mg# 81) shows some level of disequilibrium and has high concentrations of Al_2O_3 (>3.0 wt. %). The most Mg-poor augite (Mg# 71-74) shows the most extensive disequilibrium features. The other two populations (Mg# 75-77) show minimal to no disequilibrium textures.

Orthopyroxene (4-8% of phenocryst population) occurs as subhedral to euhedral microphenocrysts and phenocrysts (0.24-1.75mm) with inclusions of Fe-Ti oxides and disequilibrium textures, such as sieved cores and embayed rims. Compositions of orthopyroxene range from Mg# 68 to 85 (Table 5). Although the zonation patterns and textures of orthopyroxenes are similar to those observed in augites, orthopyroxene disequilibrium textures are far more exaggerated. Four populations of orthopyroxene are identified on the basis of textures, zoning and chemistry (Figure 20). Only one orthopyroxene from the first (rarest) population was analyzed; the only weakly, oscillatory, normal-zoned orthopyroxene (0.8 mm) identified. With a slight sieved core and exsolution, this euhedral population has core Mg# 77 and rim Mg# 76 (Figure 20a, e). The second population of orthopyroxene (0.4 mm) is characterized by euhedral microphenocrysts that lack disequilibrium textures (Figure 20b). This weak reversely-zoned population has core Mg# 73-74 and rim Mg# 75, and relatively elevated Al_2O_3 contents (1.7-1.9 wt. %) (Figure 20e, f). The third population (0.5-1.5 mm) occurs as

subhedral to euhedral, oscillatory, reverse-zoned phenocrysts. This population is characterized by their reactions rims composed of augite (Figure 20c). Disequilibrium textures are inconsistent in this population, where some contain slight-sieved cores and others are unsieved, and one grain displays minor exsolution. Analyzed core Mg# ranges from 71 to 73 and reaction rims of augite range from Mg# 72 to 85 (Figure 20e). The fourth population consists of anhedral to subhedral microphenocrysts (0.3 mm) that contain scarce oxide inclusions and rare embayments (Figure 20d). This population is weakly reversely zoned (core Mg# 68-72 and rim Mg# 70-72) (Figure 20e). In summary, the most primitive orthopyroxene (Mg# 77) shows some level of disequilibrium and is the only normally zoned population. The next most Mg-rich population (Mg # 73-74) has high concentrations of Al_2O_3 (> 1.5 wt. %) and lacks disequilibrium textures. The other two intermediate populations (Mg# 68-73) show the most extensive disequilibrium features.

Olivine (typically 2-10% of the phenocrysts) occurs as equant, anhedral to euhedral microphenocrysts and phenocrysts (Figure 21), with four population types. The typical size range of olivine is 0.25-1.0 mm, but olivine crystals as large as 3 mm (not analyzed) are found in the sample with the highest percentage of olivine (i.e., sample *adb*-02). Olivine compositions range from Fo 66 to 88 (Table 6). The first population of olivine (0.3-0.5 mm) is found in single-mineral clusters (glomerocrysts), and contains abundant chromite inclusions (Figure 21a). This population is the most forsteritic (in entire study as well) with a core composition of Fo_{88} and forms very euhedral phenocrysts with normal zoning (rim Fo_{83}) (Figure 21a, e). The second population of olivine (0.3-1.0 mm), the most abundant, forms subhedral phenocrysts that also commonly form glomerocrysts

(Figure 21b). Analyzed cores for this population range from Fo_{84-86} and contain an abundance of chromite inclusions (Figure 21b, e). With normal zoning patterns, this population has a wide range of rim compositions (Fo_{66-75}) (Figure 21e). Population 3 of olivine forms anhedral microphenocrysts (0.25-0.4 mm) and ranges from Fo_{76-80} in core composition (Figure 21b, e). Inclusions are entirely absent in population 3. The fourth population of olivine is rare and only one was analyzed. Also lacking inclusions, population 4 forms equant, subhedral microphenocrysts (0.3 mm) with a core composition of Fo_{71}, the most fayalitic (Figure 21d, e). In summary, the two most forsteritic populations of olivine (Fo_{84-88}) lack disequilibrium textures and commonly occur as glomerocrysts with abundant inclusions of chromite. The most fayalitic population (Fo_{71}) forms equant crystals that lack disequilibrium texture. The third, intermediate population of olivine (Fo_{76-80}) is the only population that shows some disequilibrium (e.g., embayments).

Fe-Ti oxides (1-6% of the phenocryst population) occur as equant anhedral to subhedral microphenocrysts and phenocrysts (typically 0.25-1.25 mm, except for sample *adb*-02, which has crystals no larger than 0.25 mm). Oxides are generally concentrated in crystal clots but also occur as inclusions in pyroxene and large plagioclase grains and as individual crystals within the groundmass. One sample (*adb*-08) contains oxides with inclusions of pyroxene. Ulvospinel has compositions of 72.1-77.0 wt. % FeO^T and 14.5-19.8 wt. % TiO_2. Ferrian ilmenite grains have compositions of 47.0-47.3 wt. % FeO^T and 47.3-48.9 wt. % TiO_2. Full compositions are presented in Table 7.

Crystal clots

Crystal clots are abundant in *adb* (3-5% of the sample) and form four distinct types on the basis of texture and mineral chemistry (Figure 22).

Crystal clot type A (Figure 22a), most abundant, is composed of predominantly orthopyroxene, ± augite and ± plagioclase and ranges in size from 1.2 to 1.5 mm at its widest diameter (Table 8). Orthopyroxene in this clot type is population 4 orthopyroxene described above (Mg# 68-72). Augite of clot type A has a narrow compositional range of Mg# 71-72 (augite population 4 described above) and is not observed in all clots of this population. Similar to crystal clot type A of *ado*, plagioclase serves as a host to orthopyroxenes of 04-clot5 (Table 8). The host plagioclase is from population 3 described above and has a core composition of An_{54}. Oxides in the clot occur as inclusions in pyroxene and as individual microphenocrysts.

Crystal clot type B (Figure 22b) consists of augite (Mg# 76), orthopyroxene (Mg# 73) and plagioclase (An_{57}) (Table 8). The size of clot type B is 1.0 mm at its widest diameter and contains oxides, generally incorporated into the crystal edges of pyroxenes but not as core inclusions. The texture of the phases in this population is more anhedral versus the subhedral nature of the phases in clot type A.

Crystal clot type C (Figure 22c) is the only olivine-bearing crystal clot. Anhedral, microphenocrystic olivine (Fo_{80}) and subhedral, microphenocrystic orthopyroxene (Mg# 73-75) are the dominant minerals, with minimal intercumulus plagioclase. The orthopyroxene in clot type C makes up phenocryst orthopyroxene population 2 described above, and olivine is phenocryst olivine population 3 described above. Oxides are abundant in clot type C, but strictly as inclusions in orthopyroxene and olivine.

Crystal clot type D (largest) of *adb* (Figure 22d) measures 4.5 mm at its widest stretch and consists of megacrystic augite and plagioclase (Table 8). Augite (Mg# 75-77) varies in size and forms subhedral to euhedral phenocrysts and microphenocrysts. Plagioclase (An_{60-61}) occurs as anhedral to subhedral phenocrysts and microphenocrysts. Microphenocrysts of plagioclase are unsieved and commonly occur as inclusions in augite, whereas phenocrysts of plagioclase are coarsely sieved. Clot type D is made up of augite population 2 and plagioclase population 1.

In summary, the variety of textures, sizes and phases comprising the crystals clots of *adb* are unique to each clot type, despite similar compositions among some populations. Crystal clot type A contains the more felsic endmember of phenocrysts, just as crystal clot type A in *ado*. The other crystal clots contain intermediate members of phenocrysts and the most mafic phenocrysts are entirely absent from crystal clots, with the exception of plagioclase, which is present in crystal clot type D. Although crystal clot types B and D have very similar mineral compositions, their crystal sizes and clot diameters are very distinct, with clot type D containing megacrysts, whereas microphenocrysts comprise clot type B. Also, crystal clot types A and B are identical to crystal clot types A and B of *ado*.

Andesite of Coleman Pinnacle (acp)

The andesite of Coleman Pinnacle (ranging from andesite to dacite in composition) is the only hornblende-bearing unit in this study. It is porphyritic with 5-20% phenocrysts of plagioclase, hornblende, augite, orthopyroxene and oxides. Although generally absent, olivine is observed in trace amounts in a few samples (e.g. *acp*-20 and *acp*-21). The

groundmass of *acp* is pilotaxitic and hypocrystalline with microlitic plagioclase, microphenocrysts of Fe-Ti oxides and pyroxenes, and portions of glass. Samples are typically not vesicular, but may have up to 5% vesicles in dacitic samples (e.g., *acp*-26). Glomerocrysts of hornblende range from 0.5 to 1.0 mm in diameter, but are rare and not observed in all samples. There is great variation among the dacites and andesites of *acp*, both petrographically (Fig. 7d-e) and geochemically.

Plagioclase (55-80% of the phenocryst population) occurs as anhedral, subhedral and euhedral microphenocrysts and phenocrysts that range in size from 0.3 to 6.5 mm. Compositions of plagioclase range from An_{28-59} (Table 3) and exhibit oscillatory zoning patterns. Three distinct textural and geochemical populations of plagioclase are identified in *acp* (Figure 23). The first population of plagioclase is characterized as subhedral microphenocrysts (0.3 mm) with an abundance of apatite inclusions. Core compositions are An_{53-60} and resorption textures are rare (Figure 23a, d). Population 2 of plagioclase forms anhedral to subhedral phenocrysts (0.75-1.2 mm) that also contain inclusions of apatite and is commonly found in crystal clots. Blebby-coarse sieves are a unique characteristic of the population and one analyzed core revealed a composition of An_{46} (Figure 23d). The third population of plagioclase forms subhedral to euhedral phenocrysts (0.7-1.5 mm) with core compositions An_{42-45} (Figure 23d). This population generally exhibits rounded edges and scattered sieves. Patchy zoning, observed in BSE, is a unique characteristic of population 3 (Figure 23b). In summary, the two most sodic populations (An_{42-46}) display extensive disequilibrium, while the most calcic plagioclase (An_{53-60}) shows minimal levels of disequilibrium.

Hornblende (10-30% of the phenocryst population) forms subhedral to euhedral, elongate and equant phenocrysts (0.5-3.75 mm). Oxidation rims and resorbed cores are common and some larger crystals even exhibit embayments (Figure 24a, b). All hornblende crystals analyzed in *acp* belong to the calcic amphibole group and are classified as magnesiohastingsite (Leake, 1978) (Table 8). Core compositions range from Mg# 71 to 77 (Figure 24d) with some crystals displaying zoning. In addition, inclusions of oxides, pyroxenes and plagioclase are common in resorbed cores and/or along reacted rims. Microphenocrysts of hornblende (0.25-0.5 mm) are also common and share similar textures, but were only analyzed in crystal clots (Mg# 74).

Augite (<1-8% of total phenocryst population) forms anhedral to euhedral microphenocrysts and phenocrysts (0.3-2.5 mm). Compositions of augite range from Mg# 69 to 82 (Table 4) and inclusions of oxides, plagioclase and apatite are common. Three distinct populations of augite are identified based on chemistry, zoning and texture (Figure 25). The first population of augite (<0.25 mm) is only observed in crystal clots (Figure 25c) and has high Al_2O_3 concentrations (3.0-4.4 wt. %) (Figure 25e). Only core analyses were taken with core Mg# 76-82 (Figure 25d) and yield the most Ca-rich augite population in the entire study, evident in Figure 6. This population is anhedral to subhedral, free of inclusions and unsieved. The second population of augite forms euhedral phenocrysts (1.25 mm) that are fine-sieved with inclusions of oxides (Figure 25b). Only one crystal from this population was analyzed and is normal-zoned with core Mg# 75 and rim Mg# 72 (Figure 25d). Inclusions of oxides, plagioclase and apatite are common along crystal edges of augite population 2. Population 3 (0.3-0.9 mm) forms anhedral to subhedral phenocrysts and microphenocrysts that are generally unsieved, with

occasional scattered coarse sieves. The population is reverse-zoned with core Mg# 69-72 and rim Mg# 70-74 (Figure 25d). Inclusions of oxides, plagioclase and apatite are commonly observed (Figure 25a). In summary, the most Mg-rich augite (Mg# 79-82) has high Al_2O_3 concentrations (> 3 wt. %) and lacks disequilibrium textures. The next most Mg-rich augite (Mg# 75) exhibits some level of disequilibrium with fine sieves. The most Mg-poor augite (Mg# 69-72) shows the most extensive disequilibrium with scattered coarse sieves.

Orthopyroxene (<1-5% of the phenocryst population) occurs as subhedral microphenocrysts and phenocrysts (0.4-1.6 mm) and only one population is identified. Orthopyroxene is reverse-zoned with core Mg# 64-68 and rim Mg# 74-76 (Table 5, Figure 24d). Reaction rims of augite along with occasional exsolution are characteristic of orthopyroxene (Figure 24c) in *acp*, and some crystals display heavily oxidized rims. Oxide inclusions are common as well.

Olivine (≤1 %) is rare (only observed in samples *acp*-20, 21 and 23), occurring predominantly as anhedral inclusions (≤ 0.25 mm) in hornblende and/or augite, but in rare cases as individual embayed phenocrysts (0.75 mm). No olivine grains were analyzed.

Fe-Ti oxides (2-8 % of the phenocryst population) form equant, anhedral to subhedral microphenocrysts and phenocrysts that are exsolved. Individual oxide microphenocrysts range in size from 0.1 to 0.5 mm, whereas oxide phenocrysts range from 0.75 to 1.0 mm and are restricted to crystal clots. Although rare, larger oxides may contain plagioclase laths as inclusions. Ulvospinel has compositions of 63.7-85.1 wt. % FeO^T and 0.2-6.3 wt. % TiO_2. Ferrian ilmenite grains, although rare, have compositions of 62.7-69.3 wt. %

FeO^T and 19.9-26.9 wt. % TiO_2. Full compositions of Fe-Ti oxides are presented in Table 7.

Crystal clots

In terms of texture and phases, several populations of crystal clots exist in the *acp* flow and vary from sample to sample. Due to the high variety of crystal clots observed, the petrography of andesitic samples (*acp*-20, 21, 22 and 24) is discussed separately from the dacitic samples (*acp*-23 and 26). However, only sample *acp*-20 was analyzed for mineral chemistry. It is important to note the andesitic samples do not have hornblende-bearing crystal clots, but the dacitic samples have one rare hornblende-bearing crystal clot type.

Two populations of crystal clots (1-2% of the rock) are identified in the andesitic samples of *acp* (Figure 26). Crystal clot type A (1.2-2.1 mm wide) contains augite, ±orthopyroxene and ±plagioclase (Figure 26a and Table 9). Augite (Mg# 70-72) is anhedral to subhedral with oxide inclusions in the core and along crystal edges. Cores of augites are often sieved. Augite in this clot is augite population 3 described above. Orthopyroxene (Mg# 64-65) is elongate and subhedral with reaction rims. Oxide inclusions are also common. Orthopyroxene in this clot correlates with the single population of orthopyroxene phenocrysts. Plagioclase (An_{46}) is subhedral and rounded with coarsely sieved mid-zones. The plagioclase commonly encompasses the augite and orthopyroxene and is much larger. Plagioclase in this clot is plagioclase population 2 described above. Inclusions of oxides are also common in plagioclase. Oxides also occur as individual, equant crystals generally along the edges of augite.

Crystal clot type B (Figure 26b and Table 9) contains anhedral, microphenocrystic augite, ±orthopyroxene, ±plagioclase and ±olivine. Olivine was not analyzed, as it is

extremely rare and was not present in the analyzed clots. Augite (Mg# 76-82) is augite population 1 described above. Orthopyroxene (Mg# 66) is similar in composition to individual orthopyroxene phenocrysts. Plagioclase (An_{59}) is plagioclase population 1 described above.

In summary, crystal clot type A represents the most felsic endmember phenocrysts and is the most common. Crystal clot type B is rare and represents the most mafic endmember of phenocrysts. This is the only olivine-bearing crystal clot.

Although not geochemically analyzed, olivine-bearing versions of crystal clot type B exist in other andesitic samples of *acp,* as mentioned above. When present, olivine is highly altered and barely recognizable (Figure 27a). In addition, other versions of this clot type clearly contain two populations of plagioclase, shown by the larger, euhedral plagioclase with inclusions and the smaller, subhedral plagioclase interlocking with the other minerals. Size range for clot type B is 3.5 to 4.0 mm in *acp*- 21 and 22. This clot type is observed in *acp*-24 as well, but much smaller in size (0.75-1.0 mm).

Another crystal clot observed in one andesitic sample (*acp*-24) is characterized as predominantly equant, granular orthopyroxene with oxide crystals as well (Figure 27b) but is extremely rare (<1%).

Three types of crystal clots (≤1% of the sample) are observed in the dacitic samples of *acp*, based on texture and modes: 1) subhedral well-zoned plagioclase and oxides (Figure 27c) that range in size from 0.5 to 0.75 mm, 2) large subhedral plagioclase and hornblende with inclusions of oxides, and smaller, equant oxides (Figure 27d). The minerals are more similar in size in *acp*-26 and more euhedral. The size range of the population is 0.75 to 2.25 mm, and 3) the same as clot type B in the andesitic samples,

with the exception that the pyroxenes observed in *acp*-26 are altered to resemble hornblende.

In addition to crystal clots, meta-plutonic xenocrystic clots (<1% of the sample) are also observed in the andesitic samples of *acp*. Three xenocrystic clots are identified: 1) microphenocrystic hornblende and pyroxenes with interstitial plagioclase in a spinifex, lath-like habit. The pyroxenes are highly unstable and contain reaction rims. The size range is 0.75 to 1.5mm and is observed in *acp*-21 and 24, 2) granular orthopyroxene and oxides dispersed in groundmass. Orthopyroxene in this xenocrystic clot contains exsolution of oxides. This xenocrystic clot is 1 mm in size and observed in *acp*-22, 3) large, subhedral hornblende with large, equant oxides surrounding plagioclase and heavily corroded augite and orthopyroxene that contain oxide exsolution. This xenocrystic clot is observed in *acp*-26 and is 2.25 mm in size.

In summary, distinct crystal clots exist in the dacitic samples of *acp* that clearly have different origins than andesitic crystal clots. In the following section, whole rock data also suggests that the geochemical signature of the dacitic samples of *acp* are clearly influenced by an additional component.

Whole Rock Chemistry

Major, minor and trace element data of all analyzed flow units are presented in Table 2. Based on the criteria of Irvine and Baragar (1971), all flow units analyzed are subalkaline, with the exception of the most mafic samples from andesite of Coleman Pinnacle (*acp*), which extend into the alkaline field (Figure 28). Although termed "andesites" by Hildreth et al. (2003), the andesites of Swift Creek (*asw)*, Dobbs Creek

(*ado*), Dobbs Cleaver (*adb*) and Coleman Pinnacle (*acp*) encompass a wider range of rock names based on the nomenclature of Le Maitre et al. (1989), extending from basaltic andesite to trachydacite. In addition, *asw*, *ado* and *adb* are classified as medium-K and *acp* is classified as high-K using fields defined by Le Maitre et al. (1989) (Figure 29).

Due to the drastic difference in composition and mineralogy between the high-K, hornblende-bearing *acp* and the medium-K, hornblende-free *asw*, *ado* and *adb*, the succeeding sections describe their whole rock chemistry in separate sections. Major element data for *asw*, *ado* and *adb* exhibit linear trends on major and trace element Harker diagrams (Figures 30-31). The high-K *acp* flow unit forms a linear major and trace element data trend of its own on Figures 30 and 31. This unit compositionally overlaps the younger 149±5 ka dacite of Nooksack Falls (Gross, 2012), which is the only other hornblende-bearing flow unit in MBVF. Whole rock compositional data of other MBVF flow units from Baggerman and DeBari (2011), Moore and DeBari (2012) and Gross (2012) are included in Harker diagrams to illustrate trends (or lack thereof) among flow units, and on trace element normalization diagrams for comparison.

Medium-K: Andesites of Swift Creek, Dobbs Creek and Dobbs Cleaver

The medium-K, calc-alkaline andesites of this study are dominantly basaltic andesite to andesite, but the more silica-rich samples border on the trachyandesite field (Le Maitre et al., 1989) (Figure 28). Each flow unit is relatively homogenous in both major and trace elements concentrations, with the exception of MgO, Na2O, Cr, Ni and Rb (Figures 30-31). The most mafic flow unit of the study, *asw*, has a silica range of 55.9-56.2 wt. % and is technically a basaltic-andesite. The *ado* flow unit is the most homogenous flow unit in

this study with 56.6-56.9 wt. % SiO_2 and straddles the border of basaltic-andesite to andesite. The *adb* flow unit (58.6-59.6 wt. % SiO_2) straddles the border of andesite and trachyandesite.

As the most mafic flow unit in the study, *asw* is the most enriched in MgO (5.7-6.2 wt. %) and the poorest in K_2O (0.97-1.3 wt. %) (Figures 29, 30). The *asw* flow unit is the most enriched in Ni (60-67 ppm) and Cr (182-203 ppm), has the widest range in Rb concentrations (19.3-30.5 ppm), but is relatively homogenous in the other trace elements (Figure 31). The *ado* flow unit is similar to *asw* in major element composition, but is more homogenous (Figure 30). Though *ado* is more evolved than *asw*, it has the lowest concentrations of Y (20.0-20.6 ppm), La (15.6-16.0 ppm) and Zr (148-153 ppm) (Figure 31). The *adb* flow unit (58.6-59.6 wt. % SiO_2) is the most varied medium-K flow unit in the study and has the widest compositional ranges for MgO, CaO, Mg# and Na_2O concentrations (Figure 30). Concentrations of Cr and Ni in *adb* illustrate that the flow unit is more evolved that the *asw* and *ado* flow units (Figure 31). However, despite its higher silica content, *adb* shares similar concentrations in Rb and La with *asw*, and is the most depleted in Sr (645-670 ppm) (Figure 31).

In summary, the medium-K flow units exhibit decreasing MgO, CaO, and Mg# with increasing SiO_2 whereas P_2O_5, Na_2O and FeO^T/MgO increase with increasing SiO_2. TiO_2 and Al_2O_3 remain relatively constant with increasing SiO_2 (Figure 30).

In terms of trace elements, the medium-K andesites decrease in Cr and Ni concentrations with increasing silica as expected. Interestingly, trends of Rb, Y, Ba, La and Zr show a decrease in concentrations from *asw* to *ado* with increasing SiO_2. The opposite is true of Sr, where concentrations increase from *asw* to *ado*. However, the more

evolved *adb* does not follow this pattern, suggesting it is not cogenetic with *asw* and *ado*. Incompatible trace element (ITE) concentrations, normalized to primitive mantle (Sun and McDonough, 1989) of the medium-K andesites display a significant amount of variation. The *adb* flow unit has the highest concentrations of ITEs of the medium-K andesites (Figure 32). The *asw* and *ado* flow units have the lowest concentrations in ITEs and overlap each other in concentrations of Rb, Ba and Th. Despite the fact that *asw* is the most mafic flow unit, the *ado* flow unit has the lowest concentrations of Ta and Nb. All medium-K andesites display a negative Ti anomaly and a spike in Sr concentrations. Medium-K andesites have shallow rare earth element (REE) patterns, $(La/Yb)_N$ = 5.2-5.8 and small negative Eu anomalies (Eu/Eu* = 0.86-0.98) (Figure 33). REE abundances of the medium-K andesites do not correlate with their SiO_2 content. For example, despite *asw* being the most mafic flow unit with the shallowest REE patterns, *ado*, more differentiated, has the lowest concentrations of light rare earth elements (LREE), middle rare earth elements (MREE) and heavy rare earth elements (HREE). Though similarities in LREE and MREE concentrations exist among *ado* and HMA of Glacier Creek (Baggerman and DeBari, 2011), the differences in HREE concentrations make their REE patterns distinct. The *adb* flow unit has HREE concentrations similar to the CA basalts of Lake Shannon (Moore and DeBari, 2012); however, differences in LREE and MREE concentrations produce distinct patterns as well.

In summary, the medium-K andesites often overlap in concentrations of ITEs and have shallow REE patterns. However, REE abundances do not correlate with degree of differentiation. Overall, REE concentrations of the high magnesium basaltic andesite

(HMBA) of Tarn Plateau are parallelly similar (Figure 33), suggesting the medium-K andesites may represent differentiates of Tarn Plateau HMBA.

High-K: Andesite of Coleman Pinnacle

The andesite of Coleman Pinnacle (*acp*) is the only andesite in this study that contains amphibole and is also the most compositionally diverse flow unit in the study. With samples extending well into the alkaline field, variation in the *acp* flow unit is bimodal with trachyandesites (57.7-60.1 wt. % SiO_2) and trachydacites (64.2-64.8 wt. % SiO_2), which overlap the dacite of Nooksack Falls (Gross, 2012) (Figure 28). Elevated K_2O concentrations (2.81-3.00 wt. %) classify the *acp* samples as high-K (Figure 29) and display minimal variation over a wide range of silica content. The *acp* flow unit also has noticeably elevated concentrations in Na_2O (4.72-4.98 wt. %) and P_2O_5 (0.24-0.50 wt. %) and much lower MgO (1.51-3.24 wt. %) and Mg# concentrations, relative to the other flow units in this study (Figure 30). The most Si-poor samples of *acp* share similar concentrations in TiO_2, Al_2O_3, CaO and FeO^T/MgO to the *adb* flow unit. The elevated concentrations of La (27.2-39.7 ppm) and Ba (852-1000 ppm) in *acp* appear to behave compatibly, showing decreasing trends with increasing SiO_2 (Figure 31). In addition, concentrations of Sr (622-2209 ppm) in *acp* are highly elevated and illustrate a trend independent of other flow units. As expected given its higher SiO_2 content, the acp flow unit has the lowest concentrations in Cr (3.38-26.4 ppm) and Ni (3.48-23.6 ppm).

In summary, *acp* exhibits decreasing TiO_2, P_2O_5, MgO, CaO and Mg# with increasing SiO_2, whereas, FeO^T/MgO increases with increasing SiO_2. Al_2O_3 and Na_2O remain relatively constant with increasing SiO_2 (Figure 30).

In terms of trace elements, concentrations of Rb, Y, and Zr illustrate similar trends as the other flow units. However, *acp* trend lines formed by concentrations of Cr, Ni, Ba, La and Sr are distinct from the other flow units. Samples from *acp* have the highest concentrations of ITEs with elevated values for Ba, Th, U, K, Pb, Sr, P, Zr, and Hf (Figure 32). However, the *acp* flow unit has the strongest negative Ti anomaly and the lowest LREE concentrations. ITE concentrations of the dacitic samples of *acp* are mirrored by concentrations of the dacite of Nooksack Falls (Gross, 2012). The andesitic samples of *acp* have higher LREE and other ITE concentrations than the dacitic samples (Figures 32 and 33). HREE concentrations of *acp* span the widest range and have both the most elevated and lowest concentrations of Yb (1.7-2.8 ppm) and Lu (0.25-0.46 ppm). Given the elevated concentrations of LREEs and wide range of HREEs, REE patterns of *acp* are steeper than the other flow units with $(La/Yb)_N$ = 7.7-17.1. The andesitic samples display the steeper range of patterns, whereas the dacitic samples display more shallow patterns. Although small, *acp* has the widest range in Eu anomalies with Eu/Eu* ranging from 0.77 to 0.9. Also, *acp* spans the widest range in Sr concentrations (622-2209 ppm), with the andesitic samples having the higher concentrations (1270-2209 ppm) and the dacitic samples with the lowest concentrations (622-704 ppm).

In summary, ITE and REE concentrations of the dacitic samples of *acp* are nearly identical to the compositions of the dacite of Nooksack Falls (Gross, 2012), the only other hornblende-bearing flow unit of MBVF (Figures 32-33), even with the ~200 ka difference in age. Surprisingly, andesitic samples of *acp* are more elevated in their concentrations of LREEs, MREEs and several ITEs. Overall, the *acp* flow unit exhibits

remarkable variation in major and trace element data and exhibits geochemical trends independent of the other flow units.

Intensive Parameters

Temperature and Pressure

The *Fe-Ti oxide geothermobarometer* of Andersen and Lindsley (1985) in the ILMAT (excel worksheet for ilmenite-magnetite for geothermometry and geobarometry) spreadsheet of Lepage (2003) was used to constrain pre-eruptive temperatures of all four intermediate flow units. ILMAT calculates several values using multiple methods under the geothermometer of Andersen and Lindsley (1985) and Andersen et al. (1993). For consistency, only calculations of the QUILF (Quartz, Ulvospinel, Ilmenite, Fayalite) method (Andersen and Lindsley, 1988) were considered and are presented in Table 10. Coexisting magnetite and ilmenite pairs were selected, when available, based on the criteria discussed by Bacon and Hirschman (1988). Only exsolved Fe-Ti oxide pairs exist in *acp*, therefore no temperatures are constrained for *acp* through this method. Unexsolved ilmenite grains are rare in *ado* and only one pair was used.

Three pairs were analyzed for *asw* and yielded pre-eruptive temperatures ranging from 919 to 964 °C. One pair from *ado* yields a temperature of 756 °C. Three pairs were analyzed for *adb*, which yielded pre-eruptive temperatures ranging from 778 to 856 °C.

The *two-pyroxene thermobarometer* of Putirka (2008) was used to calculate temperatures and pressures of pyroxene pairs. Selections of pyroxene pairs (augite and orthopyroxene) were based on type (phenocrysts vs. crystal clots), textures, and

composition (Mg-rich vs. Mg-poor). Pyroxene pairs and temperatures are presented in Table 11.

Pyroxene pairs from *asw* provided temperatures ranging from 980 to 1089 C° for phenocrysts and 989 to 1010 C° for crystal clots. These temperatures are higher than those calculated from Fe-Ti thermometry (919-964 C°). The most mafic pyroxene pair (population 1 of augite and orthopyroxene) yields the highest temperature of 1089 C° and a pressure of 4.5 kbar. The most felsic pyroxene pair (population 5 of augite and orthopyroxene) yields the lowest temperature of 980 C° and a pressure of 6.3 kbar. In addition, this felsic, reverse-zoned pair yields a rim temperature of 1048 C° and pressure of 2.4 kbar. Three intermediate pairs from crystal clots (population 2 of augite and orthopyroxene in crystal clot type A) yield a temperature range of 989-1010 C° and pressure range of 2.4-3.7 kbar.

For *ado*, pyroxene pairs provide a temperature range of 967-981 C° and a crystal clot pair yields a temperature of 1025 C°. Calculated temperatures of *ado* from two-pyroxene thermometry are significantly higher than the temperatures calculated from Fe-Ti thermometry (756 C°). The most mafic pair (population 1 of augite and orthopyroxene) yield the lowest temperature of 967 C° and pressure of 1.4 kbar. The most felsic pair (population 4 of augite and population 2 of orthopyroxene) yield a temperature of 981 C° and pressure of 5.2 kbar. This felsic, unzoned pair (population 4) produces a slight lower rim temperature of 980 C° and pressure of 4.1 kbar. One crystal clot pair (population 4 of augite and population 2 of orthopyroxene of crystal clot type B) yield the highest temperature of 1025 C° and pressure of 4.4 kbar.

Pyroxene pairs from *adb* provide temperatures ranging from 969 to 1006 C° for phenocrysts and 939 to 1000 C° for crystal clots. These temperatures are significantly higher than those produced from Fe-Ti thermometry (778-856 C°). The most mafic pair (population 1 of augite and orthopyroxene) yields a temperature of 969 C° and 2.2 kbar. The most felsic pair (population 4 of orthopyroxene and augite) yields the highest temperature of 1006 C° and pressure of 4.1 kbar. This felsic (population 4), reverse-zoned pair yields a rim temperature of 969 C° (identical to mafic pair core temperature) and pressure of 1.4 kbar. One crystal clot (type A), also consisting of population 4 augite and orthopyroxene, produces a similar temperature of 1000 C° and pressure of 4.0 kbar. An additional, more mafic, crystal clot (population 2 of augite and orthopyroxene of crystal clot type B) yields a temperature of 939 C° and pressure of 1.3 kbar.

The *acp* flow unit contains one population of orthopyroxene; all with reaction rims of augite, therefore temperatures for *acp* have the narrowest range (937-952 C°). The third population of augite is the most likely to have co-crystallized with the one population of orthopyroxene; therefore, all temperatures and pressures calculated use population 3 of augite. Phenocryst pairs yield a temperature range of 937-952 C° and pressure range of 5.8-7.4 kbar. The crystal clot pair from clot type A produces a temperature of 944 C° and pressure of 7.9 kbar. Since all orthopyroxene "rims" are reaction rims of augite, calculations of rim temperatures and pressures are not feasible.

Generally, temperature and pressure calculations of pyroxenes are proportionally related, where the higher the temperature, the higher the pressure. The calculated temperatures and pressures of the pyroxene pairs mentioned above contradict each other in that the mafic pairs (higher temperatures) yielded the lowest pressures and more felsic

pairs (lower temperatures) yielded the highest pressures. One reasonable explanation for this is that the pyroxenes in this study did not reach Al-Na-Ca exchange equilibrium, resulting in inaccurately high-pressure calculations (per conversation with Keith Putirka). Instead, low concentrations of Na and Jd in the pyroxenes of this study suggest they formed at low P (per conversation with Keith Putirka). Based on such observations and an average of the calculated results, the pyroxenes in this study most likely crystallized at temperatures around 990 C° and 2.5 kbar. The exception is the high-Al pyroxene pair of *asw* (population 1, Table 12), which yielded the highest temperature (1089 C°) and high pressure (4.5 kbar). This exceptional case is in agreement with Gasparik (1984), where high Al_2O_3 concentrations of pyroxenes are indicative of high-pressure crystallization. Due to the overall error in pressure calculations, only calculated temperatures and Al_2O_3 concentrations (as a quasi-barometer) of pyroxenes will be utilized in the succeeding section for interpretations.

Discussion and Interpretation

The purpose of this discussion is to use the mineral populations described above to elucidate processes of magma evolution at MBVF. Three primitive magma types have been identified at MBVF using whole rock and mineral studies (Moore and DeBari, 2012): 1) typical calc-alkaline basalt (CAB), 2) high-Mg basaltic andesite (HMBA) and 3) MORB-like low K tholeiite (LKT). The high-Mg basaltic andesites are likely parental to dacitic compositions by fractional crystallization, and these dacites clearly undergo recharge mixing with more primitive compositions to provide complex differentiation histories (Gross, 2012; Baggerman and DeBari, 2011).

Intermediate magmas at MBVF are clearly not derived from a single source, and open-system processes are dominant during petrogenesis (Baggerman and DeBari, 2011). In this study, our approach is to use mineral textures and geochemistry in intermediate andesites (54-60% SiO_2) to interpret some of the details of these open system processes.

MBVF lavas are notorious for their various populations of phenocrysts (based on their chemistry and textures) and abundance of crystal clots (Green, 1988; Hildreth et al., 2003; Garcia, 2008; Baggerman and DeBari, 2011; Gross, 2012). Baggerman and DeBari (2011) and Gross (2012) identified two crystal clot types within single flow units using mineral assemblages and textures but provided limited interpretations. Although Gross (2012) includes chemistry of crystal clot phenocrysts, the compositions are presented individually, rather than as crystal clot assemblages of mixed minerals, and hence interpretation of their relationship to magma petrogenesis is limited.

These previous studies have assisted immensely in decoding the complex petrogenetic history of MBVF. However, the heavy reliance on whole rock data without close examination of associated phenocrysts leads to over-simplified models of petrogenetic process (Streck et al., 2005). The exception at MBVF is Sas (2015), who used clinopyroxene textures and chemistry in HMBA and high magnesium andesites (HMA) to disentangle subducted slab versus crustal input to magma generation and evolution processes. The following discussion delves even more deeply into the powerful role that crystals and crystal clots can play in interpreting the differentiation processes responsible for generating the intermediate magmas of the MBVF.

Origin of crystal clots and relation to phenocrysts, evidence for incorporation of open-system, crystal-mush accumulation

The origin of crystal clots has been discussed in other studies (e.g., Wilkinson et al., 1964; Stewart, 1975; Scarfe and Fujii, 1987), but those discussions do not provide consensus, despite their abundance in lavas of the Cascade arc of western North America (e.g., Stewart, 1975; Garcia and Jacobson, 1979; Scarfe and Fujii, 1987; Clynne and Borg, 1997; Baggerman and DeBari, 2011; Gross, 2012). Crystal clots were initially presumed to have formed through the random accumulation of phenocrysts (reported by Gill, 1981). In one of the earliest studies of crystal clot-bearing lavas of the Cascade arc, Stewart (1975) proposed that crystal clots form through the breakdown of high-Al amphiboles, as the amphibole reacts with a melt in a low-pressure environment. Garcia and Jacobson (1979) disagreed with that interpretation, citing the absence of a "relict amphibole crystal outline and a fine-grained metamorphic texture". Garcia and Jacobson (1979) further state that the euhedral-subhedral and oscillatory-zonation textures of plagioclase in the crystal clots could not have formed from the breakdown of amphiboles. However, they fail to offer an alternate explanation, suggesting support for the random accumulation hypothesis.

If all phenocrysts (in both crystal clots and isolated crystals) show evidence of having crystallized from the host liquid (or are in equilibrium with the bulk rock), then presumably the crystal clots are derived from the liquid as well and do form through random accumulation. However, in this study it is clear that there are different types of crystal clots, each clot type bearing its own distinctive mineral geochemical and textural signature (Table 8), and these signatures are sometimes different from the isolated

phenocrysts (e.g. distinct Mg # and/or textures). This evidence suggests that crystal clots are not always related to each other and clearly must be derived from different parent magmas. In other words, this study refutes the random accumulation hypothesis as the sole explanation for the abundant crystal clots present in MBVF lavas.

Other hypotheses for the origin of crystal clots include: 1) "compositionally modified crystalline residuals from partial melting" (Flood et al., 1977), 2) crystallization and settling of minerals from the host magma (Arculus, 1976), 3) accidental inclusions of country rock xenolithic material (Wilkinson et al., 1964), and 4) disruption and entrainment of cumulate material (Arculus and Wills, 1980; Conrad et al., 1983). Hypothesis 1 can be ruled out given the lack of evidence for textures and chemistry indicative of partial melting. Hypothesis 2 implies that minerals would be of a single composition in equilibrium with the host. This is not viable given the evidence of more than one clot type, and varied geochemical "signatures" of clots presented above. Thus hypotheses 3 and 4 in this list are the most supportable.

Confusion lies in the distinction between hypotheses 3 and 4 in that the terms "cumulate" and "xenolith" are often used interchangeably in the literature. Wilkinson et al. (1964) refer to dioritic clots and early-phase clots as "xenoliths", even though they make it clear that they are derived from the same magmatic system, therefore of cumulate origin. The third "xenolith" that Wilkinson et al. (1964) describe is country rock inclusions with distinct mineralogy, therefore truly "foreign" material. In the case of hypothesis 4, Arculus and Wills (1980) refer to cumulate material as "xenoliths" as well, but with a clear explanation of having been derived as cumulates from the main magmatic system. They refer to "foreign" xenoliths as "metamorphic" xenoliths, even

though they may include meta-igneous and meta-sedimentary rock types. Conrad and Kay (1984) also refer to cumulate material as "xenoliths" with the interpretation that they represent a continual record of crystallization of basaltic magmas in the lower crust and upper mantle.

In this study, because the crystal clots are not "metamorphic" they are not referred to as xenoliths, in the same way that the term xenocryst is avoided to describe certain populations of crystals (see previous section for explanation). Refraining from using the term "xenolith" does not suggest that all crystal clots and phenocrysts are cognate (of the same parental liquid), but rather that they are derived from different episodes of magmatism at the MBVF. Though it can be argued that crystal clots and related individual phenocrysts may be derived from "foreign" country rock, the fact that mineral compositions, textures and phases present in crystal clots resemble individual phenocrysts across all flow units is strong evidence for an origin as cumulates from related magma types (Scarfe and Fujii, 1987; Amma-Miyasaka and Nakagawa, 2003), although not necessarily cognate.

I propose that the abundant crystal clots found in the intermediate magmas of MBVF represent cumulate material entrained in the erupting liquid as proposed by Arculus and Wills (1980). Evidence to support this hypothesis includes the observation that: 1) crystal clots are not metamorphic, they are clearly igneous, 2) crystal clots do not contain multiple populations of a single mineral; 3) multiple populations of crystal clots (and hence crystallizing assemblages) exist in a single flow unit, and this same range of crystallizing assemblages is found in all flow units, regardless of whole rock bulk composition; 4) some crystal clots appear to be caught in the act of disaggregating (e.g.,

crescent shaped crystal clots and smaller clots near larger, identical clots) to form isolated phenocrysts; 5) phases present as phenocrysts and crystal clots are identical; and 6) interstitial glass and relict amphibole outline are absent.

Assessment of mineral populations and crystallized assemblages: evidence for open-system processes

In the following discussion, I use the multiple populations of mineral phases found within a flow unit (as presented in Tables 2-7 and Figures 8-27) to characterize ***co-crystallizing assemblages*** using the correlation of mineral chemistry, textures, and zoning patterns at the scale of a thin section. These co-crystallizing assemblages are presented in Table 12, with the rationale for each flow unit described below. Each crystallizing assemblage is assigned a letter indicating the likely magmatic composition from which it crystallized (e.g., B=basalt, BA=basaltic-andesitic, A=andesitic, D=dacitic), followed by a number to differentiate between multiple assemblages from a similar parental liquid type. Potential parental magmatic compositions for each proposed crystallizing assemblage is derived from previous studies of mineral populations in arc lavas of Mount Shasta (Streck et al., 2007), Lassen Peak (Clynne, 1999) Arenal volcano, Costa Rica (Streck et al., 2005) and Miyake-Jima volcano, Japan (Nakagawa et al., 2002 and Amma-Miyasaka and Nakagawa, 2003). In these studies, the authors relate Mg#, Fo and An content of minerals to magma types for interpreting magmatic components involved in open system processes. This categorization of co-crystallizing assemblages and their proposed magmatic components aids in identifying the range of possible open system

inputs involved in the petrogenesis of all flow units (e.g., B1 assemblage is observed across all medium-K flow units).

The minerals within a crystal clot have textures that indicate co-crystallization and are therefore grouped into the same co-crystallizing assemblage as they can be interpreted to have crystallized concurrently from the same magma (Amma-Miyasaka and Nakagawa, 2003). Although there is no way to tell that every specific crystallizing assemblage type (e.g., B1) crystallized concurrently, textures clearly indicate that all minerals within one individual crystal clot crystallized at the same time. It is possible that a specific crystallizing assemblage type (e.g., B1) could be crystallizing from similar parental magmas throughout the history of MBVF and have spread out all over the mid/lower crust or that there is only one magma pocket responsible for a specific crystallizing assemblage.

Finally, although each mineral population has a distinct textural and geochemical signature, there is some overlap in two or more populations. In addition, not all analyzed grains in a given population have identical chemistry. In several cases, one grain could have belonged to either of two populations, hence the overlap. Assignation to a population is therefore subjective in some cases, but uses the combination of chemistry and textural features.

The andesite of Swift Creek (asw)

The andesite of Swift Creek is the most mafic of the calc-alkaline flow units based on whole rock geochemistry (55.9-56.2 wt. % SiO_2, 5.7-6.2 wt. % MgO, 60-67 ppm Ni) (Figure 28, 30 and 31). Interestingly, this flow unit yielded one of the widest ranges of

mineral populations (Tables 2-7 and Figures 8-12). In general, the most mafic (e.g., Mg#, An) population of each mineral (both phenocrysts and crystal clots) lacked or had only minimal disequilibrium textures, whereas intermediate and felsic end members (only isolated phenocrysts) of mineral phases showed some level of disequilibrium. As described in the petrography section above, the mineral populations identified in *asw* include (both phenocrysts and crystal clots): four plagioclase populations (1:An_{69}, 2:An_{57-67}, 3:An_{52}, 4:An_{46}; Figure 8), five augite populations (1:Mg#81-85, 2:Mg#78-83, 3:Mg#79-82, 4:Mg#75, 5:Mg#72; Figure 9), five orthopyroxene populations (1:Mg#77-79, 2:Mg#76-79, 3:Mg#72, 4:Mg#68, 5:Mg#65-68; Figure 10) and one olivine population (Fo_{85-87}; Figure 11). I assign each of these diverse mineral populations to co-crystallizing assemblages in the following paragraphs, with results summarized in Table 12.

Populations 1 and 2 of augite and orthopyroxene overlap in core chemistry (see previous paragraph) and exhibit normal zoning, but they differ in Al_2O_3 compositions, suggesting that the higher Al_2O_3 pyroxenes crystallized at higher pressures (e.g., Gasparik, 1984). Both populations, in addition to the sole olivine population, are in or near equilibrium with the bulk rock Mg# of *asw*-31 and -35 (Figure 34). Because of this, the bulk rock Mg# is probably very similar to the liquid composition that crystallized olivine and pyroxene populations 1 and 2, and can be equated to a "host liquid" that incorporated other assemblages/populations.

The high-Al augites of population 1 (4.2-4.9 wt. % Al_2O_3), along with population 1 of orthopyroxene and plagioclase, are found as isolated phenocrysts and in crystal clots (Figure 12: sub-type clot A and clot type B). These three mineral populations presumably co-crystallized as clumps to from crystal clots, and individual phenocrysts were derived

by their disintegration. This assemblage of minerals is understood to have crystallized from a basaltic to basaltic-andesitic magma, therefore named the B1 assemblage (Table 12).

Population 2 of the pyroxenes is found in crystal clot A, as well as population 2 of plagioclase, and the one population of olivine (Figure 12). Therefore, these four mineral populations presumably co-crystallized and individual phenocrysts of population 2 minerals were derived by their disintegration. This assemblage of minerals is understood to have crystallized from a basaltic to basaltic-andesitic magma as well, but lower Al concentrations in augite population 2 (2.1-3.3 wt. % Al_2O_3) and the presence of olivine suggests a distinct crystallization history, therefore named the B2 assemblage (Table 12) to differentiate.

Together, populations 1 and 2 of pyroxenes in *asw* are of similar composition, and suggest crystallization from a mafic host magma, perhaps at varying depths as the magma rose through the crust. This is supported by the fact that the B1 assemblage contains the higher-Al pyroxenes and lacks olivine, whereas the B2 assemblage lacks high-Al pyroxenes and does contain olivine. Müntener et al. (2001) report that olivine is not on the liquidus at pressures higher than 1.2 GPa in basaltic and basaltic andesite magmas. Furthermore, textures support the notion that the two assemblages have different crystallization histories where the B1 assemblage augites are generally euhedral and lack disequilibrium textures and the B2 assemblage augites are occasionally sieved and exhibit patchy zonation.

Populations 3 of augite, orthopyroxene and plagioclase all display great degrees of disequilibrium (sieve textures and exsolution) and exhibit reverse compositional zoning.

The similarity in disequilibrium features of these mineral populations suggests they crystallized together (Table 12). The most likely interpretation of the reverse zoning is an immersion in a more mafic magma that already contained the most mafic end-members of mineral populations. After immersion, rim growth on population 3 minerals proceeded with compositions similar to the minimally zoned compositions of the mafic endmembers described previously. It is evident from these observations that population 3 minerals originated from a more differentiated magma than the current host rock, likely a basaltic-andesitic magma, therefore named the BA1 assemblage (Table 12).

Populations 4 of augite, orthopyroxene and plagioclase provide a paradox in that they are an even more felsic assemblage than population 3, but they exhibit *normal* zoning. A permissible interpretation would be that this assemblage spent the least amount of time residing in the host magma; they were incorporated just before or during eruption, hence the absence of reversely zoned rims. Their core compositions suggest they crystallized from an andesitic magma, therefore named the A1 assemblage (Table 12).

The most felsic assemblage consists of population 5 of augite and orthopyroxene. Similar to the BA1 assemblage, this group exhibits disequilibrium features and reversely zoned rim compositions representative of the mafic endmember populations. The strong reverse zoning is clear evidence for this assemblage to have been incorporated early into the mafic host magma from a more differentiated magma. Compositions of this assemblage suggest it crystallized from an andesitic to dacitic magma, named the D1 assemblage (Table 12).

In summary, mineral populations with their proposed crystallized assemblages suggest a minimum of four distinct magmatic components (Table 12). A mafic magmatic

component(s) (presumably the host magma) crystallized the two most mafic assemblages of mineral populations, which is also the source for the abundant crystal clots. As this mafic component ascended through the crust, it plucked cumulates (crystal clots A and B, along with sub-types), presumably from its own chamber. The Mg# of the ferromagnesian minerals in the B1 assemblage (Table 12) suggest that this mafic component was a basalt or high-magnesium basaltic andesite. The other three assemblages, intermediate and felsic, could have been sourced from either contamination as the magma passed through other crystal mushes, magma mixing with more evolved liquids, or a combination. However, their influence on the bulk rock chemical signature is minimal, suggesting they are likely liquid-poor crystal mushes. The fact that the most mafic assemblages, B1 and B2, are nearest in equilibrium with the bulk rock Mg# (Figure 34) and texturally supports this hypothesis.

The andesite of Dobbs Creek (ado)

The *ado* flow unit is very similar in composition to *asw* (56.6-56.9 wt. % SiO_2, 5.2-5.5 wt. % MgO, 58-61 ppm Ni), but has a slightly steeper REE pattern (Figure 33). It has a complex set of mineral populations (Tables 2-7 and Figures 13-17), though not as extensive as *asw*. The most mafic and most felsic end member mineral populations show the *least* extent of disequilibrium textures, while the intermediate populations show textures indicative of extensive disequilibrium. Mineral populations identified in *ado* include: four plagioclase populations (1:An_{59-64}, 2:An_{54-59}, 3:An_{47-48}, 4:An_{45}; Figure 13), four augite populations (1:Mg#84, 2:Mg#82, 3:Mg#75, 4:Mg#70-73; Figure 14), two orthopyroxene populations (1:Mg#72-74, 2:Mg#69-70; Figure 15) and two olivine

populations (1:Fo_{72-74}, 2:Fo_{69-70}; Figure 16). Co-crystallizing assemblages for these diverse populations are assigned in the following paragraphs.

Populations 1 of orthopyroxene, augite, and plagioclase are the most mafic and occur as coexisting minerals in crystal clots (except augite) and as individual phenocrysts. While pyroxenes and plagioclase of population 1 dominantly lack disequilibrium textures, the outermost rims of plagioclase in this population are fine-sieved, containing channelized groundmass material. Augite in this population has elevated Al_2O_3 concentrations (3.5-4.1 wt. % Al_2O_3; similar to population 1 augite in *asw*). Presumably, these three populations of minerals (orthopyroxene, augite, and plagioclase) crystallized from a basaltic or high magnesium basaltic-andesitic magma relatively deep in the crust and represent the most mafic magmatic component of *ado*, the B1 crystallized assemblage (Table 12). This population of augite is the nearest in equilibrium with the bulk rock Mg# of *ado*-11 and -14 (Figure 34), similar to *asw*, and suggests that the bulk rock composition is probably very similar to the magma composition that crystallized the B1 assemblage, and can also be equated to a "host liquid" that incorporated other assemblages/populations. The lack of olivine in this most mafic assemblage supports a deep crustal, high pressure origin, where olivine is not on the liquidus at pressures higher than 1.2 GPa in basaltic and basaltic andesite magmas (Müntener et al. 2001).

Populations 2 of augite and plagioclase show the most extensive amount of disequilibrium, with both exhibiting patchy zonation and coarse sieves. This crystal assemblage has slightly more felsic core compositions (Mg# 82 and An_{54-59}) than population 1 of augite and plagioclase (Figure 13-14); however only augite has reversely zoned rims (Mg# 87), whereas patchy zones in plagioclase are more An-rich (An_{65-70})

than cores and rims. The patchy zonation in plagioclase is indicative of cores with a cumulate origin at high pH_2O and resorption textures acquired in H_2O-undersaturated conditions (Humphreys et al., 2006). The compositions of this assemblage suggest it crystallized from a slight more differentiated basaltic to basaltic-andesitic magma than the B1 assemblage; hence the designation as the BA1 crystallizing assemblage (BA1 assemblage; Table 12). This BA1 assemblage is identical to the BA1 assemblage in *asw* (Table 12*)*, and is interpreted to represent the same or similar magmatic component.

Populations 3 of augite and plagioclase represent a much more differentiated assemblage (Figure 13c and 14c) and show some level of disequilibrium (fine sieves and resorbed cores), however textures are far less exaggerated than population 2. The core chemistry of these populations of augite (Mg# 75) and plagioclase (An_{47-48}) suggests they crystallized from an andesitic magma, hence named the A1 assemblage (Table 12). Plagioclase displays minor patchy zoning with finely sieved outer zones, clearly indicative of mixing with a more mafic melt (Humphreys et al. 2006). Augite is unzoned and has resorbed cores (also indicative of mixing with a more mafic melt) and several inclusions of oxides and smaller pyroxenes.

Populations 4 (the most felsic) of plagioclase, augite and orthopyroxene are found coexisting in crystal clots and as individual phenocrysts. Similar to the most mafic crystallized assemblage, this assemblage also lacks disequilibrium textures. However, individual phenocrysts of augite do occasionally contain minor embayments and finely sieved cores. A reasonable explanation for this is that these isolated augites represent crystals that disaggregated early on, therefore having more time to react with the host melt and produce disequilibrium textures. Interestingly, orthopyroxene crystals in this

assemblage are relatively unzoned, whereas augites are *reversely* zoned (Mg# 73-80). The compositional zoning profile of population 4 augites suggests initial growth in a dacitic melt, named the D1 assemblage (Table 12) that eventually mixed with a mafic liquid to produce strong reverse zones (Streck et al., 2007). Immersion in a mafic magma could explain the similarity of rim compositions of augite population 4 with rim compositions of the minimally zoned B1 assemblage augite (rim Mg# 83). However, the lack of disequilibrium textures in plagioclase and orthopyroxene suggests minimal residing time in the host liquid.

The two populations of olivine identified in *ado* (only observed as isolated phenocrysts) are difficult to associate with the crystallizing assemblages mentioned above, as they are more fayalitic than what is expected to co-crystallize with the compositions of the pyroxene populations mentioned above. They are also never observed in crystal clots. Obata et al. (1974) and Brey and Kohler (1990) suggest that if olivine and pyroxene are in equilibrium, then the Mg# of olivine should be the same or slightly lower than that of augite and orthopyroxene. However, olivine in crystal clots of MBVF andesites are always more Mg-rich than coexisting pyroxenes (see *asw* and *adb*). The first population of olivine (Fo_{72-73}) contains embayments and resorbed cores, similar to population 3 of augite (Mg# 75), but is more similar in composition to augite population 4 (Mg# 70-73). The most felsic olivine population (Fo_{67-68}) is more Mg-poor than the most felsic assemblage of minerals, making it most likely unrelated. It is therefore likely that these fayalitic populations of olivine represent an additional, more evolved magmatic component or xenocryst, which lacks co-existing mineral phases.

In summary, mineral populations and their interpreted crystallizing assemblages indicate the involvement of at least four distinct magmatic components (Table 12) responsible for the petrogenesis of *ado*, with the two end member mineral assemblages (B1 and D1) as the most dominant components (source for crystal clots). Mg# of the B1 pyroxenes suggest crystallization from a basaltic or high magnesium basaltic-andesitic magma, similar to *asw* (Table 12). Thus, a mafic magma is the host liquid that crystallized the most mafic assemblage (B1), which includes the mafic crystal clots. Similar to *asw*, the high Al_2O_3 concentrations of augite in the B1 assemblage of *ado*, and the lack of co-crystallizing olivine, suggest an origin from a high pressure, deep crustal environment (Gasparik, 1984; Müntener et al. 2001). As this mafic magma ascended from the lower crust, it plucked cumulates (crystal clots), presumably from its own chamber. The felsic assemblage (D1), also found as crystal clots, most likely crystallized from a dacitic magma and spent the least amount of time residing in the host magma upon incorporation, due to the lack of reverse zoning and disequilibrium textures. The D1 assemblage, more abundant in *ado* than in *asw*, could have influenced the bulk rock chemical signature of *ado* enough to explain the bulk rock geochemical differences that exist between *asw* and *ado* (Figures 31-33). The other two intermediate assemblages (BA1 and A1 assemblages) clearly crystallized from distinct magmas and resided in the host magma for a longer period, evident from their extensive disequilibrium textures. A permissible interpretation would be that a basaltic or basaltic andesitic magma (presumably host magma) crystallized the B1 assemblage (both phenocrysts and crystal clots) and incorporated the other three assemblages as the host magma passed through liquid-poor crystal mushes (evident from most mafic assemblage nearest in equilibrium

with bulk rock Mg#) as described above. A possible fifth magmatic component may be responsible for the fayalitic olivine populations observed in *ado*, which does not appear to have crystallized with the aforementioned assemblages. Mixing with evolved liquids that crystallized the two fayalitic olivine populations cannot be ruled out, but there is no supporting textural evidence.

The andesite of Dobbs Cleaver

The andesite of Dobbs Cleaver (58.6-59.5 wt. % SiO_2, 3.5-4.0 wt. % MgO, 30-44 ppm Ni) is significantly more evolved than *asw* and *ado*, however, identified mineral populations are similar. As with the previously described units, the *adb* flow unit also yields a complex, and the largest, set of mineral populations. Similar to *asw* and *ado*, the mafic endmember mineral populations show less extensive disequilibrium textures than the other populations; however, those features are more pronounced in *adb* than in the mafic endmember populations of *asw* and *ado*. The mineral populations identified in *adb* include: four plagioclase populations (1:An_{60-61}, 2:An_{56-57}, 3:An_{46-54}, 4:An_{42-43}; Figure 18), four augite populations (1:Mg#81, 2:Mg#75-77, 3:Mg#75, 4:Mg#72-74; Figure 19), four orthopyroxene populations (1:Mg#77, 2:Mg#73-75, 3:Mg#71-73, 4:Mg#68-72; Figure 20) and four olivine populations (1:Fo_{88}, 2:Fo_{84-86}, 3:Fo_{76-80}, 4:Fo_{71}; Figure 21). As with the previous units, I describe co-crystallizing assemblages in the following paragraphs.

Populations 1 of augite and orthopyroxene are the most primitive and their high-Al concentrations (2.8-3.9 wt. % Al_2O_3) are indicative of a deep-crustal source (Gasparik, 1984). Augite and orthopyroxene both have coarse sieved cores and display weak normal

zoning. Unlike *asw* and *ado*, this population of augite is too Mg-rich to be in Mg# equilibrium with the bulk rock of *adb*-01 and -04 (Figure 34). Together, these populations of pyroxene represent the most mafic co-crystallized assemblage (B1 assemblage) of *adb* and were likely crystallized from a basaltic to high magnesium basaltic-andesitic magma (Table 12). The fact that augite of the *adb* B1 assemblage is too Mg-rich to be in equilibrium with the bulk rock Mg# of *adb*-01 and 04 suggests either that 1) a differentiated host liquid (similar to bulk rock composition) incorporated them during travel through the crust, or that 2) a mafic host liquid similar to *asw* and *ado* mixed with a more evolved liquid and its associated phenocrysts to produce a hybrid composition similar to the bulk rock composition, producing the disequilibrium features mentioned above. The latter hypothesis is supported by the mingling textures observed in this flow unit (described earlier in the petrography section, Figure 7c).

Olivine population 3 and populations 2 of augite, orthopyroxene and plagioclase represent the next most mafic co-crystallized assemblage (BA2 assemblage: phenocrysts and crystal clots, Table 12). There are three identified crystal clot types (types B, C and D; see Figure 22) that are made up of population 2 minerals. However, each crystal clot type has its own unique textures, sizes and mineral phases present. For example, population 1 of plagioclase (also included in this assemblage) is only observed in the megacrystic crystal clot type D and is slightly more calcic than plagioclase population 2, suggesting that the parental liquid of these crystal clots has undergone different stages of crystallization, and possibly magma turnover (Streck, 2008), to produce two populations of plagioclase. In spite of such differences, the chemistry of the crystal clots and phenocrysts from population 2 minerals are very similar and likely derived from a

singular magma with a complex evolutionary history. The compositions of the mineral phases in this crystallizing assemblage are representative of minerals expected to fractionate from a basaltic-andesitic to andesitic magma. In this crystallizing assemblage, augite and olivine are the nearest in equilibrium with the bulk rock Mg# of *adb*-01 and -04 (Figure 34). The lack of disequilibrium textures in population 2 augite and only minor embayments in olivine population 3 suggests that this crystallizing assemblage spent a short amount of time in the mafic host liquid or is representative of crystallization from the afore-mentioned hybridized liquid. The role of this magmatic component is discussed in the following section.

Population 3 of augite and orthopyroxene exhibit the most extensive amount of disequilibrium features (Figures 19 and 20), with augite reaction rims on orthopyroxene and exsolution and sieved cores in augite. The strong reverse zoning observed in this assemblage of pyroxenes (Mg# 79-85), with rim compositions resembling the mafic B1 assemblage (Mg# 76-82), is strong evidence that it came from a more evolved magma and then began to re-equilibrate upon contact with the more mafic host liquid. Core compositions of population 3 pyroxenes suggest it crystallized from an andesitic magma (Streck et al., 2005) with lower Mg# than the host rock, hence the name A1 assemblage (Table 12).

Populations 4 of augite and orthopyroxene, along with population 3 of plagioclase, make up the most evolved crystallized assemblage (Table 12). This assemblage also forms crystal clots (type A; Figure 22) that are identical to the D1 assemblage of phenocrysts and crystal clots identified in *asw* and *ado*. Disequilibrium features are characteristic of this assemblage (e.g. minor embayments, reverse zoning), however, they

are far less exaggerated than in the intermediate assemblage. The mineral compositions within this assemblage, as in *ado*, suggest that the assemblage crystallized from a dacitic magma, hence named the D1 assemblage (Table 12) and were incorporated into a more mafic magma to produce reversely zoned rims.

The origins of olivine populations 1, 2 and 4 are unconstrained. Population 1 of olivine is the most primitive olivine analyzed in this study, with chemistry that is too forsteritic (core Fo_{88}) to be in equilibrium with the bulk rock Mg# of *adb*-01 and -04 (Figure 34), but is close to that expected from equilibrium with mantle peridotite (Figure 35). This population of olivine is found only as very euhedral glomerocrysts with abundant chromite inclusions. It is likely that olivine population 1 is ultimately derived from a very primitive magma (much more mafic than the bulk rock composition). Due to its small size and low abundance (≤1%) in the sample, incorporation of this olivine likely had a minimal effect on the Mg, Ni and Cr content of the bulk rock. Fo content of olivine population 2 (Fo_{84-86}) suggests it may have co-crystallized with populations 1 of augite and orthopyroxene (B1 assemblage), however, olivine is not found in crystal clots. In addition, pyroxenes of the B1 assemblage have high-Al concentrations, indicative of high pressure and deep crustal origin, where olivine is not on the liquidus (Müntener et al., 2001). The high-Ni content (Figure 35) and abundance of chromite inclusions in olivine population 2 imply they are early-fractionated olivine from a mafic liquid. Olivine population 2 generally occurs as glomerocrysts, lacks disequilibrium textures and is also too forsteritic to be in equilibrium with the bulk rock Mg# of *adb*-01 and -04 (Figure 34). Olivine population 4 is the same unconstrained olivine population as in *ado*. This population of olivine is too fayalitic (Fo_{71}) to have crystallized with any of the

aforementioned assemblages. The origin of plagioclase population 4, the most sodic, is also unconstrained, as it likely did not crystallize with the most felsic assemblage. One permissible explanation is that these two populations represent other, more evolved, magmatic components lacking other mineral phases. Both lack disequilibrium textures, which indicate they were likely incorporated into the host magma shortly before eruption.

In summary, four distinct crystallizing assemblages comprise *adb* (Table 12). Interestingly, *adb* contains the most primitive olivine of all the flow units in the study, yet bulk rock chemistry shows this flow unit to be more evolved than *asw* and *ado* (Figures 28-33). Because this primitive olivine is small and rare (≤1%), it likely had minimal influence on the overall magma composition. Similar to *ado*, there are at least two crystallizing assemblages responsible for the significant amount of phenocryst and crystal clot input (Table 12). However, in the case of *adb*, the main crystal clot input is from a basaltic-andesitic to andesitic magma (BA2 assemblage; Table 12), rather than a basaltic or *high magnesium* basaltic andesitic magma as in *asw* and *ado*. The BA2 assemblage is closer to equilibrium with bulk rock Mg# of *adb*-01 and -04 (Figure 34), whereas in *asw* and *ado* the B1 assemblage is the nearest in Mg# equilibrium with its bulk rock. Mixing between a basaltic to high magnesium basaltic andesitic magma (parental to B1 assemblage) with a basaltic-andesitic to andesitic magma (parental to the phenocrysts and crystal clots of the BA2 assemblage), could explain why the bulk rock composition of *adb* is more silicic than *asw* and *ado*, and why the B1 assemblage is more out of equilibrium than observed in *asw* and *ado*. This is further discussed in the following section.

A permissible mixing scenario for *adb* is that a basaltic or high magnesium basaltic-andesitic magma, crystallizing the B1 assemblage, ascended from deep in the crust, as evidenced by high Al_2O_3 concentrations in augite (Gasparik, 1984). The other entrained crystallized assemblages (BA2, A1 and D1) could have been sourced from contamination as the magma passed through crystal mushes, magma mixing with more evolved liquids, or both. Unlike *asw* and *ado*, magma mingling textures in *adb* supports liquid mixing (Figure 7c) rather than just crystal mush entrainment. If the magmatic source for D1 supplied a significant amount of liquid, then the BA2 assemblage minerals could represent equilibrium crystallization from the hybridized liquid. Another permissible interpretation is that the BA2 assemblage is an additional cumulate mush entrained in the host magma, which is supported by the presence of BA2 crystal clots. The potential source for the additional liquid component is discussed later.

The andesite of Coleman Pinnacle

The *acp* flow unit (57.7-64.8 wt. % SiO_2, 1.5-3.2 wt. % MgO, 3-24 ppm Ni) yielded the least variable set of mineral populations. As observed in the other flow units, the most mafic assemblages display the least amount of disequilibrium while the more evolved assemblages have more extensive disequilibrium features. Mineral populations identified in andesitic samples of *acp* include: three plagioclase populations (1:An_{52-60}, 2:An_{46}, 3:An_{42-45}; Figure 23), one hornblende population (Mg#71-77; Figure 24), one orthopyroxene population (Mg#64-68; Figure 24) and three augite populations (1:Mg#76-82, 2:Mg#75, 3:Mg#69-72; Figure 25).

Populations 1 of plagioclase and augite, the most mafic, coexist in crystal clots and also exist as individual phenocrysts. Higher concentrations of Al_2O_3 in augite population 1(3.0-4.4 wt.%) are indicative of it being derived from a deep crustal source (Gasparik, 1984). Its moderate to high Mg# (76-82) is similar to the augites observed in the other flow units ascribed to a basaltic to basaltic andesite magmatic component (BA) parent (Table 12). However, they are distinctly higher in Wo component and define a salitic trend typical of clinopyroxene that crystallizes from alkaline magmas (Figure 6 and Table 3). This distinct pyroxene composition suggests that the parental magma for this is distinct from that supplying the BA1 and BA2 augites of *asw*, *ado* and *adb*, hence it is named the BA3 assemblage (Table 12). This population of augite is the nearest in Mg# equilibrium with the bulk rock of *acp*-20 (Figure 34). Hornblende, with Mg# compatible for co-crystallization with the BA3 assemblage, is only found as isolated crystals and microlites. The absence of hornblende in BA3 crystal clots suggests two hypotheses: 1) hornblende *did not* crystallize with the BA3 assemblage and is derived from a distinct magmatic component, or 2) hornblende *did* crystallize as part of the BA3 assemblage is not found in BA3 crystal clots of the analyzed thin section. The latter is more probable, due to only one thin section of *acp* analyzed with minimal analyses; therefore, it is likely that hornblende incidentally was not observed/analyzed in crystal clots selected for microprobe analyses.

The second population of augite (Mg# 75) is rare and cannot be associated with other mineral populations. This population has minimal disequilibrium features, suggesting stability in the host magma, however it contains an abundance of inclusions of oxides,

apatite and plagioclase along with scattered fine sieves. Its core Mg# 75 suggests it crystallized from an andesitic magma (A2 assemblage, Table 12).

Population 3 of augite shows the most extensive amount of disequilibrium (coarse sieves) and coexists in crystal clots with plagioclase population 2, which also has extensive disequilibrium features (blebby coarse sieves). The compositions of this assemblage suggest it crystallized from a dacitic magma, identical to the liquid producing the D1 assemblage crystal clots in *ado* and *adb* (Table 12).

A third population of plagioclase is texturally distinguished from the rest with its patchy zonation and well-rounded crystal edges though it is similar in composition to population 2 of plagioclase.

Orthopyroxene, though only one population, is perplexing. It is found in both the mafic and felsic crystal clots and has a narrow compositional range of Mg# 64-68 (Table 12). One possible explanation is that the "core" analysis in the basaltic-andesitic clot was actually representative of a mid-section or rim, suggesting normal zoning. Alternatively, this could be one example where crystals in the clots *were* randomly aggregated. Oddly, isolated phenocrysts of orthopyroxene exhibit reactions rims of augite (Figure 24c), but orthopyroxene with the same core compositions in crystal clots does not. This may be a result of isolated phenocrysts having more opportunity to react with host liquid than those crystals in the clots.

In summary, there are a minimum of three magma types (basaltic andesite, andesite and dacite) supplying phenocrysts and crystal clots to the *acp* flow unit (Table 12). Similar to the medium-K andesites, the most mafic augites (BA3 assemblage; Table 12) are the nearest in equilibrium with the bulk rock Mg# of *acp*-20 (Figure 34), suggesting

that the bulk rock composition of *acp*-20 can be equated to a host liquid that has differentiated enough to become andesitic in composition, rather than basaltic andesitic like the BA3 assemblage. Another permissible interpretation is that the magmatic source of the D1 assemblage (Table 12) represents a more liquid-rich crystal mush that supplied enough liquid to result in an increase in the bulk rock silica composition of *acp*-20 upon mixing, similar to the *adb* flow unit. However, no textural evidence (e.g., magma mingling) exists to support this.

Plagioclase population 3, unconstrained, could potentially represent an additional magmatic component that supplied enough liquid to increase the silica content of *acp*. A permissible scenario for *acp* is that a basaltic andesitic magma that crystallized the BA3 assemblage (Table 12), along with hornblende, ascended from the lower crust and incorporated crystal mush material ± liquid (D1 assemblage) before eruption. The intermediate A2 assemblage (Table 12) represents an additional magmatic component that was likely incorporated shortly before eruption providing no time to produce disequilibrium textures. Similar to *asw* and *ado*, liquid mixing cannot be ruled out, however no textural evidence supports this.

Potential parental magmas of MBVF medium-K andesites

Three previously identified mafic magmas of MBVF serve as strong candidates for parental magmas of the medium-K andesites in this study: HMBA of Tarn Plateau, HMBA of Cathedral Crag and HMA of Glacier Creek. Moore and DeBari (2012), Baggerman and DeBari (2011) and Sas (2015) have characterized these three mafic magmas and make strong cases for them as primary melts. Utilizing the authors'

extensive mineral dataset, I compare core compositions of the most primitive augites and olivines in the primary magmas mentioned above to the core compositions of the most mafic augite and olivine populations in the medium-K andesites of this study to determine which is the most likely parental magma.

Augites of the B1 crystal assemblage are very primitive (Mg# 81-85) and only the HMBA of Tarn Plateau (augite Mg# 78-89) and Cathedral Crag (augite Mg# 74-88) contain such Mg-rich augites (Moore and DeBari, 2012; Sas, 2015). Other basaltic flow units (Lake Shannon and Park Butte) did not crystallize such primitive augites (see Moore and DeBari, 2012).

The most primitive olivines in the medium-K andesites have a compositional range of Fo_{84-88} and only the HMBA of Tarn Plateau (olivine Fo_{77-85}) and HMA of Glacier Creek (olivine Fo_{72-86}) contain such forsteritic olivines (Moore and DeBari, 2012; Sas, 2015; Baggerman and DeBari, 2011). Such primitive olivines are not present in the basaltic flow units (see Baggerman and DeBari 2011 and Moore and DeBari, 2012).

As a result, the HMBA of Tarn Plateau is a strong candidate for parent liquid to the medium-K andesites of this study. The B1 crystal assemblage (observed in all medium-K andesites; Table 12) contains augite and olivine core compositions only observed coexisting in the HMBA of Tarn Plateau (Moore and DeBari, 2012 and Sas, 2015). The HMA of Cathedral Crag and Glacier Creek are too Si-rich, and primitive olivine and augite do not coexist, making them unlikely parental magmas. As further evidence, the HMBA of Tarn Plateau has REE patterns that are similar to the medium-K andesites (Figure 33). The medium-K andesites of this study are not Mg-rich enough to be classified as HMA, however, they are more Mg-rich than other MBVF andesites of the

same silica range (Figures 30-31). For this reason, the medium-K andesites of this study most likely represent derivative magmas from a parent similar to the Tarn Plateau HMBA after both pyroxene fractionation and incorporation of crystal mushes.

Petrogenesis of intermediate magmas at MBVF: complex mixing

Andesites are commonly thought of as products of fractional crystallization of a parental melt or as hybrid products resulting from the mixing of basaltic and silicic liquids. In the Cascade arc, several studies have suggested that andesites and dacites result from fractional crystallization of a parental melt (e.g., Mount Hood: Wise, 1969; Mount Adams: Sisson et al., 2014; Mount Baker: Gross, 2012) or the mixing of two end member magmas (e.g. Mount Hood: Kent et al., 2010; Mount Rainier: Venezky and Rutherford, 1997; Mount Baker: Gross, 2012).

In this study, the complex array of mineral compositions, zoning profiles and disequilibrium textures provide strong evidence that the andesites of MBVF are indeed products of open system processes involving multiple magmas. However, such an abundance of mineral and crystal clot populations cannot be explained strictly through two-component magma mixing and/or fractional crystallization. Furthermore, magma mixing, in the case of MBVF andesites, does not necessarily involve substantial amounts of liquid mixing but rather the entrainment of multiple batches of crystal mush (Figure 36). This is clear evidence that open-system processes generating the intermediate magmas are far more intricate than simple mixing. In the following sections I rely heavily on proposed crystallized assemblages in Table 12 to elaborate on the open-system

processes responsible for the generation of each andesitic flow unit, presented in chronological order (Figure 36).

High-K andesite: The andesite of Coleman Pinnacle

The petrogenetic origin of the andesite of Coleman Pinnacle and its associated BA3 assemblage is not resolved in this study, as there is no known mafic counterpart anywhere in the MBVF. The chemistry of *acp* suggests a distinct sub-Moho source from that of the medium-K andesites, and it carries no basaltic or high magnesium basaltic andesitic mineral assemblages (Table 12). Despite this difference, the D1 crystal assemblage, the most differentiated, is present in both *acp* and the medium-K andesites (Table 12). This means that magmas ascending from the lower crust at MBVF are likely tapping the same or similar types of cumulates over long periods of time (300 ka to 45 ka), regardless of the origin of the parental magma (Figure 36).

The BA3 crystallizing assemblage (Table 12) is unique to *acp* and is closest to equilibrium with the bulk rock Mg# of *acp*-20 (Figure 34a). The Mg# range of the augite in the *acp* BA3 assemblage is similar to basaltic-andesitic augite in the medium-K andesites; however, *acp* mafic augites are significantly more Ca-rich (see salitic trend; Figure 6), which suggests that they are derived from a distinct parental melt. Because the BA3 crystallizing assemblage is the only one unique to Coleman Pinnacle, it must be the source for hornblende (which only exists at Coleman Pinnacle). Hornblende is not observed in the crystal clots that are unique to the BA3 assemblage; however, hornblende does exist as groundmass microlites, suggesting that it continuously crystallized from the host liquid composition while it incorporated D1 cumulate material.

As seen in Figure 28, the *acp* flow unit grades compositionally into dacite. These are also hornblende bearing and the first order interpretation would be that they represent the end products of a crystal fractionation trend. However, their REE compositions preclude this possibility (Figure 33). Andesitic samples of *acp* are more enriched in LREE and have steeper REE patterns than the dacitic samples (Figure 33). Crystal fractionation, especially of hornblende, would produce the opposite REE trend. The contrasting bulk rock geochemical signature between the andesites (steep REE) and dacites (flat REE) of *acp* (Figure 33) is evidence that the flow unit itself represents mixing between two distinct magmas (Figure 36a).

The dacites of *acp* share identical chemical compositions and mineralogy with the 149 ± 5 ka dacite of Nooksack Falls (Gross, 2012). Gross (2012) concluded the dacite of Nooksack Falls is a near endmember magma with minimal evidence for contamination/mixing. Considering her conclusion, it is likely that dacites of *acp* represent the felsic endmember magmatic component that mixed with a basaltic andesitic liquid (BA3 assemblage) to produce a hybridized andesitic liquid (Figure 36a).

Medium-K andesites: The andesite of Swift Creek, Dobbs Creek and Dobbs Cleaver

Mineral compositional and textural data of the medium-K andesites provide evidence that the most mafic co-crystallized assemblage in each flow unit (B1 in Table 12) is *generally* the nearest in Mg# equilibrium with the bulk rock (with the exception of *adb*). Across all medium-K flow units, the minerals in the B1 assemblages are euhedral to subhedral in shape, span similar compositional ranges, are small in size and low in abundance. This serves as strong evidence that a common, nearly aphyric (crystal poor)

fractionated magma, with its B1 crystallizing assemblage, has mixed with more differentiated magmatic liquids/cumulates to produce the medium-K andesites (Figure 36b-d). This magma, fractionating the B1 assemblage, is interpreted to be the high magnesium basaltic-andesite of Tarn Plateau (Figure 36b-d). The differentiated magmatic components (B2, BA1, BA2, A1 and D1 co-crystallizing assemblages; Table 12) supplied various types of crystals plus or minus liquid, resulting in multiple populations of minerals in a single flow unit. Two of the differentiated co-crystallized assemblages are observed in all medium-K andesites (A1 and D1; Table 12 and Figure 36b-d), suggesting that upon ascension, the magma crystallizing the B1 assemblage is "tapping" the same, or similar, cumulates (Figure 36b-d).

In the case of *ado* and *asw*, these *other*, more differentiated, magmatic components are most likely liquid-poor crystal mushes (cumulates) residing in the mid- to lower crust (Figure 36b and d). Evidence for their being liquid-poor is the fact that the B1 assemblage has the least evidence for textural disequilibrium, and is the nearest in Mg# equilibrium with the bulk rock in each case (Figure 34). This near equilibrium suggests that the Mg# of the host liquid changed minimally after incorporating these other magmatic components. If the source of the additional magmatic component had included significant liquid with the observed crystals, that near equilibrium would not be possible. This argument is supported by disequilibrium features observed in *adb*, which likely did incorporate significantly more liquid with the crystals (see below).

A reasonable explanation for the greater extent of disequilibrium textures in the more evolved assemblages (BA1, A1and D1) is that these crystal mushes included minimal liquid, and upon coming into contact with a more mafic liquid, developed

disequilibrium features, while the B1 assemblage was minimally affected because its host liquid Mg# did not change by incorporation of the crystal mush.

Mineral textures observed in the more differentiated crystallized assemblages (B2, BA1 and D1) are evidence for these cumulates residing in the lower crust. Patchy zonation, specifically in plagioclase, is indicative of high-pressure crystallization during cumulate formation and resorption during decompression (Humphreys et al., 2006) and exsolution of augite and undulatory extinction is also indicative of slow cooling and plutonic origin. In addition, the B2, BA1 and D1 assemblages *generally* exhibit the most extensive disequilibrium features, suggesting they were incorporated by the ascending host magma early on (Figure 36b-d). The A1 and BA2 assemblages, on the other hand, generally show the least amount of disequilibrium, suggesting they reside at shallower depths and were entrained after the B2, BA1 and D1 assemblages (Figure 36b-d).

In the case of *adb*, the augite and olivine of the B1 crystallizing assemblage are too Mg-rich to be in equilibrium with the bulk rock Mg# (Figure 34). Disequilibrium textures (e.g. coarsely-sieved cores) of the pyroxenes in the B1 assemblage (Figure 19a) in *adb* are further evidence that they are out of equilibrium with the bulk rock composition. A permissible explanation is that some mixing of the mafic host liquid with a more differentiated liquid and its mineral cargo occurred, resulting in the development of disequilibrium features of the B1 augites and orthopyroxenes (Figure 19a and 20a). Microscopic mingling features observed in *adb* (Figure 7c) supports this interpretation. The more differentiated liquid is likely the host to the BA2 crystallizing assemblage, which is unique to *adb*. The megacrysts that comprise this assemblage have compositional ranges unseen in *asw* and *ado*, especially for olivine. A permissible

hypothesis for *adb* being a more evolved flow unit on average than *asw* and *ado* (Figures 28-33), but with strikingly similar crystal assemblages (Table 12), is that the same mafic host liquid (high magnesium basaltic andesite of Tarn Plateau) from *asw* and *ado* incorporated a more liquid-rich BA2 assemblage (Figure 36c). A substantial amount of liquid must have been available to influence the bulk rock geochemical signature and cause the B1 crystallizing assemblage to develop disequilibrium features.

Mineral populations in *ado* and *adb* with unconstrained origin (Table 12) could represent additional magmatic components (liquid and/or cumulates). In the case of *adb*, the unconstrained population of olivine (Fo_{71}) and plagioclase (An_{42-43}) could potentially have included an additional differentiated liquid component affecting the overall bulk rock composition.

In summary, a common mafic magma (such as the high magnesium basaltic andesite of Tarn Plateau) crystallized the B1 assemblage, and tapped an array of cumulates (mostly liquid-poor) on the path to the surface since the mid-Pleistocene (Figure 36). These cumulates are likely the source for the various populations of phenocrysts and crystal clots in the erupted flow units, and upon their entrainment in the host liquid, they developed disequilibrium features. An additional component in *adb*, responsible for the megacrystic BA2 assemblage, likely provides a more substantial amount of liquid, resulting in microscopic mingling features, disequilibrium features in the B1 assemblage, and a more evolved bulk rock composition.

Conclusions

Mineral compositions and textures of MBVF intermediate magmas reveal that the generation of MBVF andesites involves a variety of open system processes, much too complex to be explained with whole rock analyses and modeling alone. The presence of multiple mineral and crystal clot populations in a single flow unit suggests that intermediate magmas at MBVF are not generated strictly through mixing of two compositionally distinct magmas, but rather through a series of multiple mixing events involving cumulate material. The medium-K andesites of MBVF (*asw*, *ado* and *adb*) show a common parental magma (B1) supplies a primitive assemblage of minerals expected to crystallize from a basaltic or high magnesium basaltic magma. This primitive assemblage, B1 assemblage, is generally the nearest in equilibrium with the bulk rock Mg#, suggesting that the other, more differentiated, entrained assemblages are from liquid-poor crystal mushes, having minimal effect on the whole rock geochemical signature. In the case of the high-K *acp*, the most mafic assemblage (BA3), hornblende bearing, contains compositionally distinct augites that suggest a distinct sub-Moho parental component.

The *asw* and *ado* flow units both have at least four distinct magmatic components, each with their own unique supply of mineral cargo. The B1 assemblage appears as crystal clots in both *asw* and *ado*, with *ado* also including crystal clots from the D1 assemblage. The minor differences in whole rock chemistry between *asw* and *ado* are likely due to the B2 assemblage unique to *asw* and the D1 crystal clots only present in *ado*. In spite of these differences, a similar parental magma, with the B1 assemblage, is mixing with liquid-poor crystal mushes on its way to the surface and tapping a series of

cumulates that are responsible for the variety of mineral cargo observed in *asw* and *ado*. The *adb* flow unit, significantly more silica-rich, is understood to have undergone substantial liquid mixing, as evidenced by microscopic mingling textures, either from its unique BA2 magmatic source or from one of the other more differentiated assemblages. Similarly though, the B1 assemblage is also present in *adb*, which serves as evidence that it shares a similar parental magma to *asw* and *ado*. The chemistry of the B1 assemblage minerals of the medium-K andesites is only found in the parental HMBA of Tarn Plateau. This serves as good evidence that the most mafic magmatic component in the medium-K andesites of MBVF (B1 assemblage) can be interpreted to be differentiates of HMBA of Tarn Plateau.

The origin of the higk-K *acp* flow unit remains cryptic. However, whole rock and mineral chemistry shows that a distinct parental magma is likely the source for hornblende. In addition, dacitic samples of *acp* are identical to the dacite of Nooksack Falls, suggesting that the andesites of *acp* represent a hybridized liquid between dacitic and basaltic-andesitic end member magmas. Despite this, differentiated crystallized assemblages found in the medium-K andesites are also found in *acp*, supporting the interpretation that all ascending magmas of MBVF interact with similar cumulate material.

This study goes to show that mineral studies, in combination with whole rock analyses, provide an invaluable amount of detail of magmatic processes and allow for more involved interpretations of andesite petrogenesis than whole rock analyses alone. Although previous studies of MBVF lavas have shed light on the complex magmatic processes responsible for andesite generation (e.g., Baggerman and DeBari, 2011 and

Gross, 2012) their heavy reliance on whole rock data led to oversimplified mixing models. Minerals prove to be much more rich and intricate recorders of magmatic processes, allowing for more involved interpretations of andesite petrogenesis. Interestingly, several crystallized assemblages are found in any given andesite of MBVF, suggesting that erupting magmas, regardless of age, are tapping the same or similar cumulates on their way to the surface, which are the source for the notorious crystal clots of MBVF.

References

Amma-Miyasaka, M., and Nakagawa, M., 2003, Evolution of deeper basaltic and shallower andesitic magmas during the AD 1469-1983 eruptions of Miyake-Jima volcano, Izu-Mariana arc: Inferences from temporal variations of mineral compositions in crystal-clots: Journal of Petrology, v. 44, p. 2113-2138.

Andersen, D.J., and Lindsley, D.H., 1985, New (and final!) models for the Ti-magnetite/ilmenite geothermometer and oxygen barometer: Abstract for the AGU 1985 spring meeting, Eos Transactions, American Geophysical Union, 66 (18), 416.

Andersen, D.J., and Lindsley, D.H., 1988, Internally consistent solution models for Fe-Mg-Mn-Ti oxides: Fe-Ti oxides: The American Mineralogist, v. 73, p. 714-726.

Andersen, D.J., Lindsley, D.H., and Davidson, P.M., 1993, QUILF: A Pascal program to assess equilibria among Fe-Mg-Mn-Ti oxides, pyroxenes, olivine, and quartz: Computers & Geosciences, v. 19, p. 1333-1350.

Annen, C., Blundy, J.D., and Sparks, S.J., 2006, The genesis of intermediate and silicic magmas in deep crustal hot zones: Journal of Petrology, v. 47, p. 505-539

Arculus, R.J., and Wills, K.J.A., 1980, The petrology of plutonic blocks and inclusions from the Lesser Antilles island arc: Journal of Petrology, v. 21, p. 743-799.

Bacon, C.R., and Hirschmann, M.M., 1988, Mg/Mn partitioning as a test for equilibrium between coexisting Fe-Ti oxides: American Mineralogist, v. 73, p. 57-61.

Baggerman, T.D., and DeBari, S.M., 2011, The generation of a diverse suite of Late Pleistocene and Holocene basalt through dacite lavas from the northern Cascade arc at Mount Baker, Washington: Contributions to Mineralogy and Petrology, v. 161, p. 75–99.

Borg, L.E., and Clynne, M.A., 1998, The petrogenesis of felsic calc-alkaline magmas from the southernmost Cascades, California: origin by partial melting of basaltic lower crust: Journal of Petrology, v. 39, p. 1197–1222.

Bostock, M.G., and VanDecar, J.C., 1994, Upper mantle structure of the northern Cascadia subduction zone: Canadian journal of Earth Science, v. 32, p. 1-12.

Brey, G.P., and Kohler, T., 1990, Geothermobarometry in four-phase lherzolites II. New thermobarometers, and practical assessment of existing thermobarometers: Journal of Petrology, v. 31, p. 1353-1378.

Brown, E.H., Bernardi, M.L., Christenson, B.W., Cruver, J.R., Haugerud, R.A., Rady, P.M., and Sondergaard, J.N., 1981, Metamorphic facies and tectonics in part of the Cascade Range and Puget Lowland of northwestern Washington: Geological Society of America Bulletin, v. 92, p. 170-178.

Brown, E.H., 1987, Structural geology and accretionary history of the Northwest Cascades system, Washington and British Columbia: Geological Society of America Bulletin, v. 99, p.201-214.

Brown, E.H., Talbot, J.L., McClelland, W.C., Feltman, J.A., Lapen, T.J., Bennett, J.D., 2000, Interplay of plutonism and regional deformation in an obliquely convergent arc, southern coast belt, British Columbia: Tectonics, v. 19, p. 493-511.

Christensen, M.I., and Mooney, W.D., 1995, Seismic velocity structure and composition of the continental crust: a global view: Journal of Geophysical Research, v. 100, p. 9761-9788.

Clynne, M.A., and Borg, L.E., 1997, Olivine and chromian spinel in primitive calc-alkaline and tholeiitic lavas from the southernmost Cascade range, California: a reflection of relative fertility of the source: The Canadian Mineralogist, v. 35, p. 453-472.

Clynne, M.A., 1999, A complex magma mixing origin for rocks erupted in 1915, Lassen Peak, California: Journal of Petrology, v. 40, p. 105-132.

Conrad, W.K., Kay, S.M., and Kay, R.W., 1983, Magma mixing in the Aleutian arc: Evidence from cognate inclusions and composite xenoliths: Journal of Volcanology and Geothermal Research, v. 18, p. 279-295.

Conrad, W.K., and Kay, R.W., 1984, Ultramafic and mafic inclusions from Adak island: crystallization history, and implications for the nature of primary magmas and crustal evolution in the Aleutian arc: Journal of Petrology, v. 25, p. 88-125.

Danner, W.R., 1966, Limestone resources of western Washington: Washington Division of Mines and Geology Bulletin, v. 52, p. 474.

Dash, R.K., Spence, G.D., Riedel, M., Hyndman, R.D., and Brocher, T.M., 2007, Upper-crustal structure beneath the Strait of Georgia, Southwest British Columbia: Geophysics Journal International, v. 170, p. 800-812.

Flood, R.H., Vernon, R.H., Shaw, S.E., and Chappell, B.W., 1977, Origin of pyroxene-plagioclase aggregates in a rhyodacite: Contributions to Mineralogy and Petrology, vol. 60, p. 299-309.

Garcia, B.J., 2008, Magma mixing at Mt. Baker, Washington: evidence from solution textures in plagioclase: University of Alabama.

Garcia, M.O., and Jacobson, S.S., 1979, Crystal clots, amphibole fractionation and the evolution of calc-alkaline magmas: Contributions to Mineralogy and Petrology, v. 69, p. 319-327.

Gasparik, T., 1984, Two-pyroxene thermobarometry with new experimental data in the system CaO-MgO-Al_2O_3-SiO_2: Contributions to Mineralogy and Petrology, v. 87, p. 87-97.

GeoPRISMS, 2010, Draft Science Plan, http://www.geoprisms.org/wp-content/uploads/2014/09/GeoPRISMS_DSP_full_hires.pdf

Gill, J.B., 1981, Orogenic andesites and plate tectonics: Springer-Verlag Berlin New York.

Ginibre, C., Wörner, G., and Kronz, A., 2007, Crystal zoning as an archive for magma evolution: Elements, v. 3, p. 261-266.

Green, N.L., 1988, Basalt-basaltic andesite mixing at Mount Baker volcano, Washington, I. Estimation of mixing conditions: Journal of volcanology and geothermal research, v. 34, p. 251–265.

Green, N.L., and Harry, D.L., 1999, On the relationship between subducted slab age and arc basalt petrogenesis, Cascadia subduction system, North America: Earth and Planetary Science Letters, v. 171, p. 367-381.

Greene, A.R., DeBari, S.M., Kelemen, P., Blusztajn, J., and Clift, P.D., 2006, A detailed geochemical study of island arc crust: the Talkeetna arc section, south-central Alaska: Journal of Petrology, v. 47, p. 1051-1093.

Gross, J.A., 2012, Felsic magmas from Mt. Baker in the northern Cascade arc: origin and role in andesite production: Western Washington University.

Grove, T.L., and Kinzler, R.J., 1986, Petrogenesis of andesites: Annual Reviews Earth Planetary Science, v. 14, p. 417-454.

Guffanti, M., and Weaver, C.S., 1988, Distribution of late Cenozoic volcanic vents in the Cascade Range: Volcanic arc segmentation and regional tectonic considerations: Journal of Geophysical Research: Solid Earth (1978–2012), v. 93, p. 6513–6529.

Heaton, T.H., and Kanamori, H., 1984, Seismic potential associated with subduction in the northwestern United States: Bulletin of the Seismological Society of America, v. 74, p. 933–941.

Hildreth, W., and Moorbath, S., 1988, Crustal contribution to arc magmatism in the Andes of Central Chile: Contributions to Mineralogy and Petrology, vol. 98, p. 455-489.

Hildreth, W., 2007, US Geological Survey professional paper: Quaternary magmatism in the Cascades - geologic perspectives: US Government Printing Office.

Hildreth, W., Fierstein, J., and Lanphere, M., 2003, Eruptive history and geochronology of the Mount Baker volcanic field, Washington: Geological Society of America Bulletin, v. 115, p. 729–764.

Humphreys, M.C.S., Blundy, J.D., and Sparks, R.S.J., 2006, Magma evolution and open-system processes at Shiveluch volcano: insights from phenocryst zoning: Journal of Petrology, v. 47, p. 2303-2334.

Irvine, T.N., and Baragar, W.R.A., 1971, A guide to the chemical classification of the common volcanic rocks: Canadian Journal of Earth Sciences, v. 8, p. 523–548.

Jerram, D.A., Cheadle, M.J., and Philpotts, A.R., 2003, Quantifying the building blocks of igneous rocks: Are clustered crystal frameworks the foundation?: Journal of Petrology, v. 44, p. 2033-2051.

Johnson, D.M., Hooper, P.R., and Conrey, R.M., 1999, XRF analysis of rocks and minerals for major and trace elements on a single low dilusion Li-tetraborate fused bead: JCPDS International Centre for Diffraction Data

Journeay, J.M., and Friedman, R.M., 1993, The Coast Belt thrust system: evidence of late Cretaceous shortening in southwest British Columbia: Tectonics, v. 12, p. 756-775.

Kent, A.J.R., Darr, C., Koleszar, A.M., Salisbury, M.J., and Cooper, K.M., 2010, Preferential eruption of andesitic magmas through recharge filtering: Nature Geoscience, v. 3, p. 631-636.

Le Maitre, R.W., Bateman, P., Dudek, A., Keller, J., Lameyre Le Bas, M.J., Sabine, P.A., Schmid, R., Sorensen, H., Streckeisen, A., Woolley, A.R., and Zanettin, B., 1989, A classification of igneous rocks and glossary of terms: Blackwell, Oxford.

Leake, B.E., 1978, Nomenclature of amphiboles: The Canadian Mineralogist, v. 16, p. 501-520.

Lepage, L.D., 2003, ILMAT: an Excel worksheet for ilmenite–magnetite geothermometry and geobarometry: Computers & Geosciences, v. 29, p. 673–678.

Misch, P., 1966, Tectonic evolution of the northern Cascades, Washington: Tectonophysics, v. 342, p. 351-370.

McCrory, P.A., Blair, J.L., Oppenheimer, D.H., and Walter, S.R., 2004, Depth to the Juan de Fuca slab beneath the Cascadia subduction margin: a 3-D model for sorting earthquakes [CD-ROM], U.S. Geological Survey Data Series, DS-91.

McDonough, W.F., and Frey, F.A., 1989, REE in upper mantle rocks. In: Geochemistry and mineralogy of rare Earth elements. Lipin, B., and McKay, G.R., (Editors), Mineralogical Society of America, Chelsea, Michigan. 99-145.

Monger, J.W.H., and Journeay, J.M., 1994, Guide to the geology and tectonic evolution of the southern Coast Mountains: Geological Survey of Canada, Open File 2490, 77 p.

Monger, J.W.H., and Nokleberg, W.J., 1996, Evolution of the northern North America Cordillera: generation, fragmentation, displacement and accretion of successive North American plate-margin arcs, in Coyner, A.R., and Fahey, P.L., ed., Geology and ore deposits of the American Cordillera: Geological Society of Nevada Symposium Proceedings, Reno/Sparks, Nevada, 1133-1152.

Monger, J.W.H., and Price, R.A., 2000, A transect of the southern Canadian Cordillera from Vancouver to Calgary: Geological Survey of Canada Open File 3902, 170 p.

Moore, N.E., and DeBari, S.M., 2012, Mafic magmas from Mount Baker in the northern Cascade arc, Washington: probes into mantle and crustal processes: Contributions to Mineralogy and Petrology, v. 163, p. 521–546.

Mullen, E.K., and McCallum, I.S., 2013, Coexisting pseudobrookite, ilmenite, and titanomagnetite in hornblende andesite of the Coleman Pinnacle flow, Mount Baker, Washington: Evidence for a highly oxidized arc magma: American Mineralogist, v. 98, p. 417–425.

Mullen, E.K., 2011, Petrology and geochemistry of the Mount Baker volcanic field: constraints on source regions and terrane boundaries, and comparison with other Cascade Arc volcanic centers: University of Washington

Müntener, O., Kelemen, P.B., and Grove, T.L., 2001, The role of H_2O during crystallization of primitive arc magmas under uppermost mantle conditions and genesis of igneous pyroxenites: an experimental study: Contributions to Mineralogy and Petrology, v. 141, p. 643-658.

Nakagawa, M., Wada, K., and Wood, C.P., 2002, Mixed magmas, mush chambers and eruption triggers: evidence from zoned clinopyroxene phenocrysts in andesitic scoria from the 1995 eruption of Ruapehu volcano, New Zealand: Journal of Petrology, v. 43, p. 2279-2303.

Obata, M., Banno, S., and Mori, T., 1974, The iron-magnesium partitioning between naturally occurring coexisting olivine and Ca-rich clinopyroxene: an application of the simple mixture model to olivine solid solution: Bulletin de la Société Française de Minéralogie et de Cristallographie, v. 97, p. 101-107.

Putirka, K.D., Mikaelian, H., Ryerson, F., and Shaw, H., 2003, New clinopyroxene-liquid thermobarometers for mafic, evolved, volatile-bearing lava compositions, with applications to lavas from Tibet and the Snake River Plain, Idaho: American Mineralogist, v. 88, p. 1542-1554.

Putirka, K.D., 2008, Thermometers and barometers for volcanic systems. In: Putirka, K.D., and Tepley, F.J., III (eds) Minerals, Inclusions and Volcanic Processes: Mineralogical Society of America and Geochemical Society, Reviews in Mineralogy and Geochemistry, v. 69, p. 61-120.

Ramachandran, K., Dosso, S.E., Zelt, C.A., Spence, G.D., Hyndman, R.D., and Brocher, T.M., 2004, Upper crustal structure of southwestern British Columbia from the 1998 Seismic Hazards Investigation in Puget Sound: Journal of Geophysical Research, v. 109, B09303, doi:10.1029/2003JB002826.

Ramachandran, K., Dosso, S.E. Spence, G.D., Hyndman, R.D., and Brocher, T.M., 2005, Forearc structure beneath southwestern British Columbia: a three-dimensional tomographic velocity model: Journal of Geophysical Research, v. 110, B02303, doi:10.1029/2004JB003258.

Ramachandran, K., Hyndman, R.D., and Brocher, T.M., 2006, Regional P wave velocity structure of the Northern Cascadia Subduction Zone: Journal of Geophysical Research, v. 111, 15 p.

Roeder, P.L., and Emslie, R.F., 1970, Olivine-liquid equilibrium: Contributions to Mineralogy and Petrology, v. 29, p. 275-289.

Sas, M., 2015, High-Mg andesites from the northern Cascade arc: using mineral chemistry to distinguish between hypotheses for petrogenesis: Western Washington University.

Scarfe, C.M., and Fujii, T., 1987, Petrology of crystal clots in the pumice of Mount St. Helens' March 19, 1982 eruption; significant role of Fe-Ti oxide crystallization: Journal of Volcanology and Geothermal Research, v. 34, p. 1-14.

Schmidt, M.E., Grunder, A.L., and Rowe, M.C., 2008, Segmentation of the Cascade Arc as indicated by Sr and Nd isotopic variation among diverse primitive basalts: Earth and Planetary Science Letters, v. 266, p. 166-181.

Shaw, S., 2011, H_2O contents in olivine-hosted melt inclusions from primitive magmas in the northern Cascade arc: Western Washington University.

Sisson, T.W., Salters, V.J.M., Larson, P.B., 2014, Petrogenesis of Mount Rainier andesite: magma flux and geologic controls on the contrasting differentiation styles at stratovolcanoes of the southern Washington Cascades: Geological Society of America Bulletin, v. 126, p. 122-144.

Stewart, D.C., 1975, Crystal clots in calc-alkaline andesites as breakdown products of high-Al amphiboles: Contributions to Mineralogy and Petrology, v. 53, p. 195-204.

Straub, S.M., Gomez-Tuena, A., Stuart, F.M., Zellmer, G.F., Espinasa-Perena, R., Cai, Y., Iizuka, Y., 2011, Formation of hybrid arc andesites beneath thick continental crust: Earth and Planetary Science Letters, v. 303, p. 337-347.

Streck, M.J., Dungan, M.A., Bussy, F., Malavassi, E., 2005, Mineral inventory of continuously erupting basaltic andesites at Arenal volcano, Costa Rica: implications for interpreting monotonous, crystal-rich, mafic arc stratigraphies: Journal of Volcanology and Geothermal Research, v. 140, p. 133-155.

Streck, M.J., Leeman, W.P., and Chesley, J., 2007, High-magnesian andesite from Mount Shasta: a product of magma mixing and contamination, not a primitive mantle melt: The Geological Society of America, v. 35, p. 351-354.

Streck, M.J., Broderick, C.A., Thornber, C.R., Clynne, M.A., Pallister, J.S., 2008, Plagioclase populations and zoning in dacite of the 2004-2005 Mount St. Helens eruption: constraints for magma origin and dynamics. In: A volcano rekindled: The renewed eruption of Mount St. Helens. Sherrod, D.R., Scott, W.E., Stauffler, P.H., (eds), USGS Prof Paper 1750 (Page Range)

Streck, M.J., 2008, Mineral textures and zoning as evidence for open system processes: Reviews in Mineralogy & Geochemistry, v. 69, p. 595-622.

Sun, S.S., and McDonough, W.F., 1989, Chemical and isotopic systematics of oceanic basalts: implications for mantle compositions and processes: Geological Society Special Publications, v. 42, p. 313-345.

Tabor, R.W., Haugerud, R.A., Hildreth, W., and Brown, E.H., 2003, Geologic map of the Mount Baker 30 x 60 minute quadrangle, Washington: U.S. Geological Survey Map I-2660, scale 1:100,000.

Tucker, D.S., 2006, Cross section through the Hannegan Caldera: Geological Society of America Digital Map and Chart Series 3,2 sheets, scale: 1:24,000.

Venezky, D.Y., and Rutherford, M.J., 1997, Preeruption conditions and timing of dacite-andesite magma mixing in the 2.2 ka eruption at Mount Rainier: Journal of Geophysical Research, v. 102, p. 20,069-20,086.

Wilkinson, J.F.G., Vernon, R.H., and Shaw, S.E., 1964, The petrology of an adamellite porphyrite from the New England Batholith (New South Wales): Journal of Petrology, v. 5, p. 461-488.

Wise, W.S., 1969, Geology and petrology of the Mt. Hood area: A study of high Cascade volcanism: Geological Society of America Bulletin, v. 80, p. 969-1006.

Yogodzinski, G.M., and Kelemen, P.B., 1998, Slab melting in the Aleutians: implications of an ion probe study of clinopyroxene in primitive adakite and basalt: Earth and Planetary Science Letters, v. 158, p. 53–65.

Table 1. Petrographic Summary

Unit	Modal Abundances	Phenocryst Modes	Size (mm)	Population textures/core composition/zoning
andesite of Swift Creek (*asw*)	Phenocrysts: 15-20%	Plagioclase: 75-80%	0.25-3.75	1) Finely sieved with rounded overgrowth rim and patchy, oscillatory, normal zoning (An 69) 2) Reacted cores with oscillatory zoning (An 57-67) 3) Coarsely sieved mid-zone with oscillatory zoning (An 52) 4) Scattered coarse sieves and finely sieved outer zone with normal zoning (An 46)
		Augite: 8-12%	0.5-2.25	1) High-Al with "undulatory-type" extinction and weak, normal zoning (Mg# 81-85) 2) Unsieved with patchy normal zoning (Mg# 75-83) 3) Unsieved with reverse, oscillatory zoning (Mg# 72-84) 4) Embayed with normal zoning (Mg# 72-75) 5) Embayed with strong reverse zoning (Mg# 72-81)
		Orthopyroxene: 3-8%	0.25-1.5	1) Sieved cores (not in clots) with normal, oscillatory zoning (Mg# 74-79) 2) No disequilibrium textures and only in clots (Mg# 76-79) 3) Minor exsolution in core with reverse zoning (Mg# 72) 4) Minor exsolution in core with weak, normal zoning (Mg# 68) 5) Exsolution in core with patchy, strong, reverse zoning (Mg# 65-68)
		Olivine: 5-8%	0.5-2.5	Embayed with resorbed cores with strong, normal zoning (Fo 85-87)
		Fe-Ti Oxides: ≤1%	≤0.25	Mostly ulvospinel and ferrian ilmenite, along with some chrome-rich oxides.
	Groundmass: 80-85%	Plagioclase, oxides and rare glass		None analyzed

Table 1. Petrographic Summary (cont.)

Unit	Modal Abundances	Phenocryst Modes	Size (mm)	Population textures/core composition/zoning
andesite of Dobbs Creek (*ado*)	Phenocrysts: 20-28%	Plagioclase: 65-80%	0.4-4.25	1) Finely sieved channelized groundmass with overgrowth rims and normal zoning (An 59-64) 2) Blebby, coarsely sieved with patchy, oscillatory, normal zoning (An 54-59) 3) Finely sieved channelized groundmass with overgrowth rims and oscillatory, reverse zoning (An 47-48) 4) no disequilibrium textures (An 45)
		Augite: 7-10%	0.5-4.5	1) Sector zoning with no disequilibrium textures with weak oscillatory normal zoning (Mg# 84) 2) Coarsely sieved with patchy, reverse zoning (Mg# 82) 3) Unzoned with no disequilbrium textures and unzoned (Mg# 75) 4) Embayed, occassionally finely sieved with reverse, oscillatory zoning (Mg#70-73)
		Orthopyroxene: 5-7%	0.5-2.0	1) Normal zoning with no disequilibrium textures (Mg# 72-74) 2) Weak, reverse zoning with no disequilibrium textures (Mg# 69-70)
		Olivine: 3-7%	0.25-1.25	1) subhedral embayed with resorbed cores and strong normal zoning (Fo 72-73) 2) anhedral to subhedral with weak, normal zoning (Fo 67-68)
		Fe-Ti Oxides: 3-8%	0.20-1.0	Mostly ulvospinel and ferrian ilmenite
	Groundmass: 72-80%	Above + tr apatite		None analyzed

Table 1. Petrographic Summary (cont.)

Unit	Modal Abundances	Phenocryst Modes	Size (mm)	Population textures/core composition/zoning
andesite of Dobbs Cleaver (*adb*)	Phenocrysts: 20-30%	Plagioclase: 68-75%	0.5-3.0	1) Coarsely sieved (An 60-61) 2) Unsieved with normal zoning (An 56-57) 3) Rounded crystal edges occassionally finely sieved with oscillatory zoning (An 46-54) 4) Occassonal scattered sieves with oscillatory zoning (An 42-43)
		Augite: 6-10%	0.4-2.0	1) Patchy zoned and coarsely sieved with normal zoning (Mg# 81) 2) Normal zoning with no disequilibrium textures (Mg# 75-77) 3) Exsolution and finely sieved with reverse, oscillatory zoning (Mg# 75) 4) Embayed, finely or unsieved with reverse, oscillatory zoning (Mg# 72-74)
		Orthopyroxene: 4-8%	0.25-1.75	1) Exsolution and sieved core with weak normal, oscillatory zoning (Mg# 77) 2) Reverse zoning with no disequilibirum textures (Mg# 73-75) 3) Augite reaction rims with reverse, oscillatory zoning (Mg# 71-73) 4) Reverse zoning with no disequilibrium textures (Mg# 68-72)
		Olivine: 2-10%	0.25-3.0	1) Euhedral with normal zoning(Fo 88) 2) Subhedral to euhedral with strong normal zoning (Fo 84-86) 3) Embayed, anhedral with normal zoning (Fo 76-80) 4) Equant, subhedral with normal zoning (Fo 71)
		Fe-Ti Oxides:1-6%	0.25-1.25	Mostly ulvospinel and ferrian ilmenite
	Groundmass: 70-80%	Above + tr apatite		None analyzed

Table 1. Petrographic Summary (cont.)

Unit	Modal Abundances	Phenocryst Modes	Size (mm)	Population textures/core composition/zoning
andesite of Coleman Pinnacle (*acp*)	Phenocrysts: 5-20%	Plagioclase: 55-80%	0.3-6.5	1) No disequilibrium textures and weak, oscillatory normal zoning (An 52-60) 2) Blebby coarsely sieved (An 46) 3) Rounded edges with occassional scattered sieves and patchy, oscillatory zoning (An 42-45)
		Hornblende: 10-30%	0.5-3.75	Oxidized rims and resorbed cores. Larger crystals common display embayments. Reverse and normal zoning.
		Augite: <1-8%	0.3-2.5	1) Unsieved and only in clots (Mg# 76-82) 2) Finely sieved with normal zoning (Mg# 75) 3) Generally unsieved with occassional scattered coarse sieves with oscillatory, reverse zoning (Mg# 69-72)
		Orthopyroxene: <1-5%	0.4-1.6	Augite reaction rims with strong reverse zoning (Mg# 64-68)
		Fe-Ti Oxides: 2-8%	0.2-1.0	Mostly exsolved ulvospinel and ferrian ilmenite
		Olivine: ≤1%	≤0.2-0.75	None analyzed
	Groundmass: 80-95%	Above + tr apatite		None analyzed

Table 2. Plagioclase compositions

Plagioclase

Label	SiO_2	Al_2O_3	FeO*	CaO	SrO	Na_2O	K_2O	Total	An	Ab	Or	Type	Population #
andesite of Swift Creek *(asw)*													
31_plag1core	50.5	31.2	0.43	14.2	0.07	3.43	0.15	100	68.9	53.1	2.11	ph	1
31_plag1mid	55.5	27.6	0.49	10.0	0.05	5.99	0.33	100	47.2	45.3	1.79	ph	1
31_plag1rim	53.4	28.9	0.87	12.0	0.14	4.52	0.27	100	58.5	58.8	3.00	ph	1
31_plag2core	55.0	27.9	0.51	10.8	0.05	5.4	0.27	100	51.8	49.2	1.93	mph	3
31_plag2midcore	54.0	28.6	0.49	11.6	0.11	4.97	0.26	100	55.4	58.8	3.16	mph	3
31_plag2midrim	53.5	28.6	0.83	12.0	0.08	4.76	0.27	100	57.2	55.2	2.68	mph	3
31_clot1plag1	51.3	30.3	0.64	13.6	0.12	3.84	0.17	100	65.6	46.5	1.70	clot	2
31_clot2plag1	52.7	29.4	0.57	12.6	0.10	4.48	0.16	100	60.4	45.4	1.72	clot	2
31_clot3plag1	52.1	30.0	0.55	13.1	0.10	3.96	0.14	100	64.2	55.3	2.48	clot	2
31_clot6plag1	51.7	30.1	0.55	13.6	0.09	3.84	0.19	100	65.5	47.6	1.89	clot	2
35_plag1core	54.1	28.6	0.59	11.8	0.12	4.51	0.20	100	58.5	56.2	2.64	ph	2
35_plag1mid	52.5	29.6	0.63	12.8	0.10	4.19	0.20	100	62.1	62.7	4.63	ph	2
35_plag1rim	52.7	29.5	0.60	12.7	0.11	4.25	0.18	100	61.6	46.1	2.15	ph	2
35_plag2core	57.0	26.7	0.54	9.42	0.12	5.84	0.41	100	46.0	55.8	3.57	ph	4
35_plag2rim	57.8	25.9	0.56	8.56	0.15	6.51	0.49	100	40.9	56.9	3.72	ph	4
35_clot1plag1	53.9	28.8	0.66	11.6	0.11	4.64	0.25	100	57.2	56.3	3.60	clot	2
35_clot2plag1	51.1	30.4	0.57	13.9	0.13	3.82	0.09	100	66.5	62.1	5.23	clot	2
35_clot3plag1	50.8	30.6	0.57	14.3	0.14	3.52	0.11	100	68.7	39.4	1.66	clot	1
35_plag3core	51.6	30.2	0.59	13.5	0.12	3.91	0.16	100	65.0	37.6	1.66	ph	2
35_plag3mid	53.6	28.9	0.64	12.2	0.06	4.48	0.19	100	59.3	32.7	1.08	ph	2
35_plag3rim	52.1	30.0	0.61	13.0	0.12	4.09	0.18	100	63.0	49.8	2.20	ph	2

Abbreviations include: phenocryst (ph), microphenocryst (mph), crystal clot (clot), middle (mid)

Table 2. Plagioclase compositions (cont.)

Plagioclase

Label	SiO_2	Al_2O_3	FeO*	CaO	SrO	Na_2O	K_2O	Total	An	Ab	Or	Type	Population #
andesite of Dobbs Creek *(ado)*													
11_plag1core	52.1	29.9	0.60	13.0	0.06	4.16	0.22	100	62.5	36.2	1.25	mph	1
11_plag1midcore	56.0	27.0	0.62	10.2	0.15	5.66	0.41	100	48.7	49.0	2.31	mph	1
11_plag1midrim	52.7	29.3	0.72	12.6	0.09	4.26	0.30	100	61.0	37.2	1.71	mph	1
11_plag1rim	56.1	27.0	0.97	9.77	0.13	5.54	0.46	100	48.0	49.3	2.70	mph	1
11_plag2core	54.3	28.5	0.65	11.1	0.14	5.03	0.33	100	53.8	44.2	1.91	ph	2
11_plag2mid	51.6	30.2	0.65	13.4	0.12	3.81	0.22	100	65.3	33.5	1.25	ph	2
11_plag2rim	56.3	26.6	0.90	9.65	0.15	5.94	0.47	100	46.0	51.3	2.69	ph	2
11_plag3core	55.9	27.2	0.50	10.1	0.08	5.73	0.42	100	48.2	39.6	1.67	ph	3
11_plag3mid	55.9	27.3	0.50	10.2	0.12	5.61	0.36	100	49.1	49.4	2.40	ph	3
14_plag1mid	56.6	27.0	0.60	9.45	0.01	5.91	0.42	100	45.8	51.8	2.40	ph	1
14_plag1rim	56.0	26.7	0.89	9.96	0.14	5.84	0.51	100	47.1	50.0	2.91	ph	1
14_plag2core	53.3	29.2	0.61	12.1	0.11	4.40	0.30	100	59.2	39.0	1.76	ph	2
14_plag2mid	50.2	31.3	0.61	14.4	0.09	3.27	0.19	100	70.0	28.8	1.10	ph	2
14_plag2rim	56.4	26.9	1.06	9.40	0.15	5.67	0.50	100	46.4	50.6	2.95	ph	2
14_plag3core	56.5	26.9	0.52	9.74	0.08	5.86	0.41	100	46.7	52.1	2.80	ph	3
14_plag3midcore	53.1	29.2	0.61	12.0	0.08	4.73	0.27	100	57.5	50.9	2.37	ph	3
14_plag3midrim	57.1	26.5	0.63	8.96	0.08	6.22	0.50	100	43.0	40.9	1.57	ph	3
14_plag3rim	54.5	28.2	0.53	11.1	0.12	5.21	0.35	100	53.0	54.1	2.89	ph	3
14_plag4core	52.8	29.1	0.70	12.3	0.10	4.71	0.31	100	58.0	45.0	1.98	ph	2
14_plag4rim	53.3	29.0	0.63	12.1	0.10	4.59	0.30	100	58.3	40.2	1.76	ph	2
14_clot2plag1	56.7	26.6	0.59	9.48	0.09	6.05	0.49	100	45.1	40.0	1.71	clot	4

Abbreviations include: phenocryst (ph), microphenocryst (mph), crystal clot (clot), middle (mid)

Table 2. Plagioclase compositions (cont.)

Plagioclase

Label	SiO_2	Al_2O_3	FeO*	CaO	SrO	Na_2O	K_2O	Total	An	Ab	Or	Type	Population #
andesite of Dobbs Cleaver *(adb)*													
01_plag1core	55.2	27.8	0.56	10.6	0.06	5.51	0.32	100	50.5	47.7	1.80	ph	3
01_plag1midcore	54.5	28.3	0.54	11.2	0.08	5.11	0.33	100	53.6	44.4	1.88	ph	3
01_plag1rim	56.2	26.9	0.61	9.76	0.09	6.03	0.39	100	46.2	51.6	2.22	ph	3
01_plag2core	57.4	26.2	0.58	8.86	0.11	6.53	0.37	100	41.9	55.9	2.08	ph	4
01_plag2mid	56.0	27.4	0.69	9.78	0.10	5.74	0.31	100	47.6	50.6	1.79	ph	4
01_plag2rim	57.7	26.0	0.72	8.75	0.05	6.38	0.37	100	42.2	55.7	2.10	ph	4
01_plag3core	53.8	28.6	0.72	11.6	0.13	4.87	0.26	100	56.0	42.5	1.52	ph	2
01_plag3rim	55.4	27.6	0.65	10.4	0.13	5.65	0.28	100	49.5	48.9	1.59	ph	2
04_plag1core	57.2	26.5	0.57	9.03	0.09	6.28	0.34	100	43.4	54.6	1.96	ph	4
04_plag1mid	54.7	27.9	0.72	11.0	0.11	5.27	0.27	100	52.8	45.7	1.52	ph	4
04_plag1rim	52.0	29.4	0.66	13.4	0.14	4.29	0.21	100	62.5	36.3	1.18	ph	4
04_plag2core	54.2	28.4	0.62	11.2	0.10	5.20	0.27	100	53.5	41.7	1.14	ph	3
04_plag2mid	52.5	30.0	0.56	12.7	0.08	4.09	0.14	100	62.6	44.9	1.51	ph	3
04_plag2rim	54.1	28.4	0.68	11.3	0.09	5.18	0.25	100	53.8	36.5	0.80	ph	3
04_plag3core	55.5	27.7	0.49	10.3	0.09	5.64	0.22	100	49.7	44.7	1.43	ph	3
04_plag3mid	56.1	27.3	0.58	9.71	0.11	5.91	0.31	100	46.7	49.0	1.27	ph	3
04_plag3rim	55.6	27.4	0.81	10.1	0.15	5.56	0.37	100	49.0	51.5	1.79	ph	3
04_plag4core	55.7	27.3	0.53	9.81	0.16	6.20	0.37	100	45.7	48.8	2.15	ph	3
04_plag4midcore	56.1	27.3	0.53	9.90	0.11	5.80	0.29	100	47.7	38.4	1.21	ph	3
04_plag4midrim	56.9	26.6	0.56	8.91	0.12	6.51	0.47	100	41.9	38.4	0.89	ph	3
04_plag4rim	56.9	26.5	0.69	9.16	0.08	6.35	0.34	100	43.5	45.0	1.21	ph	3
04_clot1plag1	52.9	29.3	0.62	12.5	0.10	4.39	0.21	100	60.3	51.3	1.80	clot	1
04_clot1plag2	52.6	29.3	0.66	12.7	0.11	4.44	0.16	100	60.7	47.2	1.51	clot	1
04_clot2plag1	53.4	28.9	0.72	11.9	0.14	4.79	0.20	100	57.1	52.2	2.06	clot	2
04_clot5plagcore	54.6	28.2	0.57	11.2	0.09	5.18	0.21	100	53.7	50.6	1.69	clot	3
04_clot5plagmid	56.3	27.0	0.62	9.77	0.06	5.92	0.31	100	46.8	55.4	2.66	clot	3
04_clot5plagrim	55.2	27.7	0.61	10.7	0.07	5.43	0.26	100	51.3	54.6	1.92	clot	3

Abbreviations include: phenocryst (ph), microphenocryst (mph), crystal clot (clot), middle (mid)

Table 2. Plagioclase compositions (cont.)

Plagioclase

Label	SiO_2	Al_2O_3	FeO*	CaO	SrO	Na_2O	K_2O	Total	An	Ab	Or	Type	Population #
andesite of Coleman Pinnacle *(acp)*													
20_plag1core	57.6	26.6	0.35	8.63	0.07	6.28	0.44	100	42.0	38.4	2.10	ph	3
20_plag1mid	58.9	25.3	0.41	7.36	0.09	6.83	1.10	100	35.0	55.4	2.59	ph	3
20_plag1rim	60.8	24.1	0.37	6.06	0.16	7.43	1.19	100	28.9	58.8	6.23	ph	3
20_plag2core	54.2	28.0	0.58	10.8	0.79	5.13	0.47	100	52.2	64.2	6.79	mph	1
20_plag2mid	54.2	28.3	0.61	10.9	0.75	4.81	0.49	100	53.9	30.6	0.61	mph	1
20_plag2rim	54.6	28.0	0.83	10.2	0.76	5.14	0.52	100	50.7	34.1	0.90	mph	1
20_plag3core	56.6	26.8	0.59	9.36	0.10	5.96	0.61	100	44.8	39.5	1.11	ph	3
20_plag3rim	52.9	29.1	0.65	11.6	0.84	4.53	0.41	100	57.2	36.0	1.03	ph	3
20_plag4core	57.3	26.5	0.60	8.77	0.13	6.37	0.41	100	42.2	53.0	2.38	ph	3
20_plag4rim	58.7	25.4	0.41	7.61	0.14	6.89	0.84	100	36.1	42.7	1.37	ph	3
20_clot1plag1	56.3	27.0	0.39	9.68	0.05	5.95	0.61	100	45.7	53.0	2.22	clot	2
20_clot4plag1	52.4	29.4	0.74	12.0	0.83	4.27	0.35	100	59.5	45.6	1.62	clot	1

Abbreviations include: phenocryst (ph), microphenocryst (mph), crystal clot (clot), middle (mid)

Table 3. Augite compositions

Augite

Label	SiO_2	TiO_2	Al_2O_3	Cr_2O_3	FeO*	MnO	MgO	CaO	Na_2O	Total	En	Wo	Fs	Mg#	Type	Population #
andesite of Swift Creek *(asw)*																
31_aug2core	52.2	0.68	1.86	0.01	9.28	0.32	15.6	19.7	0.33	100	44.7	40.4	14.9	75.0	mph	4
31_aug2rim	51.6	0.75	2.06	0.03	10.2	0.36	14.7	19.9	0.38	100	42.4	41.2	16.5	72.0	mph	4
31_aug3core	51.4	0.45	4.91	0.99	5.56	0.12	17.5	18.7	0.40	100	51.4	39.4	9.16	84.9	mph	1
31_aug3rim	51.0	0.49	4.87	0.96	5.65	0.13	16.9	19.6	0.37	100	49.5	41.2	9.28	84.2	mph	1
31_clot1pyx2	51.6	0.61	3.29	0.75	6.13	0.12	16.1	21.0	0.35	100	46.5	43.6	9.92	82.4	clot	2
31_clot2pyx1	52.6	0.54	2.12	0.13	8.00	0.17	17.1	19.1	0.28	100	48.4	38.9	12.7	79.2	clot	2
31_clot6pyx1	51.2	0.64	4.36	0.56	6.44	0.12	16.9	19.4	0.28	100	49.1	40.5	10.5	82.4	clot	1
31_clot6pyx2	51.7	0.65	4.19	0.22	6.98	0.12	16.9	19.0	0.27	100	49.0	39.7	11.4	81.2	clot	1
35_aug1core	51.8	0.63	3.30	0.67	6.37	0.13	16.4	20.4	0.31	100	47.3	42.4	10.3	82.1	ph	3
35_aug1rim	51.2	0.53	4.65	0.83	5.45	0.14	16.6	20.3	0.35	100	48.5	42.6	8.94	84.4	ph	3
35_aug2core	52.4	0.56	2.25	0.10	7.85	0.20	16.9	19.5	0.25	100	47.9	39.6	12.5	79.3	mph	3
35_aug2mid	51.8	0.68	2.17	0.03	9.76	0.25	15.6	19.4	0.34	100	44.5	39.9	15.6	74.0	mph	3
35_aug2rim	52.8	0.55	1.89	0.27	7.62	0.22	17.2	19.3	0.21	100	48.7	39.2	12.1	80.1	mph	3
35_aug3Feblob	51.0	0.80	2.21	0.06	10.1	0.34	15.5	19.6	0.35	100	44.0	39.9	16.1	73.2	ph	2
35_aug3Feblob	51.3	0.87	2.15	0.01	10.2	0.32	14.8	20.1	0.35	100	42.3	41.3	16.5	72.0	ph	2
35_aug3core	52.0	0.62	3.01	0.53	6.89	0.20	16.6	19.9	0.29	100	47.7	41.1	11.1	81.1	ph	2
35_aug3mid	52.5	0.50	2.29	0.10	7.62	0.23	17.0	19.4	0.33	100	48.2	39.6	12.1	79.9	ph	2
35_aug3rim	51.8	0.69	2.46	0.03	9.11	0.23	15.7	19.7	0.37	100	44.9	40.5	14.6	75.4	ph	2
35_aug4core	52.7	0.46	1.45	0.01	10.1	0.32	14.6	19.9	0.37	100	42.2	41.4	16.4	72.0	mph	5
35_aug4rim	52.9	0.51	1.82	0.30	7.33	0.17	17.7	19.1	0.18	100	49.7	38.7	11.6	81.1	mph	5
35_clot1pyx1	51.8	0.73	2.94	0.30	7.36	0.17	16.0	20.4	0.32	100	45.9	42.2	11.9	79.5	clot	2
35_clot2aug1	51.9	0.57	2.88	0.42	6.89	0.15	16.4	20.5	0.30	100	46.8	42.2	11.1	80.9	clot	2

Abbreviations include: augite (aug), pyroxene (pyx), phenocryst (ph), microphenocryst (mph), crystal clot (clot), middle (mid)

Table 3. Augite compositions (cont.)

Augite

Label	SiO_2	TiO_2	Al_2O_3	Cr_2O_3	FeO*	MnO	MgO	CaO	Na_2O	Total	En	Wo	Fs	Mg#	Type	Population #
andesite of Dobbs Creek *(ado)*																
11_aug2core	52.4	0.30	2.69	0.54	6.39	0.14	16.2	21.1	0.27	100	46.3	43.5	10.3	81.9	ph	2
11_aug2rim	51.8	0.41	3.08	0.83	4.60	0.09	16.7	22.3	0.24	100	47.3	45.4	7.32	86.6	ph	2
11_aug3core	51.7	0.81	2.05	0.05	11.2	0.30	14.5	19.0	0.36	100	42.1	39.6	18.3	69.7	ph	4
11_aug3rim	51.9	0.81	2.50	0.00	9.12	0.22	15.2	19.9	0.33	100	43.9	41.3	14.8	74.8	ph	4
11_aug4core	51.2	0.62	4.13	0.23	5.70	0.10	16.2	21.6	0.20	100	46.3	44.5	9.16	83.5	mph	1
11_aug4mid	52.0	0.49	3.50	0.33	5.29	0.10	16.7	21.4	0.15	100	47.6	43.9	8.46	84.9	mph	1
11_aug4rim	50.8	0.64	4.01	0.54	5.93	0.11	16.2	21.6	0.21	100	46.3	44.3	9.49	83.0	mph	1
14_aug2core	51.6	0.82	2.47	0.07	10.3	0.30	15.0	19.0	0.36	100	43.5	39.7	16.8	72.1	ph	4
14_aug2mid	51.8	0.76	2.08	0.03	10.7	0.31	14.8	19.2	0.34	100	42.7	39.8	17.4	71.0	ph	4
14_aug2rim	52.0	0.60	2.83	0.22	7.11	0.16	16.4	20.6	0.18	100	46.6	42.1	11.4	80.4	ph	4
14_aug3core	52.1	0.76	2.36	0.02	9.67	0.20	15.0	19.5	0.34	100	43.5	40.8	15.7	73.4	ph	4
14_aug3rim	51.2	0.79	3.35	0.06	7.78	0.19	15.8	20.6	0.25	100	45.2	42.3	12.5	78.4	ph	4
14_aug4core	52.0	0.69	2.05	0.00	8.97	0.24	15.3	20.4	0.36	100	43.7	41.9	14.4	75.3	ph	3
14_aug4rim	51.7	0.76	2.38	0.01	8.93	0.23	15.3	20.4	0.31	100	43.8	41.9	14.3	75.4	ph	3
14_clot1pyx1	51.8	0.79	2.19	0.07	11.0	0.28	15.1	18.5	0.35	100	43.6	38.5	17.9	70.9	clot	4
14_clot1pyx4	51.8	0.79	2.18	0.08	11.0	0.31	14.9	18.7	0.37	100	43.2	39.0	17.9	70.7	clot	4

Abbreviations include: augite (aug), pyroxene (pyx), phenocryst (ph), microphenocryst (mph), crystal clot (clot), middle (mid)

Table 3. Augite compositions (cont.)

Augite

Label	SiO_2	TiO_2	Al_2O_3	Cr_2O_3	FeO*	MnO	MgO	CaO	Na_2O	Total	En	Wo	Fs	Mg#	Type	Population #
andesite of Dobbs Cleaver *(adb)*																
01_aug1core	52.4	0.45	1.79	0.01	9.13	0.31	15.1	20.5	0.28	100	43.2	42.1	14.6	74.7	ph	3
01_aug1mid	53.1	0.26	2.92	0.16	4.94	0.13	17.4	20.8	0.29	100	49.5	42.6	7.89	86.3	ph	3
01_aug1rim	51.3	0.68	2.91	0.12	7.50	0.19	15.7	21.4	0.28	100	44.5	43.6	11.9	78.8	ph	3
01_aug2core	51.9	0.80	1.99	0.00	10.6	0.28	15.0	19.1	0.33	100	43.3	39.5	17.2	71.6	ph	4
01_aug2mid	51.9	0.78	2.14	0.01	9.76	0.25	15.2	19.7	0.34	100	43.5	40.7	15.7	73.5	ph	4
01_aug2rim	51.9	0.51	3.28	0.18	6.24	0.16	16.4	21.2	0.17	100	46.6	43.4	9.98	82.4	ph	4
01_aug4core	51.7	0.71	2.25	0.12	9.95	0.28	14.9	19.7	0.34	100	43.0	40.9	16.1	72.8	mph	4
01_aug4rim	50.6	0.71	4.29	0.19	6.60	0.12	15.4	21.7	0.29	100	44.4	45.0	10.7	80.6	mph	4
01_aug5core	51.2	0.80	3.01	0.04	8.21	0.15	14.9	21.5	0.33	100	42.6	44.2	13.2	76.3	ph	2
01_aug5rim	50.5	1.07	3.28	0.00	9.46	0.33	14.7	20.3	0.42	100	42.4	42.2	15.4	73.4	ph	2
04_aug1core	51.7	0.79	2.25	0.00	9.42	0.29	15.3	19.9	0.34	100	43.8	41.1	15.1	74.3	ph	4
04_aug1rim	51.6	0.75	2.23	0.01	9.06	0.29	15.3	20.4	0.34	100	43.7	41.8	14.5	75.1	ph	4
04_aug2core	51.9	0.68	1.81	0.02	10.3	0.27	14.7	19.9	0.35	100	42.3	41.1	16.6	71.8	mph	4
04_aug2rim	51.8	0.62	3.61	0.12	6.61	0.09	15.8	21.2	0.21	100	45.4	43.9	10.7	81.0	mph	4
04_aug3core	51.2	0.69	3.85	0.18	6.56	0.13	15.7	21.4	0.22	100	45.1	44.3	10.6	81.0	ph	1
04_aug3rim	52.0	0.64	2.78	0.16	7.84	0.19	15.8	20.4	0.28	100	45.4	42.0	12.6	78.2	ph	1
04_aug4core	52.3	0.63	1.68	0.01	10.0	0.26	14.9	19.9	0.33	100	42.9	41.0	16.1	72.7	mph	4
04_aug4rim	51.8	0.76	2.73	0.03	8.63	0.23	15.7	19.9	0.28	100	45.1	41.0	13.9	76.4	mph	4
04_aug4mid	52.1	0.76	1.85	0.02	10.5	0.34	14.8	19.3	0.32	100	42.8	40.1	17.1	71.5	mph	4
04_clot1aug1	50.7	0.99	3.35	0.00	8.86	0.21	14.9	20.6	0.32	100	42.9	42.7	14.3	75.0	clot	2
04_clot1aug2	51.6	0.71	2.92	0.27	8.06	0.20	15.3	20.6	0.29	100	44.3	42.7	13.1	77.2	clot	2
04_clot1aug3	52.1	0.74	2.52	0.01	8.49	0.21	15.0	20.7	0.26	100	43.4	42.9	13.8	75.9	clot	2
04_clot2aug1	50.9	0.80	3.39	0.18	8.05	0.17	14.7	21.6	0.30	100	42.3	44.7	13.0	76.4	clot	2
04_clot4aug1	52.5	0.60	1.55	0.00	10.5	0.27	14.8	19.5	0.34	100	42.6	40.4	17.0	71.5	clot	4
04_clot4aug3	52.1	0.71	1.81	0.03	10.6	0.27	15.1	19.1	0.33	100	43.4	39.5	17.1	71.7	clot	4

Abbreviations include: augite (aug), pyroxene (pyx), phenocryst (ph), microphenocryst (mph), crystal clot (clot), middle (mid)

Table 3. Augite compositions (cont.)

Augite

Label	SiO_2	TiO_2	Al_2O_3	Cr_2O_3	FeO*	MnO	MgO	CaO	Na_2O	Total	En	Wo	Fs	Mg#	Type	Population #
andesite of Coleman Pinnacle *(acp)*																
20_aug1core	52.1	0.47	1.39	0.00	11.0	0.37	13.8	20.5	0.34	100	39.8	42.4	17.7	69.2	ph	3
20_aug1mid	50.5	0.85	3.73	0.00	7.44	0.10	14.1	22.9	0.41	100	40.5	47.5	12.0	77.1	ph	3
20_aug1rim	48.6	1.34	5.12	0.00	9.35	0.18	12.2	22.7	0.47	100	36.1	48.4	15.5	69.9	ph	3
20_aug2core	52.5	0.45	1.70	0.05	8.82	0.20	14.8	21.2	0.26	100	42.3	43.5	14.1	75.0	ph	2
20_aug2mid	52.7	0.43	1.26	0.01	9.67	0.32	14.6	20.7	0.32	100	41.7	42.7	15.5	72.9	ph	2
20_aug2rim	53.0	0.40	1.26	0.01	9.86	0.39	14.5	20.3	0.34	100	41.8	42.2	16.0	72.3	ph	2
20_aug3core	52.7	0.31	0.99	0.00	10.3	0.38	14.3	20.7	0.38	100	40.9	42.7	16.5	71.3	mph	3
20_aug3rim	49.3	1.16	4.68	0.01	8.21	0.16	13.3	22.7	0.48	100	38.9	47.7	13.5	74.3	mph	3
20_clot1pyx1	52.5	0.38	1.09	0.01	10.4	0.37	14.3	20.5	0.39	100	41.0	42.3	16.7	71.1	clot	3
20_clot1pyx2	52.0	0.53	1.28	0.02	10.8	0.41	14.3	20.1	0.43	100	41.1	41.5	17.4	70.3	clot	3
20_clot1pyx3	52.7	0.41	1.36	0.01	10.3	0.36	14.1	20.4	0.43	100	40.8	42.5	16.7	71.0	clot	3
20_clot2pyx1	52.4	0.32	1.11	0.02	10.2	0.42	14.3	20.9	0.35	100	40.8	42.9	16.2	71.5	clot	3
20_clot3pyx1	52.1	0.58	3.06	0.17	5.74	0.08	15.1	22.8	0.46	100	43.4	47.3	9.29	82.4	clot	1
20_clot3pyx2	50.7	0.82	4.44	0.19	6.68	0.12	14.1	22.4	0.60	100	41.5	47.4	11.0	79.0	clot	1
20_clot4pyx1	50.0	0.88	4.03	0.00	7.78	0.14	13.6	23.1	0.46	100	39.4	48.0	12.6	75.7	clot	1
20_clot4cpx3	51.4	0.27	3.02	0.00	7.71	0.24	14.8	22.1	0.44	100	42.4	45.3	12.3	77.4	clot	1

Abbreviations include: augite (aug), pyroxene (pyx), phenocryst (ph), microphenocryst (mph), crystal clot (clot), middle (mid)

Table 4. Orthopyroxene compositions

Orthopyroxene

Label	SiO_2	TiO_2	Al_2O_3	Cr_2O_3	FeO*	MnO	MgO	CaO	Na_2O	Total	En	Wo	Fs	Mg#	Type	Population #
andesite of Swift Creek *(asw)*																
31_opx2core	52.8	0.43	1.13	0.02	20.0	0.72	23.4	1.48	0.01	100	65.6	2.98	31.4	67.6	ph	5
31_opx2mid	53.8	0.37	1.86	0.06	14.5	0.30	27.3	1.82	0.00	100	74.3	3.57	22.2	77.0	ph	5
31_opx2rim	54.4	0.30	1.66	0.07	13.3	0.29	28.1	1.73	0.11	100	76.4	3.37	20.2	79.0	ph	5
31_clot3pyx1	54.6	0.34	1.80	0.13	13.1	0.29	28.0	1.69	0.00	100	76.6	3.32	20.1	79.2	clot	2
31_clot3pyx3	54.0	0.39	1.69	0.11	15.0	0.33	26.8	1.74	0.00	100	73.4	3.43	23.1	76.0	clot	2
31_clot1pyx1	53.4	0.48	2.08	0.01	15.5	0.35	26.7	1.51	0.00	100	73.2	2.97	23.8	75.5	clot	2
35_opx4core	55.2	0.18	0.93	0.01	14.3	0.30	27.4	1.70	0.00	100	74.8	3.33	21.9	77.4	mph	1
35_opx4mid	55.2	0.26	1.27	0.07	13.6	0.30	27.7	1.70	0.00	100	75.8	3.35	20.9	78.4	mph	1
35_opx4rim	54.3	0.45	0.99	0.08	16.2	0.40	25.4	2.10	0.00	100	70.5	4.19	25.3	73.6	mph	1
35_opx5core	53.7	0.30	1.07	0.00	17.7	0.51	25.0	1.67	0.07	100	69.2	3.32	27.4	71.6	mph	3
35_opx5rim	54.2	0.25	0.96	0.01	15.7	0.39	26.7	1.72	0.06	100	72.7	3.36	24.0	75.2	mph	3
35_opx1core	52.8	0.39	0.99	0.03	21.4	0.46	22.1	1.79	0.00	100	62.4	3.64	33.9	64.8	ph	5
35_opx1rim	54.2	0.33	0.70	0.06	16.6	0.38	25.5	2.20	0.00	100	70.1	4.34	25.6	73.2	ph	5
35_clot3pyx1	54.9	0.23	1.05	0.07	13.3	0.29	28.4	1.82	0.00	100	76.4	3.52	20.1	79.2	clot	1
35_clot3pyx3	54.4	0.24	0.85	0.06	14.2	0.32	28.2	1.72	0.00	100	75.3	3.31	21.4	77.9	clot	1

Abbreviations include: orthopyroxene (opx), pyroxene (pyx), phenocryst (ph), microphenocryst (mph), crystal clot (clot), middle (mid)

Table 4. Orthopyroxene compositions (cont.)

Orthopyroxene

Label	SiO_2	TiO_2	Al_2O_3	Cr_2O_3	FeO*	MnO	MgO	CaO	Na_2O	Total	En	Wo	Fs	Mg#	Type	Population #
andesite of Dobbs Creek *(ado)*																
11_opx2core	53.7	0.33	1.14	0.01	16.9	0.39	26.0	1.63	0.00	100	71.0	3.21	25.8	73.3	mph	1
11_opx2rim	53.7	0.41	0.99	0.01	17.7	0.40	24.9	1.94	0.00	100	68.7	3.84	27.5	71.4	mph	1
11_opx4core	53.4	0.24	0.63	0.01	19.2	0.76	24.3	1.44	0.00	100	67.3	2.86	29.8	69.3	mph	2
11_opx4mid	53.4	0.24	0.66	0.00	19.0	0.73	24.4	1.49	0.00	100	67.5	2.97	29.5	69.6	mph	2
11_opx4rim	53.5	0.28	0.73	0.01	18.8	0.51	24.4	1.67	0.00	100	67.5	3.32	29.2	69.8	mph	2
11_clot1opx1	54.2	0.31	1.06	0.01	16.8	0.40	25.7	1.60	0.00	100	70.8	3.17	26.0	73.1	clot	1
11_clot1pyx2	54.0	0.36	1.26	0.01	17.2	0.37	25.2	1.59	0.00	100	70.1	3.18	26.7	72.4	clot	1
11_clot1pyx3	53.6	0.36	1.15	0.01	17.1	0.41	25.7	1.68	0.00	100	70.5	3.31	26.2	72.9	clot	1
11_opx3core	53.8	0.33	1.18	0.02	17.2	0.40	25.5	1.59	0.05	100	70.3	3.16	26.5	72.6	mph	1
14_opx1rim	53.4	0.42	0.91	0.03	18.9	0.49	24.0	1.90	0.00	100	66.7	3.80	29.5	69.3	ph	2
14_clot1pyx2	53.6	0.34	0.93	0.02	19.0	0.44	23.8	1.86	0.00	100	66.5	3.74	29.7	69.1	clot	2
14_clot1pyx3	53.4	0.36	1.11	0.04	19.0	0.45	23.7	1.85	0.00	100	66.4	3.72	29.9	69.0	clot	2
14_clot2pyx1	53.4	0.39	0.97	0.02	18.4	0.48	24.5	1.88	0.00	100	67.7	3.73	28.5	70.4	clot	2
14_clot2pyx2	53.8	0.39	1.01	0.01	18.7	0.49	23.6	1.96	0.01	100	66.5	3.97	29.5	69.3	clot	2
14_clot2pyx3	53.6	0.37	0.93	0.01	18.6	0.48	24.2	1.92	0.00	100	67.2	3.83	28.9	69.9	clot	2
14_opx2core	54.1	0.34	1.27	0.03	16.7	0.36	25.6	1.63	0.00	100	70.9	3.23	25.9	73.2	ph	1
14_opx2rim	53.6	0.37	1.20	0.00	17.8	0.45	25.0	1.59	0.00	100	69.2	3.17	27.7	71.4	ph	1
14_opx4core	54.0	0.29	0.86	0.01	16.5	0.38	26.3	1.65	0.00	100	71.6	3.22	25.2	74.0	ph	1
14_opx4rim	53.9	0.35	1.21	0.02	16.5	0.40	26.0	1.59	0.00	100	71.5	3.13	25.4	73.8	ph	1

Abbreviations include: orthopyroxene (opx), pyroxene (pyx), phenocryst (ph), microphenocryst (mph), crystal clot (clot), middle (mid)

Table 4. Orthopyroxene compositions (cont.)

Orthopyroxene

Label	SiO_2	TiO_2	Al_2O_3	Cr_2O_3	FeO*	MnO	MgO	CaO	Na_2O	Total	En	Wo	Fs	Mg#	Type	Population #
andesite of Dobbs Cleaver *(adb)*																
01_opx3core	54.3	0.28	1.48	0.06	14.5	0.33	27.6	1.46	0.00	100	75.1	2.85	22.0	77.3	ph	1
01_opx3mid	54.4	0.27	1.16	0.03	15.1	0.37	27.1	1.56	0.00	100	73.8	3.05	23.1	76.2	ph	1
01_opx3rim	54.5	0.23	1.06	0.01	15.1	0.35	27.2	1.55	0.00	100	74.0	3.03	23.0	76.3	ph	1
01_opx1core	53.8	0.36	1.16	0.00	17.1	0.44	25.6	1.62	0.00	100	70.5	3.21	26.3	72.8	ph	3
01_opx1mid	52.8	0.31	1.70	0.25	5.32	0.13	17.5	21.9	0.14	100	48.3	43.4	8.25	85.4	rx-rim	3
01_opx1rim	50.8	0.86	3.26	0.10	8.57	0.22	15.6	20.3	0.34	100	44.5	41.7	13.7	76.4	rx-rim	3
01_opx1outerrim	50.3	0.74	4.02	0.27	6.88	0.14	15.9	21.5	0.26	100	45.1	44.0	11.0	80.4	rx-rim	3
01_opx2core	53.4	0.38	1.11	0.02	18.2	0.43	24.7	1.78	0.00	100	68.2	3.53	28.2	70.7	ph	3
01_opx2rim	53.5	0.38	1.01	0.02	18.1	0.49	24.6	1.80	0.00	100	68.2	3.58	28.2	70.8	ph	3
01_opx2outerrim	50.6	0.90	4.35	0.10	6.83	0.06	15.4	21.6	0.22	100	44.3	44.6	11.0	80.0	rx-rim	3
01_opx4core	54.0	0.27	0.66	0.01	17.9	0.68	25.0	1.47	0.00	100	69.2	2.93	27.8	71.3	mph	4
01_opx4rim	53.5	0.35	1.25	0.00	17.5	0.50	25.3	1.62	0.00	100	69.8	3.20	27.0	72.1	mph	4
01_clot4pyx1	53.6	0.34	1.08	0.00	17.9	0.43	25.0	1.59	0.00	100	69.1	3.15	27.7	71.4	clot	4
01_clot4pyx2	53.9	0.36	1.11	0.00	17.8	0.43	24.8	1.61	0.00	100	69.1	3.23	27.7	71.4	clot	4
01_clot4pyx3	53.7	0.37	0.98	0.00	17.9	0.47	24.8	1.78	0.00	100	68.7	3.55	27.8	71.2	clot	4
04_opx1core	54.4	0.26	0.88	0.00	17.8	0.44	24.6	1.71	0.00	100	68.7	3.44	27.8	71.2	ph	3
04_opx1mid	52.5	0.41	1.48	0.01	10.8	0.31	15.3	18.8	0.29	100	43.9	38.8	17.3	71.7	rx-rim	3
04_opx1rim	51.9	0.71	2.60	0.04	8.63	0.26	15.4	20.2	0.30	100	44.2	41.8	13.9	76.0	rx-rim	3
04_clot2opx1	54.0	0.37	1.49	0.00	16.7	0.48	25.3	1.66	0.00	100	70.5	3.33	26.1	73.0	clot	2
04_clot3pyx1	53.7	0.40	1.89	0.05	15.8	0.43	26.2	1.57	0.00	100	72.4	3.12	24.4	74.8	clot	2
04_clot3pyx3	53.4	0.41	1.82	0.02	16.9	0.50	25.2	1.70	0.00	100	70.2	3.41	26.4	72.7	clot	2
04_clot4pyx2	53.5	0.41	0.97	0.01	19.3	0.50	23.5	1.81	0.00	100	65.9	3.65	30.5	68.4	clot	4
04_clot5pyx1	54.1	0.30	0.87	0.01	17.9	0.43	24.5	1.80	0.00	100	68.4	3.61	28.0	70.9	clot	4
04_clot5pyx2	53.8	0.34	0.89	0.00	18.5	0.45	24.2	1.86	0.00	100	67.3	3.73	28.9	70.0	clot	4
04_clot5pyx3	54.1	0.35	0.85	0.01	17.6	0.38	24.8	1.83	0.00	100	69.0	3.65	27.4	71.6	clot	4
04_opx2core	53.1	0.38	1.73	0.03	16.6	0.44	26.0	1.66	0.06	100	71.3	3.26	25.5	73.7	mph	2
04_opx2rim	53.6	0.41	1.42	0.01	16.0	0.44	26.5	1.59	0.00	100	72.4	3.12	24.5	74.7	mph	2
04_opx3core	53.3	0.38	0.89	0.00	19.5	0.48	23.5	1.89	0.00	100	65.7	3.79	30.5	68.3	mph	4
04_opx3rim	53.7	0.41	0.97	0.01	18.5	0.48	24.1	1.85	0.01	100	67.3	3.71	29.0	69.9	mph	4

Abbreviations include: orthopyroxene (opx), pyroxene (pyx), phenocryst (ph), microphenocryst (mph), crystal clot (clot), middle (mid), reaction (rx)

Table 4. Orthopyroxene compositions (cont.)

Orthopyroxene

Label	SiO_2	TiO_2	Al_2O_3	Cr_2O_3	FeO*	MnO	MgO	CaO	Na_2O	Total	En	Wo	Fs	Mg#	Type	Population #
andesite of Coleman Pinnacle *(acp)*																
20_clot2pyx2	53.1	0.28	0.71	0.01	21.8	0.71	21.9	1.53	0.00	100	62.2	3.13	34.7	64.2	clot	1
20_clot2pyx3	52.5	0.29	0.76	0.01	21.7	0.70	22.7	1.43	0.00	100	63.3	2.86	33.9	65.1	clot	1
20_opx2core	53.0	0.21	0.43	0.03	22.1	0.87	22.1	1.26	0.00	100	62.4	2.56	35.1	64.0	mph	1
20_opx2rim	49.5	1.06	4.58	0.03	8.22	0.11	13.3	22.7	0.43	100	38.9	47.7	13.5	74.3	rx-rim	1
20_opx1core	53.0	0.31	0.93	0.02	20.0	0.51	23.7	1.58	0.00	100	65.8	3.15	31.1	67.9	ph	1
20_opx1mid	53.3	0.34	0.90	0.01	19.7	0.53	23.6	1.63	0.00	100	66.0	3.26	30.8	68.2	ph	1
20_opx1rim	50.4	0.92	3.85	0.01	7.84	0.16	13.8	22.5	0.47	100	40.1	47.1	12.8	75.8	rx-rim	1
20_clot4opx1	53.0	0.24	0.64	0.00	21.1	0.79	23.1	1.24	0.00	100	64.5	2.50	33.0	66.1	clot	

Abbreviations include: orthopyroxene (opx), pyroxene (pyx), phenocryst (ph), microphenocryst (mph), crystal clot (clot), middle (mid), reaction (rx)

Table 5. Olivine compositions

Olivine

Label	SiO_2	Cr_2O_3	FeO*	MnO	NiO	MgO	CaO	Total	Fo	Type	Population #
andesite of Swift Creek *(asw)*											
31_olv1core	39.6	0.05	14.5	0.18	0.15	45.4	0.19	100	84.8	ph	1
31_olv1rim	39.8	0.05	13.9	0.17	0.17	45.6	0.21	100	85.4	ph	1
31_olv2core	39.9	0.03	13.8	0.21	0.15	45.8	0.18	100	85.5	ph	1
31_olv2rim	39.0	0.04	16.3	0.25	0.13	44.2	0.16	100	82.9	ph	1
31_olv3core	40.0	0.02	13.5	0.16	0.15	45.9	0.18	100	85.8	ph	1
31_olv3rim	38.3	0.04	20.7	0.28	0.14	40.3	0.17	100	77.6	ph	1
35_olv3core	39.9	0.05	14.0	0.18	0.18	45.5	0.18	100	85.2	ph	1
35_olv3mid	39.8	0.04	14.1	0.20	0.14	45.6	0.18	100	85.2	ph	1
35_olv3rim	37.6	0.07	26.2	0.44	0.15	35.3	0.21	100	70.6	ph	1
35_olv4core	40.1	0.05	14.5	0.21	0.11	44.8	0.17	100	84.7	ph	1
35_olv4mid	38.1	0.04	22.0	0.29	0.16	39.2	0.19	100	76.0	ph	1
35_olv4rim	37.6	0.05	27.1	0.45	0.15	34.5	0.20	100	69.4	ph	1
35_clot1olv1	39.5	0.04	14.1	0.15	0.28	45.9	0.15	100	85.3	clot	1

Abbreviations include: olivine (olv), phenocryst (ph), crystal clot (clot), middle (mid)

Table 5. Olivine compositions (cont.)

Olivine

Label	SiO_2	Cr_2O_3	FeO*	MnO	NiO	MgO	CaO	Total	Fo	Type	Population #
andesite of Dobbs Creek *(ado)*											
11_olv2core	37.5	0.06	25.5	0.38	0.24	36.2	0.15	100	71.7	ph	1
11_olv2rim	37.3	0.06	28.0	0.46	0.13	34.0	0.16	100	68.4	ph	1
11_olv3core	37.2	0.05	29.1	0.48	0.17	32.9	0.19	100	66.9	ph	2
11_olv3rim	37.0	0.05	29.3	0.48	0.16	32.8	0.17	100	66.6	ph	2
11_olv4core	37.1	0.04	28.8	0.48	0.19	33.2	0.19	100	67.3	ph	2
11_olv4rim	37.3	0.06	29.0	0.45	0.15	32.9	0.16	100	66.9	ph	2
14_olv1core	37.3	0.06	28.0	0.46	0.19	33.8	0.18	100	68.2	ph	2
14_olv1rim	37.2	0.05	29.0	0.50	0.20	32.9	0.15	100	66.9	ph	2
14_olv2core	37.2	0.06	28.0	0.44	0.17	33.9	0.20	100	68.3	ph	2
14_olv4core	36.9	0.03	29.3	0.50	0.19	32.9	0.20	100	66.7	ph	2
14_olv4rim	36.8	0.05	29.6	0.50	0.16	32.8	0.15	100	66.4	ph	2

Abbreviations include: olivine (olv), phenocryst (ph), crystal clot (clot), middle (mid)

Table 5. Olivine compositions (cont.)

Olivine

Label	SiO_2	Cr_2O_3	FeO*	MnO	NiO	MgO	CaO	Total	Fo	Type	Population #
andesite of Dobbs Cleaver *(adb)*											
01_olv1core	40.1	0.02	11.9	0.09	0.34	47.4	0.12	100	87.7	ph	1
01_olv1rim	39.5	0.02	16.5	0.21	0.14	43.5	0.14	100	82.5	ph	1
01_olv4core	39.9	0.03	13.5	0.18	0.30	46.0	0.14	100	85.9	ph	2
01_olv4mid	39.5	0.03	16.1	0.21	0.29	43.8	0.11	100	82.9	ph	2
01_olv4rim	37.9	0.03	22.6	0.33	0.22	38.7	0.12	100	75.3	ph	2
01_olv5core	39.7	0.03	15.1	0.20	0.25	44.7	0.09	100	84.1	ph	2
01_olv5rim	37.7	0.05	24.9	0.41	0.18	36.6	0.13	100	72.4	ph	2
04_olv1core	39.4	0.05	15.2	0.23	0.29	44.6	0.14	100	83.9	ph	2
04_olv1rim	37.0	0.05	27.3	0.48	0.16	35.0	0.14	100	69.6	ph	2
04_olv2core	37.8	0.04	26.0	0.44	0.07	35.5	0.16	100	70.8	ph	4
04_olv2rim	37.0	0.04	29.4	0.57	0.07	32.7	0.16	100	66.5	ph	4
04_olv3core	39.5	0.04	15.3	0.19	0.31	44.6	0.10	100	83.8	ph	2
04_olv3rim	36.8	0.13	29.7	0.53	0.16	32.5	0.16	100	66.1	ph	2
04_olv4core	38.1	0.03	21.7	0.35	0.15	39.5	0.12	100	76.4	ph	3
04_olv4rim	36.4	0.06	28.5	0.53	0.12	34.2	0.15	100	68.2	ph	3
04_clot3olv1	38.3	0.05	18.7	0.25	0.30	42.4	0.09	100	80.2	clot	3

Abbreviations include: olivine (olv), phenocryst (ph), crystal clot (clot), middle (mid)

Table 6. Fe-Ti oxide compositions

Ferrian Ilmenite

Label	SiO_2	TiO_2	Al_2O_3	Cr_2O_3	V_2O_3	FeO*	MnO	NiO	MgO	ZnO	Total	Type
andesite of Swift Creek (*asw*)												
31_ilm1	0.17	47.5	0.05	0.02	2.17	48.0	0.51	0.01	0.81	0.00	99.3	ph
31_ilm2	0.19	48.3	0.06	0.02	2.80	47.2	0.46	0.03	1.01	0.00	100.0	ph
31_ilm3	0.64	47.5	0.25	0.04	2.58	47.0	0.52	0.00	1.19	0.04	99.8	ph
35_ilm1	0.21	48.8	0.09	0.02	1.66	45.8	0.54	0.00	1.85	0.01	99.0	ph
35_ilm2	0.16	49.5	0.12	0.02	2.19	45.9	0.55	0.00	2.38	0.05	100.9	ph
andesite of Dobbs Creek (*ado*)												
14_ilm2	0.03	49.9	0.03	0.03	2.46	45.6	0.47	0.01	1.68	0.05	100.2	ph
14_ilm3	0.00	48.4	0.09	0.02	1.63	47.0	0.61	0.01	1.71	0.00	99.5	ph (exs)
andesite of Dobbs Cleaver (*adb*)												
01_ilm1	0.35	47.8	0.06	0.00	1.20	47.0	0.55	0.00	0.50	0.00	97.5	ph
04_ilm1	0.23	48.9	0.03	0.01	1.93	47.3	0.56	0.00	0.40	0.06	99.4	ph
04_ilm2	0.33	47.3	0.11	0.01	2.45	47.1	0.49	0.00	0.61	0.07	98.4	ph
andesite of Coleman Pinnacle (*acp*)												
20_ilm1	0.04	26.9	0.46	0.01	1.99	62.7	0.36	0.04	2.85	0.04	95.3	ph (exs)
20_ilm2	0.05	19.9	0.55	0.02	1.85	69.3	0.29	0.00	1.90	0.01	93.8	ph (exs)

Abbreviations include: ilmenite (ilm), phenocryst (ph), exsolved (exs)

Table 6. Fe-Ti oxide compositions (cont.)

Magnetite

Label	SiO_2	TiO_2	Al_2O_3	Cr_2O_3	V_2O_3	FeO*	MnO	NiO	MgO	ZnO	Total	Type
andesite of Swift Creek (*asw*)												
31_mag1	0.11	17.3	2.79	0.51	4.10	72.2	0.39	0.06	1.48	0.07	99.0	ph
31_mag2	0.10	20.7	1.14	0.03	3.06	71.7	0.43	0.01	1.01	0.10	98.4	ph
31_mag3	0.28	21.3	1.60	0.04	3.83	71.5	0.48	0.03	1.35	0.15	100.5	ph
35_mag3	0.12	22.9	1.25	0.05	2.84	69.6	0.54	0.02	1.54	0.11	99.0	ph
andesite of Dobbs Creek (*ado*)												
11_mag1	0.07	10.2	1.37	0.56	4.98	80.3	0.27	0.08	0.44	0.13	98.4	ph (exs)
11_mag2	0.07	14.9	2.02	0.13	4.73	75.2	0.19	0.05	0.38	0.08	97.8	ph
11_mag3	0.07	7.05	6.42	0.14	2.44	78.8	0.41	0.04	0.48	0.13	96.0	ph
11_clot3ox	0.05	14.4	2.95	0.39	3.34	74.0	0.38	0.06	2.49	0.10	98.2	ph (clot)
14_mag1	0.30	18.0	2.13	0.36	5.09	67.7	0.41	0.05	2.14	0.10	96.3	ph
14_mag4b	0.05	16.9	2.35	0.23	4.04	71.6	0.39	0.05	2.99	0.12	98.7	ph (exs)
andesite of Dobbs Cleaver (*adb*)												
01_mag1	0.10	14.5	2.86	0.07	2.89	75.4	0.44	0.00	2.53	0.10	98.8	ph
01_mag2	0.19	19.8	0.90	0.06	3.78	72.1	0.57	0.03	0.88	0.08	98.4	ph
01_mag3	0.09	15.4	2.68	0.02	3.10	74.6	0.45	0.02	2.59	0.07	99.0	ph
04_mag1	0.09	16.0	2.07	0.15	3.07	74.7	0.50	0.02	0.62	0.04	97.2	ph
04_mag2	0.04	16.5	1.09	0.01	3.15	75.3	0.49	0.03	0.44	0.14	97.3	ph
04_mag3	0.33	18.1	0.63	0.02	2.42	72.2	0.67	0.05	0.40	0.16	94.9	ph
04_mag4	0.10	15.6	1.99	0.05	2.95	77.0	0.55	0.02	0.55	0.14	98.9	ph
andesite of Coleman Pinnacle (*acp*)												
20_mag1	0.05	4.06	2.79	0.04	1.57	83.6	0.85	0.04	3.27	0.25	96.6	ph (exs)
20_mag2	0.06	1.61	3.25	0.02	1.77	85.1	1.00	0.06	3.08	0.28	96.3	ph (exs)
20_mag3	0.03	0.25	9.78	0.04	0.15	63.7	4.62	0.15	13.61	1.25	93.6	ph
20_mag4	0.01	6.32	1.53	0.02	1.79	80.6	0.50	0.00	1.58	0.00	92.4	ph
20_mag5	0.05	2.55	1.35	0.01	1.43	84.3	0.77	0.05	2.73	0.29	93.6	ph
20_maginc	0.03	6.17	1.53	0.02	2.16	81.6	0.24	0.00	0.62	0.01	92.3	inc

Abbreviations include: magnetite (mag), phenocryst (ph), exsolved (exs)

Table 6. Fe-Ti oxide compositions (cont.)

Chromium Spinel

Label	SiO_2	TiO_2	Al_2O_3	Cr_2O_3	V_2O_3	FeO*	MnO	NiO	MgO	ZnO	Total	Type
andesite of Swift Creek (*asw*)												
31_clot1ox	0.08	17.2	3.71	2.93	3.77	69.1	0.38	0.06	3.52	0.06	100.8	ph (clot)
35_chr1	0.06	15.1	2.19	11.1	3.44	63.9	0.39	0.03	1.93	0.10	98.3	ph
35_chr2	0.08	19.3	1.69	4.66	3.59	67.7	0.48	0.03	1.85	0.11	99.5	ph
35_ox2inc	0.39	15.2	5.57	11.6	3.66	59.0	0.38	0.11	3.89	0.03	99.9	inc
andesite of Dobbs Creek (*ado*)												
14_chr1	0.20	14.6	2.96	7.48	3.10	64.1	0.42	0.07	2.69	0.08	95.7	inc
andesite of Dobbs Cleaver (*adb*)												
01_chr1	0.09	13.7	3.20	3.53	3.76	72.9	0.43	0.05	2.50	0.04	100.2	ph
01_chr2	0.08	0.85	16.5	39.3	0.59	31.0	0.35	0.11	9.44	0.14	98.3	inc
04_chr1	0.06	0.65	15.0	37.1	0.65	36.2	0.34	0.14	6.03	0.27	96.4	inc
04_clot3oxinc	0.06	12.1	4.56	2.08	2.24	71.9	0.37	0.17	2.81	0.06	96.4	inc (clot)

Abbreviations include: oxide (ox), chromium spinel (chr), phenocryst (ph), exsolved (exs)

Table 7. Hornblende compositions

Hornblende

Label	SiO_2	TiO_2	Al_2O_3	FeO*	MnO	MgO	CaO	Na_2O	K_2O	Total	Mg#	Type
andesite of Coleman Pinnacle *(acp)*												
20_hbl1core	44.1	2.26	11.7	9.37	0.07	16.5	12.1	2.59	1.27	100	75.9	ph
20_hbl1rim	43.6	2.48	11.7	10.0	0.14	16.3	12.0	2.53	1.22	100	74.4	ph
20_hbl2core	44.3	2.21	12.2	8.92	0.09	16.5	12.0	2.48	1.34	100	76.8	ph
20_hbl2rim	43.3	2.68	11.7	10.3	0.08	16.0	12.2	2.56	1.11	100	73.5	ph
20_hbl4core	42.6	2.86	12.0	11.1	0.11	15.5	12.3	2.59	0.99	100	71.3	ph
20_hbl4rim	43.2	4.47	11.4	8.46	0.21	16.4	12.2	2.60	1.09	100	77.5	ph

Abbreviations include: hornblende (hbl), phenocryst (ph)

Table 8. Crystal clot types with sizes and compositions

Crystal clots

Label	Population	Clots	Olivine (Fo)	Augite (Mg#)	Orthopyroxene (Mg#)	Plagioclase (An)	Size (diameter)
asw	A	31-clot1	85	82	75	65	5 mm
		31-clot2	-	78-83	-	60	4.75 mm
		31-clot3	-	83	76-79	64	3 mm
		35-clot1	85	79	77	57	3.75 mm
		35-clot2	-	81	-	66	3.25 mm
		35-clot3	-	-	74-79	69	1.5 mm
	B	31-clot6	-	81-82	-	65	0.9 mm
adb	A	01-clot4	-	-	71	-	1.2 mm
		04-clot4	-	71-72	68	-	1.5 mm
		04-clot5	-	-	70-72	54	1.25 mm
	B	04-clot2	-	76	73	57	1 mm
	C	04-clot3	80	-	73-75	-	1 mm
	D	04-clot1	-	75-77	-	60-61	4 mm
acp	A	20-clot1	-	70-71	-	46	2.1 mm
		20-clot2	-	72	64-65	-	1.2 mm
	B	20-clot3	-	79-82	-	-	<0.5 mm
		20-clot4	-	76-77	66	59	1.25 mm

Table 9. Whole rock major, minor and trace element data. Sample locations are reported in latitude and longitude.

Unit	**andesite of Swift Creek (*asw*)**				
Sample	**asw-30**	**asw-31**	**asw-33**	**asw-34**	**asw-35**
Latitude	48.48109	48.48113	48.70739	48.70739	48.79918
Longitude	-121.41207	-121.41197	-121.68775	-121.68775	-121.68864
	Major element oxides (wt.%) analyzed by XRF				
SiO_2	56.0	56.2	55.9	55.9	56.0
TiO_2	1.02	1.02	1.03	1.04	1.02
Al_2O_3	16.8	16.9	16.9	16.8	16.7
CaO	7.85	7.67	7.92	8.14	7.77
Na_2O	3.72	3.84	3.75	3.65	3.71
K_2O	1.16	1.28	1.12	0.97	1.15
P_2O_5	0.24	0.25	0.24	0.24	0.24
Total	100	100	100	100	100
Mg#	59.8	59.5	60.3	60.2	60.7
	Trace elements (ppm) analyzed by XRF				
Ni	60	60	60	60	67
Cr	182	184	191	191	203
V	140	138	140	139	142
Cu	33	37	30	25	31
Zn	68	67	70	69	70
	Trace elements (ppm) analyzed by ICP-MS				
La	17.3	17.1	17.7	17.4	17.5
Ce	38.3	37.9	38.8	38.4	38.6
Pr	4.94	4.89	5.03	4.96	4.95
Eu	1.35	1.36	1.36	1.38	1.35
Gd	4.13	4.14	4.18	4.20	4.15
Tb	0.70	0.69	0.69	0.68	0.70
Dy	4.32	4.25	4.37	4.34	4.28
Ho	0.92	0.90	0.92	0.91	0.91
Er	2.50	2.46	2.54	2.49	2.51
Tm	0.36	0.36	0.37	0.36	0.37
Yb	2.33	2.35	2.34	2.34	2.35
Lu	0.37	0.37	0.37	0.38	0.37
Ba	409	392	405	379	397
Th	2.91	2.83	2.99	2.93	2.84
Nb	5.75	5.86	5.82	5.85	5.79
U	1.12	1.10	1.14	1.11	1.10
Pb	4.65	4.65	4.65	4.61	4.66
Rb	22.2	19.3	30.5	23.0	29.0

Table 9. Whole rock major, minor and trace element data. Sample locations are reported in latitude and longitude (cont.)

Cs	4.28	3.83	6.55	6.82	6.56
Sr	710	708	735	724	716
Sc	22.2	22.3	22.4	22.5	22.3
Zr	160	158	161	158	161

Table 9. Whole rock major, minor and trace element data. Sample locations are reported in latitude and longitude (contd.)

Unit	**andesite of Dobbs Creek (*ado*)**				
Sample	**ado-10**	**ado-11**	**ado-12**	**ado-13**	**ado-14**
Latitude	48.85389	48.85386	48.85335	48.85325	48.85331
Longitude	-121.80048	-121.80032	-121.80047	-121.80029	-121.80029
	Major element oxides (wt.%) analyzed by XRF				
SiO_2	56.6	56.9	56.4	56.5	56.3
TiO_2	1.01	0.99	0.99	1.01	1.02
Al_2O_3	17.0	17.0	17.0	16.9	16.9
CaO	7.72	7.58	7.75	7.77	7.80
Na_2O	3.76	3.76	3.69	3.72	3.66
K_2O	1.35	1.40	1.32	1.32	1.30
P_2O_5	0.26	0.26	0.25	0.26	0.26
Total	100	100	100	100	100
Mg#	57.8	58.0	57.4	57.8	57.7
	Trace elements (ppm) analyzed by XRF				
Ni	57.5	57.5	60.4	58.1	61.2
Cr	128	137	137	135	139
V	181	175	181	179	181
Cu	23.6	18.8	36.4	24.3	55.1
Zn	73.2	72.3	74.5	75.5	72.8
	Trace elements (ppm) analyzed by ICP-MS				
La	15.7	15.9	15.6	16.0	15.6
Ce	35.0	35.4	34.7	35.7	35.0
Pr	4.62	4.65	4.56	4.75	4.64
Eu	1.27	1.33	1.29	1.26	1.30
Gd	4.07	4.02	3.90	4.06	3.99
Tb	0.64	0.65	0.63	0.65	0.64
Dy	3.93	3.95	3.87	3.96	3.93
Ho	0.80	0.80	0.78	0.81	0.81
Er	2.16	2.15	2.13	2.22	2.20
Tm	0.32	0.31	0.31	0.33	0.31
Yb	1.99	2.00	1.96	1.98	2.01
Lu	0.32	0.31	0.31	0.32	0.31
Ba	389	388	391	394	382
Th	3.44	3.39	3.40	3.49	3.38
Nb	4.97	4.95	4.94	5.03	4.98
U	1.24	1.22	1.22	1.26	1.21
Pb	4.75	4.03	4.34	4.86	4.84
Rb	19.8	19.8	19.7	20.4	19.3

Table 9. Whole rock major, minor and trace element data. Sample locations are reported in latitude and longitude (contd.)

Cs	0.27	0.35	0.26	0.33	0.28
Sr	825	841	832	821	824
Sc	21.3	21.6	20.9	21.1	21.7
Zr	150	149	148	153	148

Table 9. Whole rock major, minor and trace element data. Sample locations are reported in latitude and longitude (contd.)

Unit	**andesite of Dobbs Cleaver (*adb*)**						
Sample	**adb-01**	**adb-02**	**adb-04**	**adb-05**	**adb-06**	**adb-07**	**adb-08**
Latitude	48.8697	48.86849	48.86815	48.86811	48.86678	48.8664	48.87101
Longitude	-121.79219	-121.79218	-121.7923	-121.79339	-121.79494	-121.79365	-121.78744
Major element oxides (wt.%) analyzed by XRF							
SiO_2	58.6	59.4	59.5	59.2	59.3	59.1	59.4
TiO_2	1.08	1.07	1.07	1.06	1.06	1.07	1.08
Al_2O_3	17.1	16.7	16.8	16.7	16.8	17.0	16.8
CaO	6.31	6.01	6.04	6.21	6.10	6.25	6.10
Na_2O	4.17	4.38	4.38	4.36	4.37	4.36	4.45
K_2O	1.78	1.87	1.87	1.83	1.86	1.82	1.89
P_2O_5	0.30	0.30	0.30	0.30	0.30	0.30	0.30
Total	100	100	100	100	100	100	100
Mg#	52.4	50.7	49.9	50.7	50.2	50.9	49.5
Trace elements (ppm) analyzed by XRF							
Ni	44.1	32.6	32.0	33.1	31.4	32.2	29.5
Cr	89.8	66.6	64.9	65.5	62.3	66.4	56.7
V	168	151	148	147	188	150	145
Cu	27.8	26.2	36.2	22.2	27.9	30.3	26.7
Zn	89.8	74.6	76.9	76.7	76.9	77.2	77.5
Trace elements (ppm) analyzed by ICP-MS							
La	19.2	19.5	19.4	19.2	19.1	19.6	19.8
Ce	41.9	43.4	42.5	41.9	42.2	42.6	42.9
Pr	5.62	5.71	5.62	5.54	5.58	5.64	5.62
Eu	1.50	1.49	1.48	1.46	1.48	1.48	1.47
Gd	5.08	5.10	5.07	5.04	5.03	5.16	5.19
Tb	0.84	0.83	0.84	0.83	0.82	0.84	0.84
Dy	5.06	5.10	5.06	5.04	5.05	5.14	5.16
Ho	1.02	1.04	1.04	1.03	1.03	1.04	1.07
Er	2.81	2.86	2.87	2.81	2.80	2.82	2.95
Tm	0.42	0.42	0.42	0.41	0.41	0.42	0.43
Yb	2.62	2.66	2.63	2.60	2.60	2.62	2.69
Lu	0.42	0.41	0.42	0.41	0.42	0.41	0.41
Ba	552	539	534	526	532	534	544
Th	4.52	4.51	4.44	4.42	4.45	4.50	4.59
Nb	7.27	7.28	7.27	7.03	7.27	7.11	7.41
U	1.74	1.74	1.74	1.74	1.75	1.72	1.81
Pb	6.67	5.71	4.91	6.68	5.36	6.48	6.02
Rb	28.4	31.0	32.2	30.1	30.2	26.5	31.2

Table 9. Whole rock major, minor and trace element data. Sample locations are reported in latitude and longitude (contd.)

Cs	0.74	0.49	0.53	0.58	0.35	0.63	0.54
Sr	670	645	649	659	651	664	641
Sc	18.9	18.7	18.3	18.6	18.7	18.2	18.3
Zr	201	201	198	194	201	196	202

Table 9. Whole rock major, minor and trace element data. Sample locations are reported in latitude and longitude (contd.)

Unit	**andesite of Coleman Pinnacle (*acp*)**					
Sample	**acp-20**	**acp-21**	**acp-22**	**acp-23**	**acp-24**	**acp-26**
Latitude	48.82095	48.82031	48.82213	48.82316	48.82502	48.83968
Longitude	-121.74055	-121.74142	-121.73672	-121.73396	-121.72859	-121.7212
	Major element oxides (wt.%) analyzed by XRF					
SiO_2	57.7	60.1	61.2	64.8	60.0	64.2
TiO_2	1.06	0.97	0.93	0.74	0.97	0.76
Al_2O_3	17.0	16.8	17.0	16.8	16.9	16.9
CaO	6.72	5.79	5.26	3.77	5.78	4.15
Na_2O	4.98	4.88	4.72	4.96	4.91	4.92
K_2O	2.84	2.90	2.81	3.00	2.91	2.87
P_2O_5	0.50	0.41	0.36	0.24	0.41	0.26
Total	100	100	100	100	100	100
Mg#	49.6	47.3	46.3	40.0	46.7	41.4
	Trace elements (ppm) analyzed by XRF					
Ni	23.6	19.3	13.6	3.48	16.3	3.58
Cr	26.4	21.0	14.8	3.38	14.6	4.88
V	154	129	115	76.5	126	86.8
Cu	39.0	33.1	36.3	11.2	37.0	18.0
Zn	107	91.2	56.7	61.5	87.5	67.3
	Trace elements (ppm) analyzed by ICP-MS					
La	39.7	33.8	32.2	30.5	35.3	27.2
Ce	89.4	73.6	68.5	54.6	77.6	57.2
Pr	12.0	9.65	9.16	7.91	10.2	7.11
Eu	2.26	1.84	1.72	1.36	1.89	1.41
Gd	5.90	5.36	5.46	4.86	5.54	4.49
Tb	0.76	0.78	0.82	0.80	0.79	0.72
Dy	3.95	4.37	4.70	4.84	4.28	4.32
Ho	0.73	0.86	0.95	1.02	0.86	0.89
Er	1.92	2.27	2.50	2.77	2.23	2.48
Tm	0.27	0.33	0.38	0.42	0.32	0.38
Yb	1.67	2.13	2.40	2.80	2.11	2.54
Lu	0.25	0.33	0.38	0.46	0.34	0.42
Ba	1000	915	868	909	936	852
Th	5.96	6.07	5.82	7.62	6.16	7.03
Nb	8.93	9.78	9.80	10.16	9.78	9.70
U	2.30	2.42	2.38	2.97	2.52	2.87
Pb	15.1	12.9	10.7	8.52	13.7	9.14
Rb	35.8	42.5	40.1	47.2	37.3	49.8

Table 9. Whole rock major, minor and trace element data. Sample locations are reported in latitude and longitude (contd.)

Cs	0.51	0.48	0.63	0.62	1.37	1.02
Sr	2209	1564	1270	622	1664	704
Sc	13.5	12.6	12.0	7.2	12.2	7.4
Zr	217	241	247	325	241	307

Table 10. Temperatures are calculated from ILMAT 1.30h using the geothermobarometer of Andersen and Lindsley (1985) and QUILF 95 by Andersen and Lindsley (1998).

Unit	Pair	Temp °C
asw-31	mag2 & ilm3	947
asw-31	mag3 & ilm2	919
asw-35	mag1 & ilm1	964
ado-11	mag3 & ilm2	756
adb-01	mag2 & ilm1	856
adb-04	mag2 & ilm2	819
adb-04	mag3 & ilm1	778

abbreviations include: magnetite (mag), ilmenite (ilm)

Table 11. Temperatures and pressures are calculated using the Two-Pyroxene-based Thermometer of Putirka (2008).

Unit	Pyroxene	Sample	Pop. #	Mg#	Type	Location	En	Wo	Fs	Temp °C	Pressure (kbar)
asw	Augite	31_clot3pyx2	2	82.6	clot	core	46.8	43.4	9.82	1000	2.4
	Orthopyroxene	31_clot3pyx1		79.2	clot	core	76.6	3.32	20.1		
	Augite	31_clot1pyx2	2	82.4	clot	core	46.5	43.6	9.92	989	3.1
	Orthopyroxene	31_clot1pyx1		75.5	clot	core	73.2	2.97	23.8		
	Augite	35_clot1pyx1	2	79.5	clot	core	45.9	42.2	11.9	1010	3.7
	Orthopyroxene	35_clot1pyx2		77.2	clot	core	74.8	3.19	22.0		
	Augite	31_aug3core	1	84.9	ph	core	51.4	39.4	9.16	1089	4.5
	Orthopyroxene	35_opx4core		77.4	ph	core	74.8	3.33	21.9		
	Augite	35_aug4core	5	72.0	ph	core	42.2	41.4	16.4	980	6.3
	Orthopyroxene	35_opx1core		64.8	ph	core	62.4	3.64	33.9		
	Augite	35_aug4rim	5	81.1	ph	rim	49.7	38.7	11.6	1048	2.4
	Orthopyroxene	35_opx1rim		73.2	ph	rim	70.1	4.34	25.6		
ado	Augite	11_aug4core	1	83.5	ph	core	46.3	44.5	9.16	966	1.4
	Orthopyroxene	14_opx4core		74.0	ph	core	71.6	3.22	25.2		
	Augite	11_aug4rim	1	83.0	ph	rim	46.3	44.3	9.49	982	1.6
	Orthopyroxene	14_opx4rim		73.8	ph	rim	71.5	3.13	25.4		
	Augite	11_aug3core	4	69.7	ph	core	42.1	39.6	18.3	981	5.2
	Orthopyroxene	11_opx4core		69.3	ph	core	67.3	2.86	29.8		
	Augite	11_aug3rim	4	74.8	ph	rim	43.9	41.3	14.8	980	4.1
	Orthopyroxene	11_opx4rim		69.8	ph	rim	67.5	3.32	29.2		
	Augite	14_clot1pyx1	4	70.9	clot	core	43.6	38.5	17.9	1025	4.4
	Orthopyroxene	14_clot1pyx2		69.1	clot	core	66.5	3.74	29.7		

abbreviations include: crystal clot (clot), pyroxene (pyx), augite (aug), orthopyroxene (opx), phenocryst (ph)

Table 11. Temperatures and pressures are calculated using the Two-Pyroxene-based Thermometer of Putirka (2008) (cont.)

Unit	Pyroxene	Sample	Pop. #	Mg#	Type	Location	En	Wo	Fs	Temp °C	Pressure (kbar)
adb	Augite	04_aug3core	1	81.0	ph	core	45.1	44.3	10.6	969	2.2
	Orthopyroxene	01_opx3core		77.3	ph	core	75.1	2.85	22.0		
	Augite	04_clot2cpx1	2	76.4	clot	core	42.3	44.7	13.0	939	1.3
	Orthopyroxene	04_clot2opx1		73.0	clot	core	70.5	3.33	26.1		
	Augite	04_clot4pyx3	4	71.7	clot	core	43.4	39.5	17.1	1000	4.0
	Orthopyroxene	04_clot4pyx2		68.4	clot	core	65.9	3.65	30.5		
	Augite	01_aug2core	4	71.6	ph	core	43.3	39.5	17.2	1006	4.1
	Orthopyroxene	04_opx3core		68.3	ph	core	65.7	3.79	30.5		
	Augite	01_aug2rim	4	82.4	ph	rim	46.6	43.4	9.98	969	1.4
	Orthopyroxene	04_opx3rim		69.9	ph	rim	67.3	3.71	29.0		
acp	Augite	20_clot2pyx1	3	71.5	clot	core	40.8	42.9	16.2	944	7.9
	Orthopyroxene	20_clot2pyx3		65.1	clot	core	63.3	2.86	33.9		
	Augite	20_aug3core	3	71.3	ph	core	40.9	42.7	16.5	952	5.8
	Orthopyroxene	20_opx1core		67.9	ph	core	65.8	3.15	31.1		
	Augite	20_aug1core	3	69.2	ph	core	39.8	42.4	17.7	937	7.4
	Orthopyroxene	20_opx2core		64.0	ph	core	62.4	2.56	35.1		

abbreviations include: crystal clot (clot), pyroxene (pyx), augite (aug), orthopyroxene (opx), phenocryst (ph)

Table 12. Crystallized assemblages with proposed magmatic compositions for each flow unit.

Unit	**andesite of Swift Creek (*asw*)**				
Proposed Magmatic Composition	***Basalt or High Magnesium Basaltic Andesite (HMBA)***		***Basaltic Andesite***	***Andesite***	***Dacite***
	B1 clots + phenos	B2 clots + phenos	BA1 phenos	A1 phenos	D1 phenos
Olv (Fo)	-	85-87	-	-	-
Aug (Mg#)	$81\text{-}85_{pop1}$	$78\text{-}83_{pop2}$	$79\text{-}82_{pop3}$	75_{pop4}	72_{pop5}
Opx (Mg#)	$77\text{-}79_{pop1}$	$76\text{-}79_{pop2}$	72_{pop3}	68_{pop4}	$65\text{-}68_{pop5}$
Plag (An)	69_{pop1}	$57\text{-}67_{pop2}$	52_{pop3}	46_{pop4}	-

Unit	**andesite of Dobbs Creek (*ado*)**				
Proposed Magmatic Composition	***Basalt or HMBA***	***Basaltic Andesite***	***Andesite***	***Dacite***	
	B1 clots + phenos	BA1 phenos	A1 phenos	D1 clots + phenos	*Unconstrained populations*
Olv (Fo)	-	-	-	-	$72\text{-}74_{pop1}$, $69\text{-}70_{pop2}$
Aug (Mg#)	84_{pop1}	82_{pop2}	75_{pop3}	$70\text{-}73_{pop4}$	
Opx (Mg#)	$72\text{-}74_{pop1}$	-	-	$69\text{-}70_{pop4}$	
Plag (An)	$59\text{-}64_{pop1}$	$54\text{-}59_{pop2}$	$47\text{-}48_{pop3}$	45_{pop4}	

Unit	**andesite of Dobbs Cleaver (*adb*)**				
Proposed Magmatic Composition	***Basalt or HMBA***	***Basaltic Andesite***	***Andesite***	***Dacite***	
	B1 phenos	BA2 clots + phenos	A1 phenos	D1 clots + phenos	*Unconstrained populations*
Olv (Fo)	-	$76\text{-}80_{pop3}$	-	-	88_{pop1}, $84\text{-}86_{pop2}$, 71_{pop4}
Aug (Mg#)	81_{pop1}	$75\text{-}77_{pop2}$	75_{pop3}	$72\text{-}74_{pop4}$	
Opx (Mg#)	77_{pop1}	$73\text{-}75_{pop2}$	$71\text{-}73_{pop3}$	$68\text{-}72_{pop4}$	
Plag (An)	-	$56\text{-}61_{pop1\&2}$	-	$46\text{-}54_{pop3}$	$42\text{-}43_{pop4}$

* Abbreviations: clots = crystal clots, phenos = phenocrysts, pop = population

Table 12. Crystallized assemblages with proposed magmatic compositions for each flow unit (cont.)

Unit	**andesite of Coleman Pinnacle (*acp*)**		
Proposed Magmatic Composition	***Basaltic Andesite***	***Andesite***	***Dacite***
Aug (Mg#)	BA3 clots + phenos $76\text{-}82_{pop1}$	A2 phenos 75_{pop2}	D1 clots + phenos $69\text{-}72_{pop3}$
Opx (Mg#)	64-68		
Plag (An)	$52\text{-}60_{pop1}$	-	46_{pop2}

Unconstrained populations

$42\text{-}45_{pop3}$

* Abbreviations: clots = crystal clots, phenos = phenocrysts, pop = population

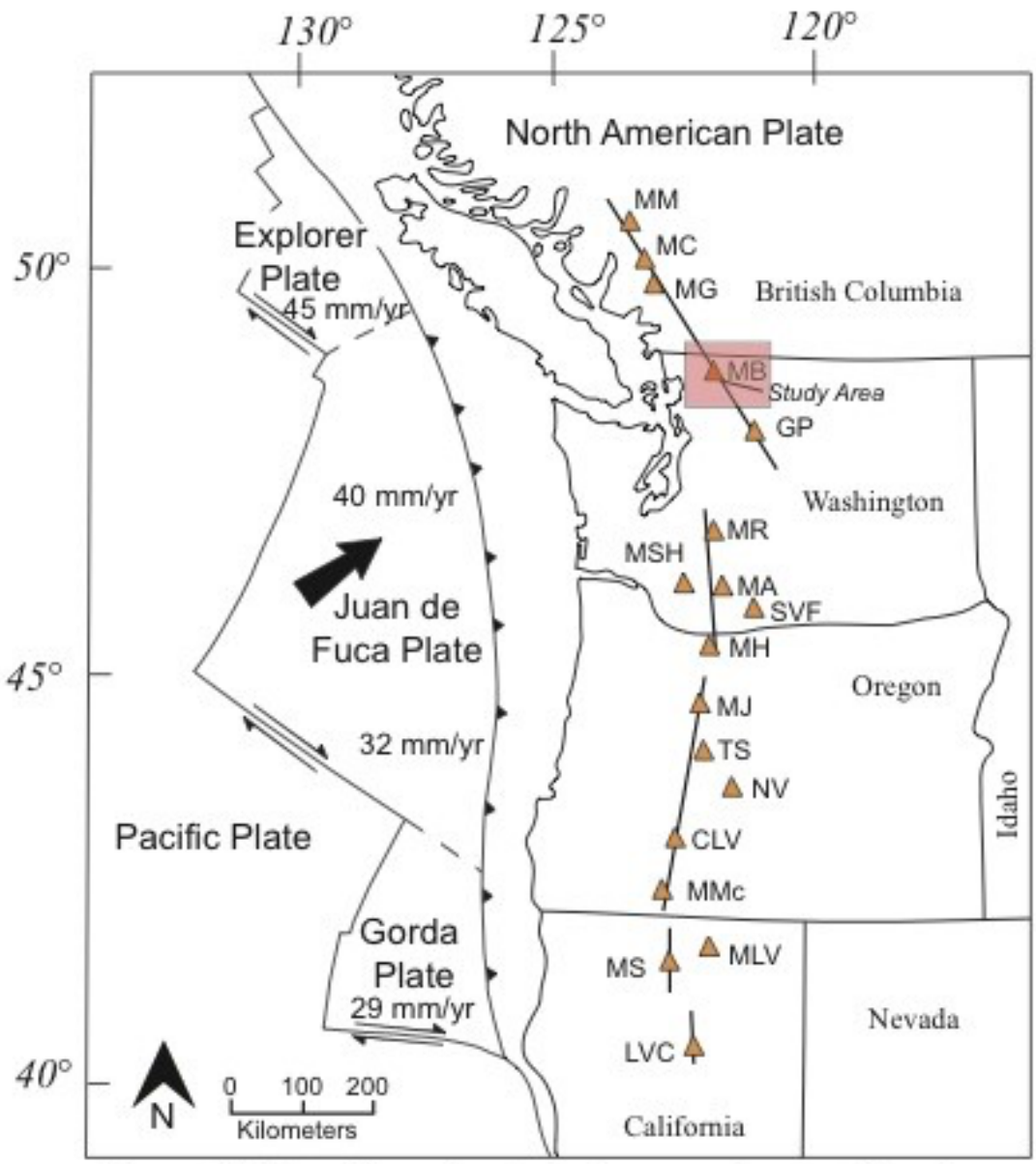

Figure 1. 1300 km Cascadia subduction complex stretching from Lassen Peak Volcanic Center in northern California to Mount Meager in Canada. Black lines indicate segments of the Cascade arc as described by Guffanti and Weaver (1988). Mount Baker volcanic field study area in red is member of the Garibaldi Belt, where a shift in arc trend from N-S to NW-SE begins and mafic output is less. Modified from Borg and Clynne (1998). Subduction rates from McCrory et al. (2004).

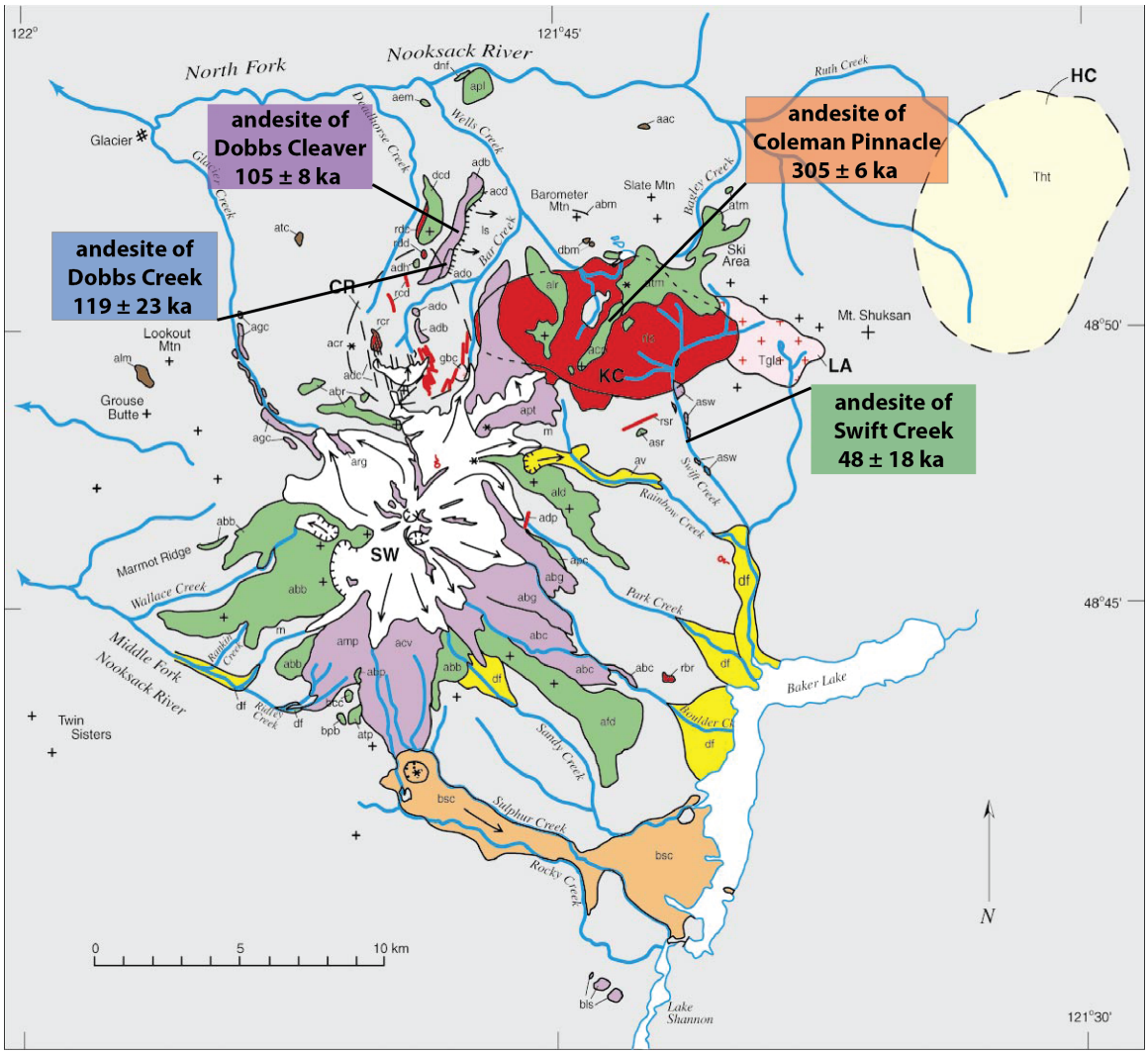

Figure 2. Generalized map showing main lava flow units of the Mount Baker volcanic field and outlying lava remnants (Hildreth et al., 2003). Andesites analyzed in this study are labeled with their age and representative colors (used throughout the study).

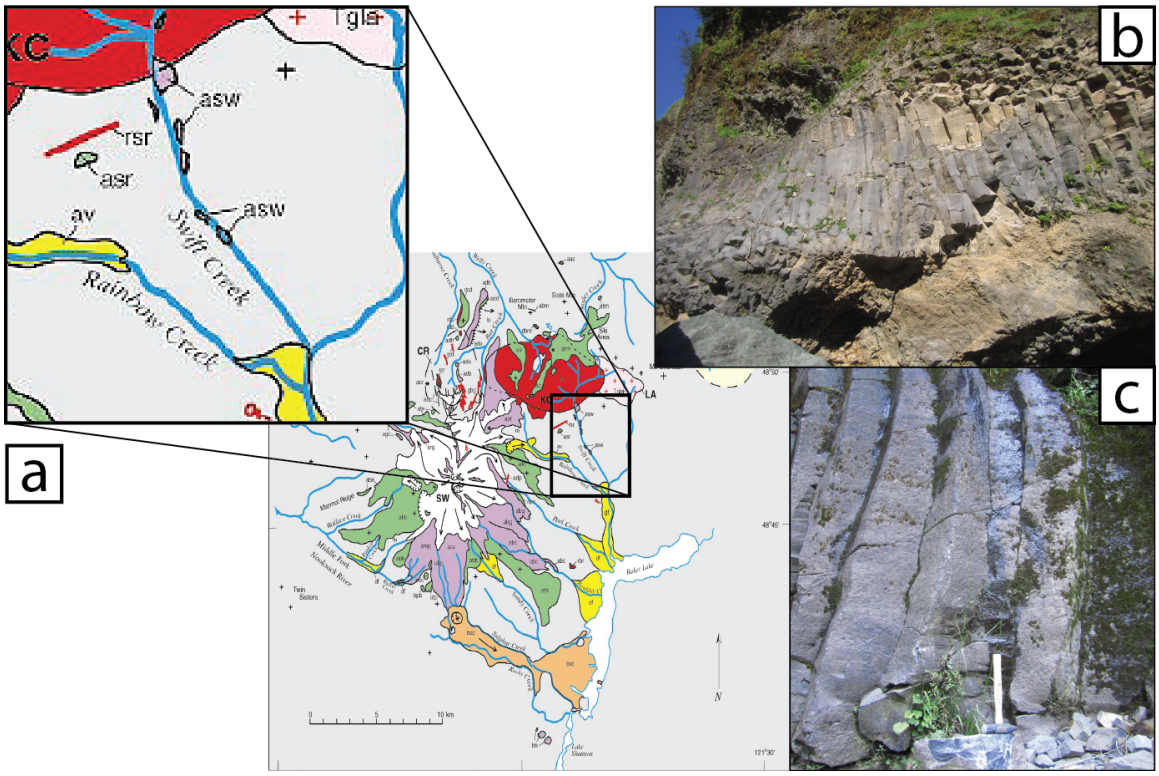

Figure 3. Map and field images of the andesite of Swift Creek (*asw*): a) Geologic map after Hildreth et al. (2003) with close up of dispersed exposures of *asw*. b) Outcrops form steep cliffs on the eastern edge of Swift Creek. c) The *asw* flow unit commonly forms vertical columns that measure up to 9m tall.

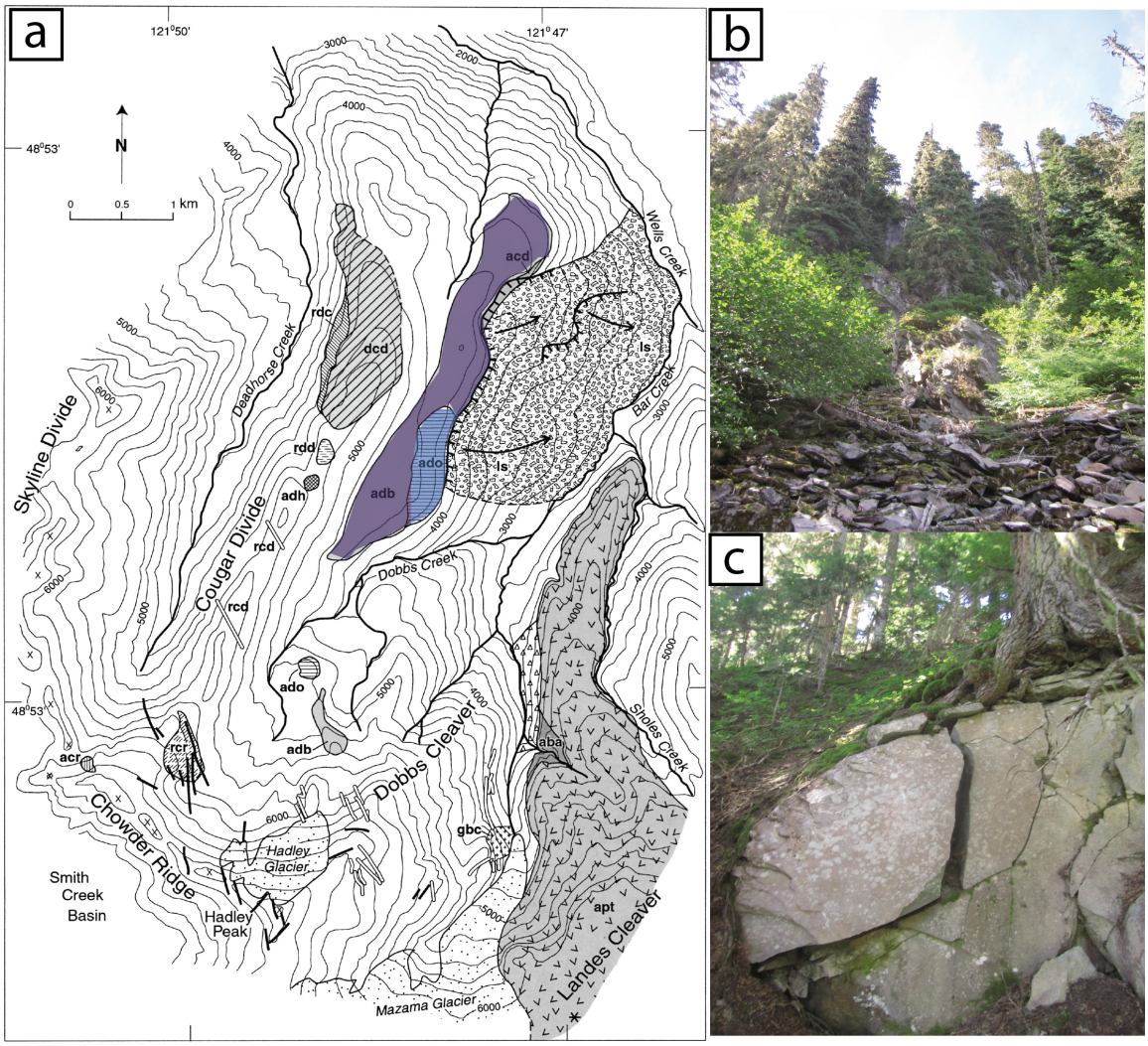

Figure 4. Map and field images of the andesite of Dobbs Cleaver (*adb*) and Dobbs Creek (*ado*): a) Close up map from Figure 3 and modified from Hildreth et al. (2003) with flow units color coded. b) Ascension through forested slopes and loose rubble for access to underlying *ado* flow unit. c) Densely vegetated, scattered outcrops of *adb*.

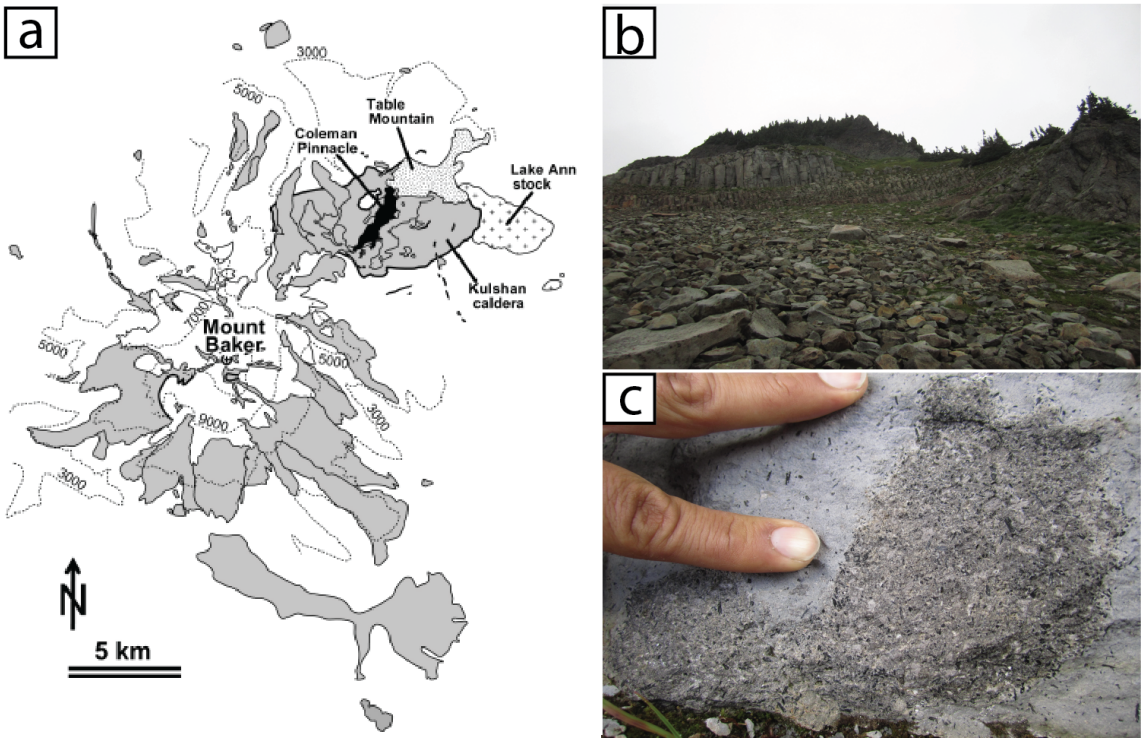

Figure 5. Map and field images of the andesite of Coleman Pinnacle (*acp*): a) Geologic map from Mullen and McCallum (2013) after Hildreth et al. (2003), Tabor et al. (2003), and Tucker (2006). The *acp* flow unit is filled in black. Elevation contours (dotted lines) are given in feet. b) View from Ptarmigan Ridge trail of the notorious exposures of vertical columnar lavas. The top of the *acp* flow unit is commonly capped by dense vegetation. c) Although not common, *acp* is the only flow unit in the study with large inclusions observable in the field.

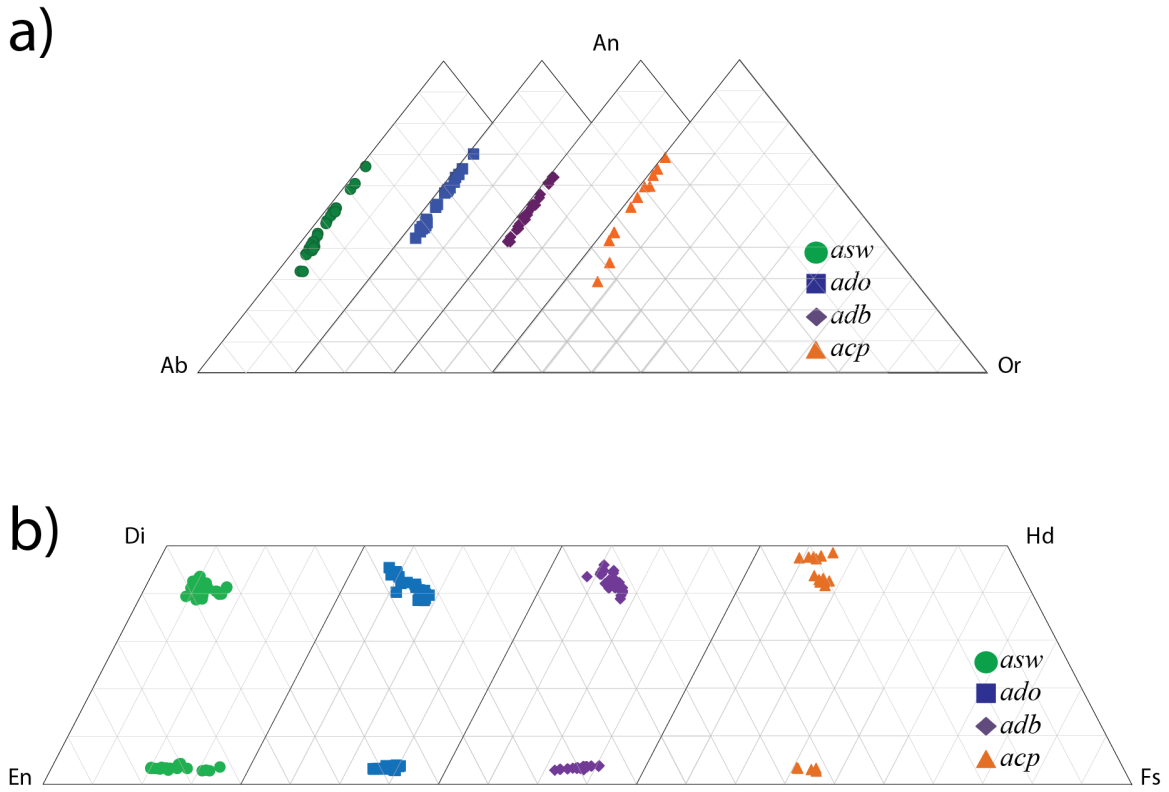

Figure 6. a) Plagioclase feldspar compositions for each flow unit. b) Pyroxene compositions for each flow unit. Abbreviations for flow units are as follows: andesite of Swift Creek (*asw*), andesite of Dobbs Creek (*ado*) andesite of Dobbs Cleaver (*adb*) and andesite of Coleman Pinnacle (*acp*). Abbreviations for compositions are as follows: Ab = albite, An = anorthite, Or = orthoclase, Di = diopside, Hd = hedenbergite, En = enstatite and Fs = ferrosilite.

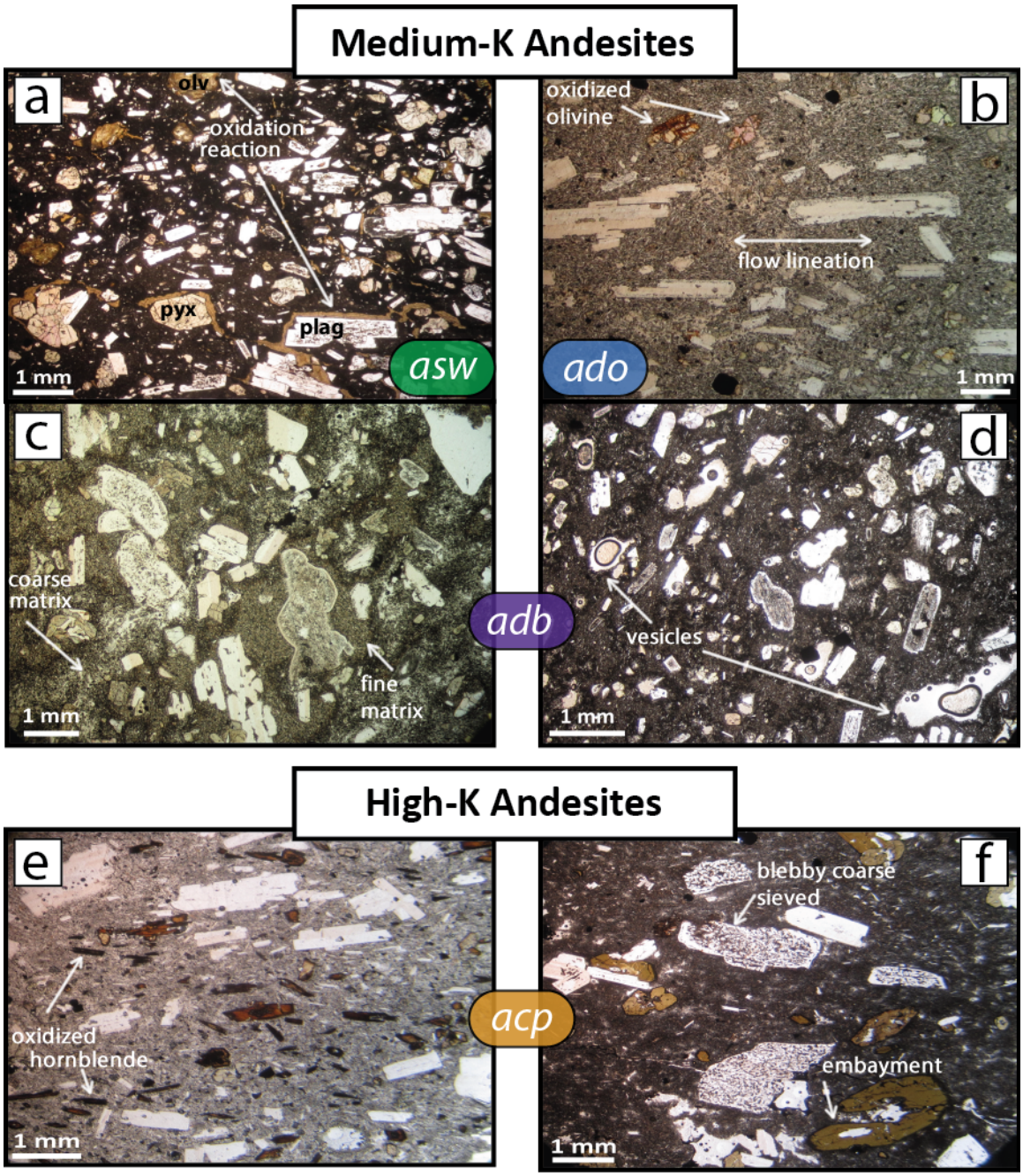

Figure 7. Notable features of each flow unit in thin section. a) All samples of *asw* contain oxidation reaction textures along the edges of all mineral phases. In many cases, olivine is completely replaced by the oxidation reaction. b) The flow unit of *ado* is characterized as having strong phenocryst flow lineation and obvious oxidized fractures in olivine crystals. c) Although very uncommon, evidence of microscopic magma mingling exists in *adb*-07 with coarse grained (light) and fine grained (dark) sections of groundmass. d) *adb*-01, collected on the margin of the flow unit, is the only sample from *adb* with vesicles. e) Andesitic samples of *acp* have heavily oxidized hornblende and generally display flow lineation as well. f) Dacitic samples of *acp* contain hornblende that is less oxidized but commonly displays embayments. Also, blebby coarse-sieved plagioclase is the most unique mineral texture of the dacites of *acp*.

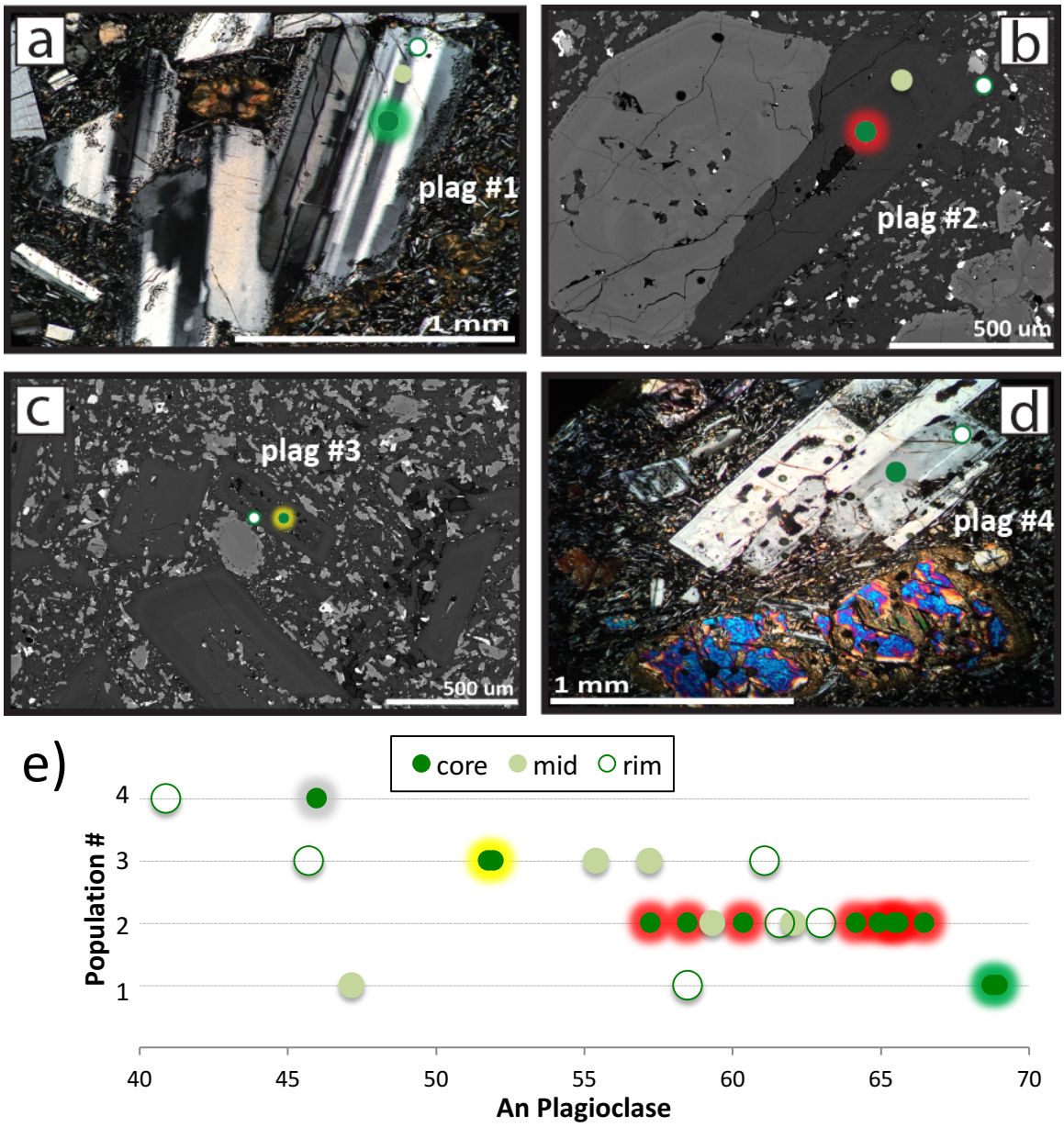

Figure 8. Plagioclase populations of andesite of Swift Creek (*asw*) with each population assigned a color code. a) Subhedral plagioclase with finely sieved outer zone and rounded overgrowth rims (population 1), the most calcic in composition. b) Subhedral plagioclase, with commonly reacted core (darker portion) (population 2). c) Euhedral plagioclase with blebby, coarsely sieved mid-zone that generally contains inclusions of apatite (population 3). d) Euhedral plagioclase with scattered blebby-coarse sieves and reacted spots (population 4), the most sodic in composition. e) Linear plot of core-to-rim compositions of plagioclase populations in *asw*.

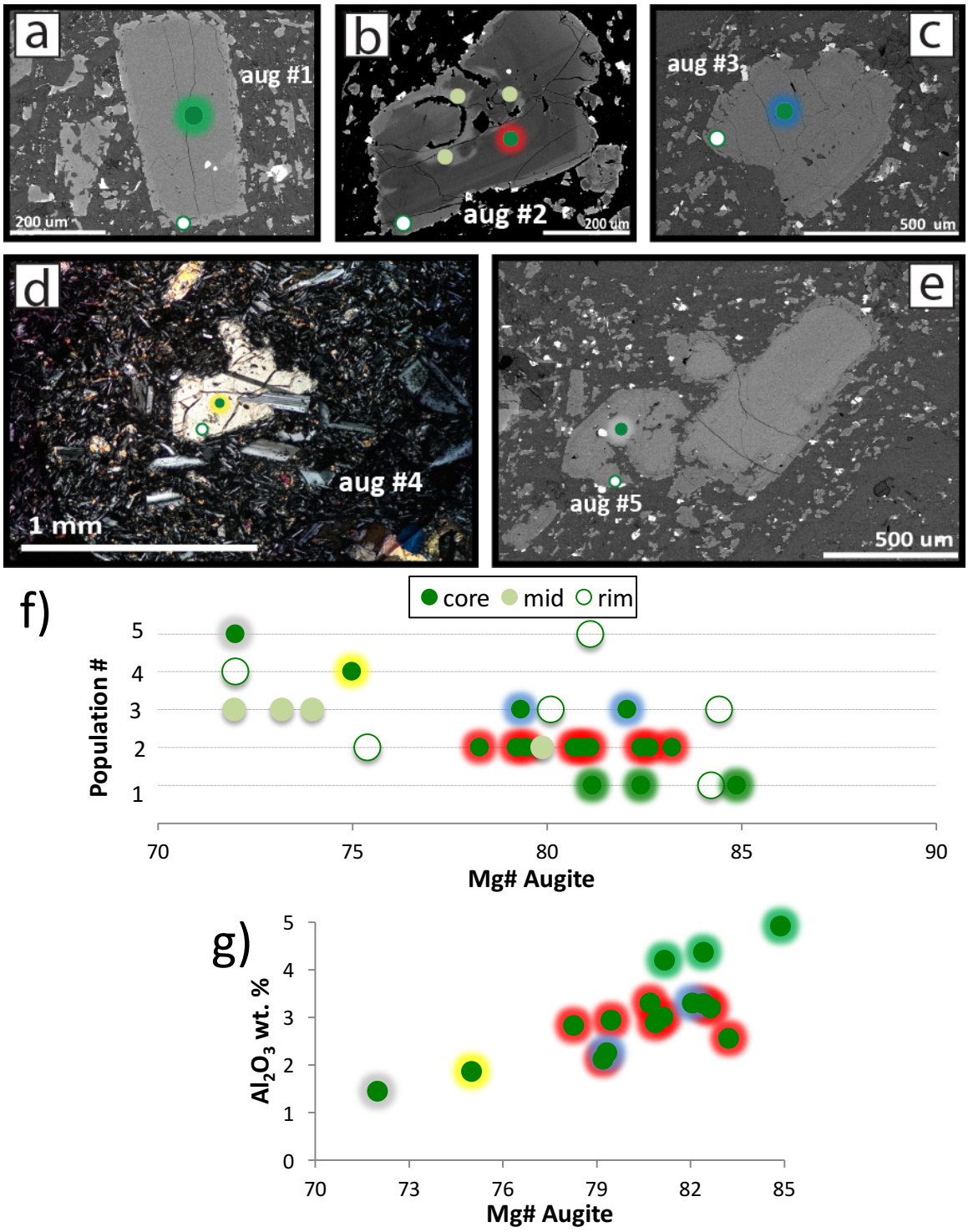

Figure 9. Augite populations of *asw* with each population assigned a color code. a) Euhedral augite with no disequilibrium textures, elevated Al_2O_3 concentrations (population 1), the most Mg rich population. b) Subhedral augite patchy Fe-rich blebs and embayments (population 2). c) Anhedral to subhedral augite with strong, reverse zoning and slight sieved core (population 3). d) Anhedral augite with slight sieved core and with plagioclase microphenocryst in embayment (population 4). e) Subhedral augite with oxide inclusions and large embayment (population 5), and also the most Mg poor population. f) Linear plot of core-to-rim compositions of augite populations. g) Al_2O_3 (wt. %) vs. Mg# of augite populations.

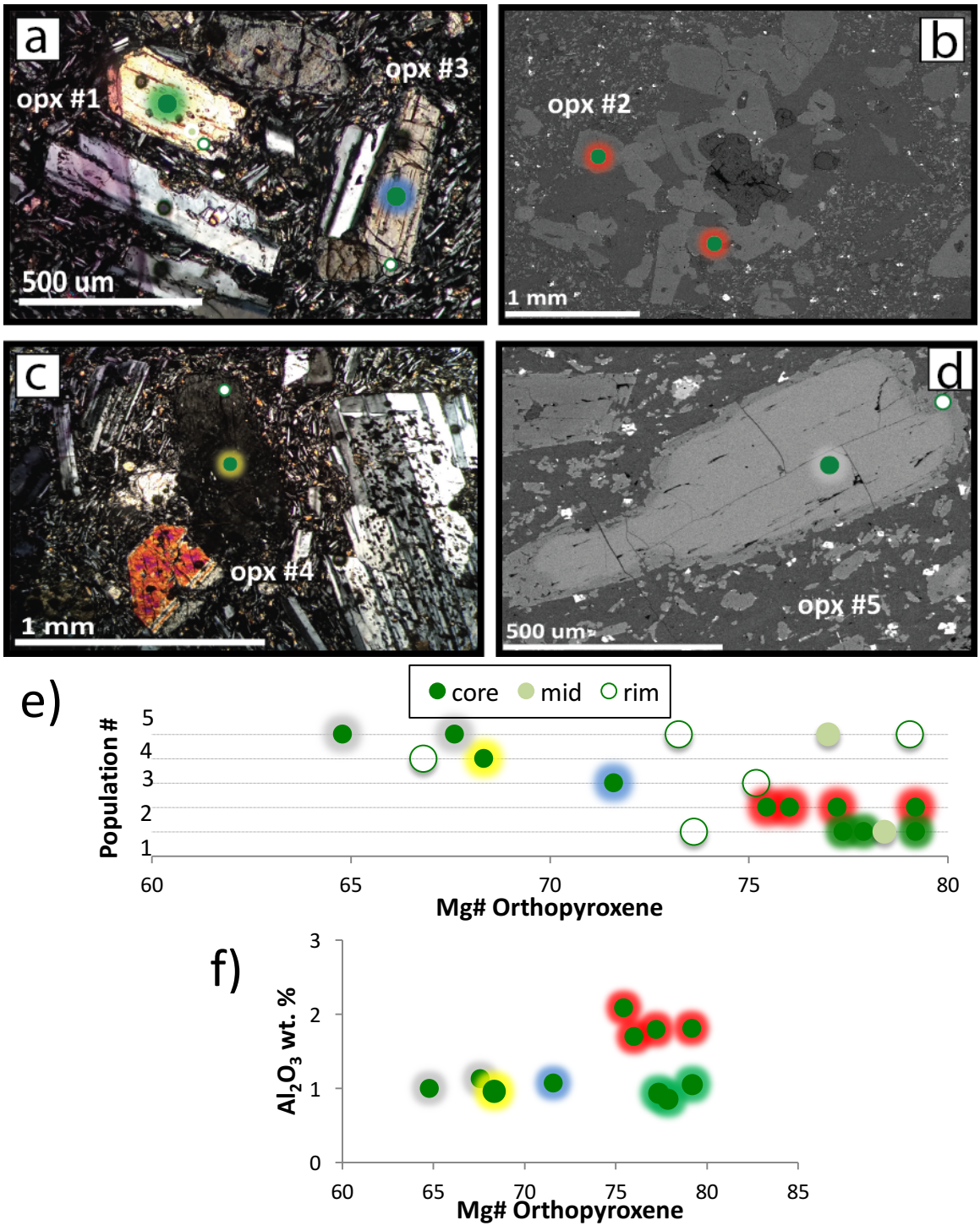

Figure 10. Orthopyroxene populations of *asw* with each population assigned a color code. a) Subhedral orthopyroxene with sieved core (green, population 1) and subhedral orthopyroxene (blue, population 3). b) Anhedral orthopyroxene with elevated Al_2O_3 concentrations and strictly found in crystal clots (population 2). d) Subhedral orthopyroxene (oriented at extinction) with minor exsolution of augite (population 4). d) Subhedral orthopyroxene with strong, reverse zoning (population 4), the most Mg poor population. e) Linear plot of core-to-rim compositions of orthopyroxene populations. f) Al_2O_3 (wt. %) vs. Mg# of orthopyroxene populations.

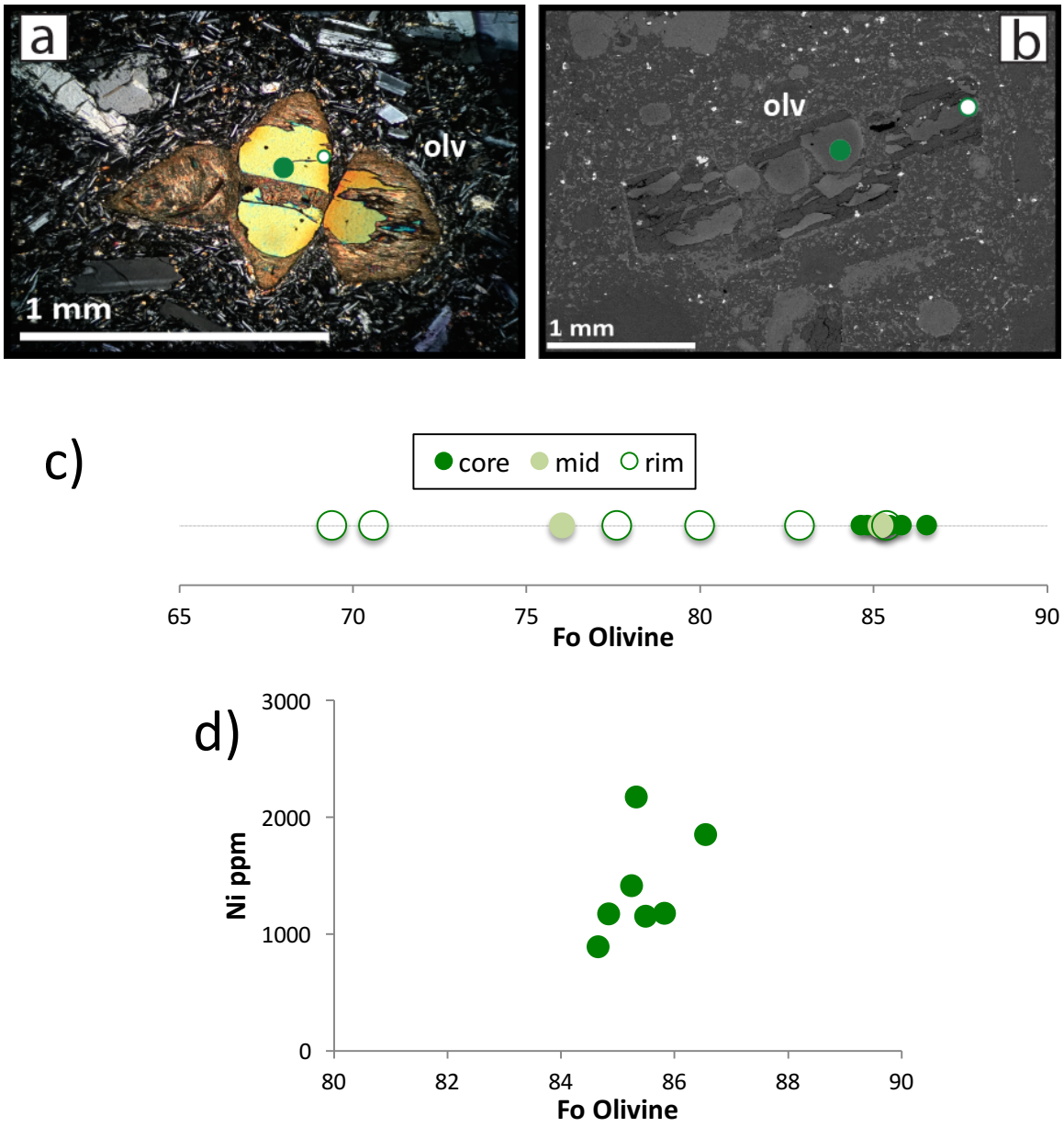

Figure 11. Olivine populations of *asw*. a) Euhedral, glomerocrystic olivine with chromite inclusions and oxidation reaction textures. b) Heavily embayed, euhedral olivine with oxidation reaction texture. c) Linear plot of core-to-rim compositions of olivine, d) concentrations of Ni (ppm) vs. Mg# (Fo) of olivine.

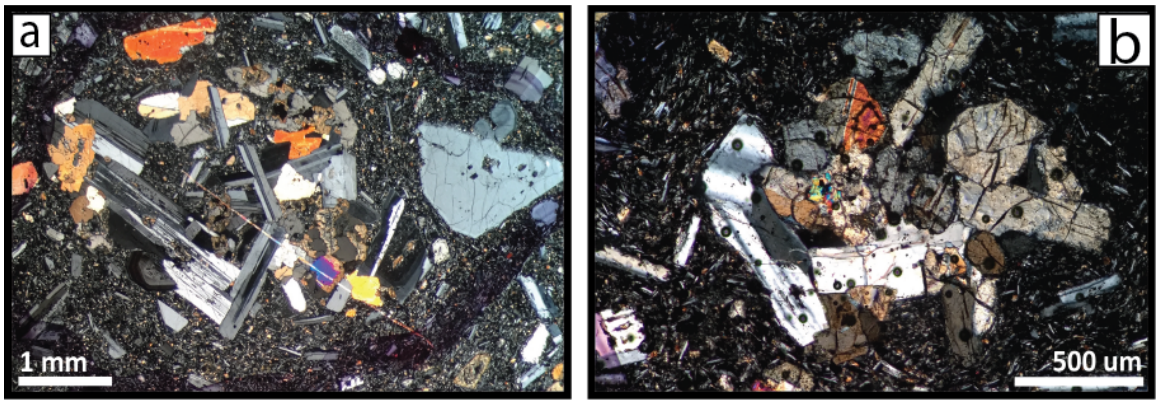

Clot A	
Olv (Fo)	85
Aug (Mg#)	79-83
Opx (Mg#)	75-79
Plag (An)	57-69

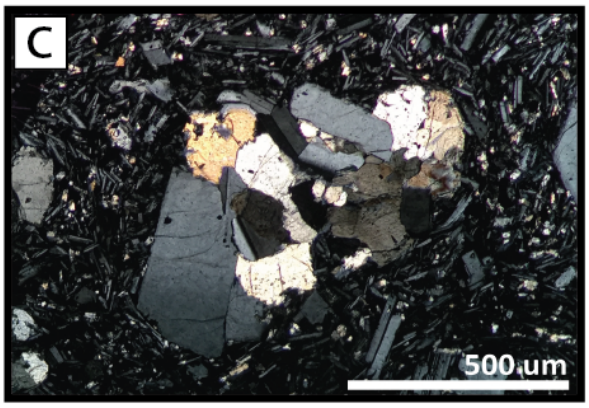

Clot B	
Olv (Fo)	-
Aug (Mg#)	81-82
Opx (Mg#)	-
Plag (An)	65

Figure 12. Crystal clots of *asw* with their core compositional ranges in tables to the right a) most common variety of crystal clot type A. b) smaller, and less common variety of crystal clot type A. b) microphenocrystic crystal clot type B with well interlocking grains.

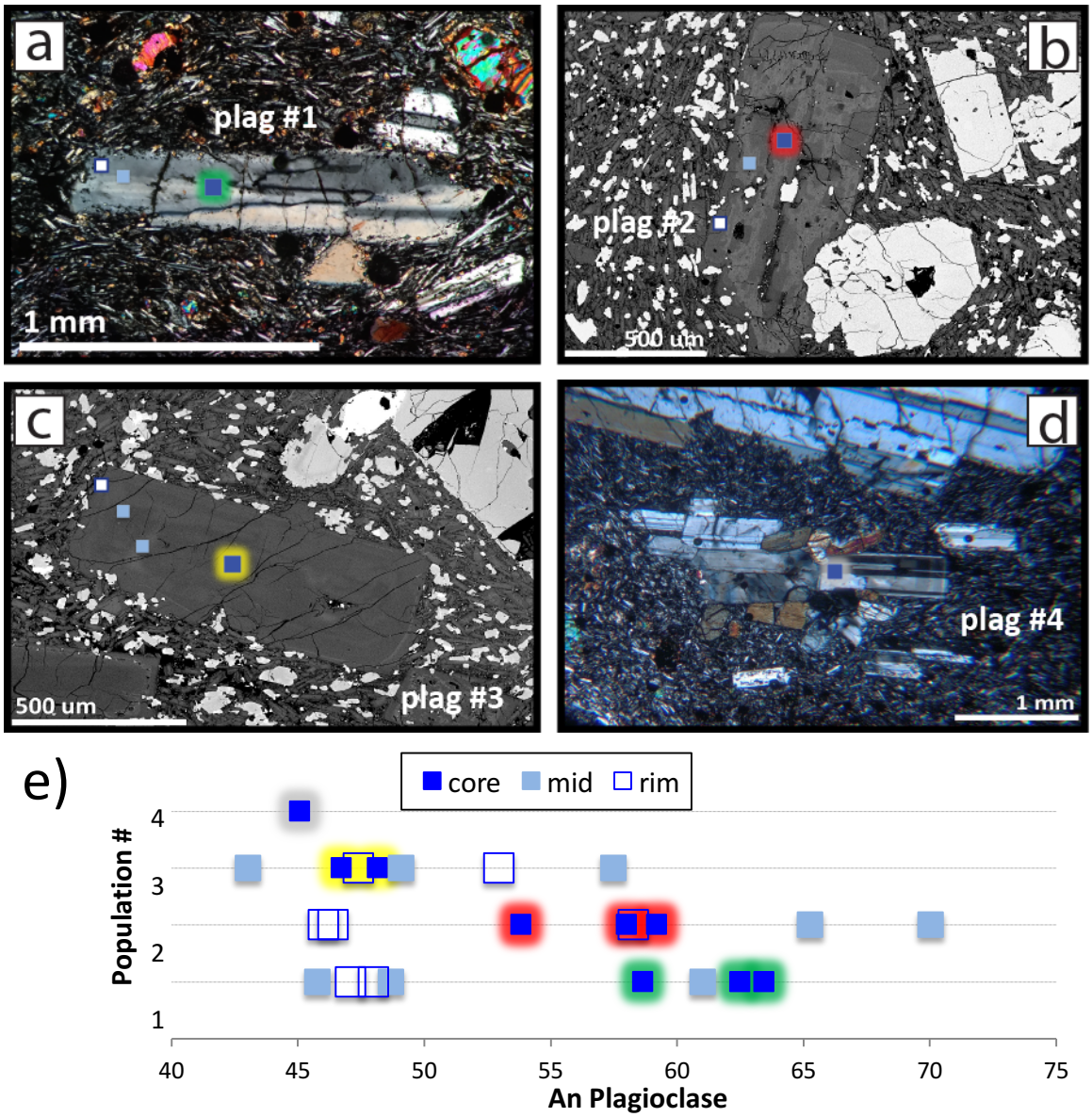

Figure 13. Plagioclase populations of andesite of Dobbs Creek (*ado*) with each population assigned a color code. a) Subhedral plagioclase with rounded, finely sieved rims that contain channelized groundmass (population 1), and is the most calcic in composition. b) Subhedral to euhedral plagioclase with patchy zoning and several oxide inclusions (population 2). c) Subhedral to euhedral plagioclase with slight rounded edges and lack of disequilibrium textures (population 3). d) Large, euhedral plagioclase, which contains occasional scattered sieves and is the most sodic in composition (population 4). e) Linear plot of core-to-rim compositions of plagioclase populations.

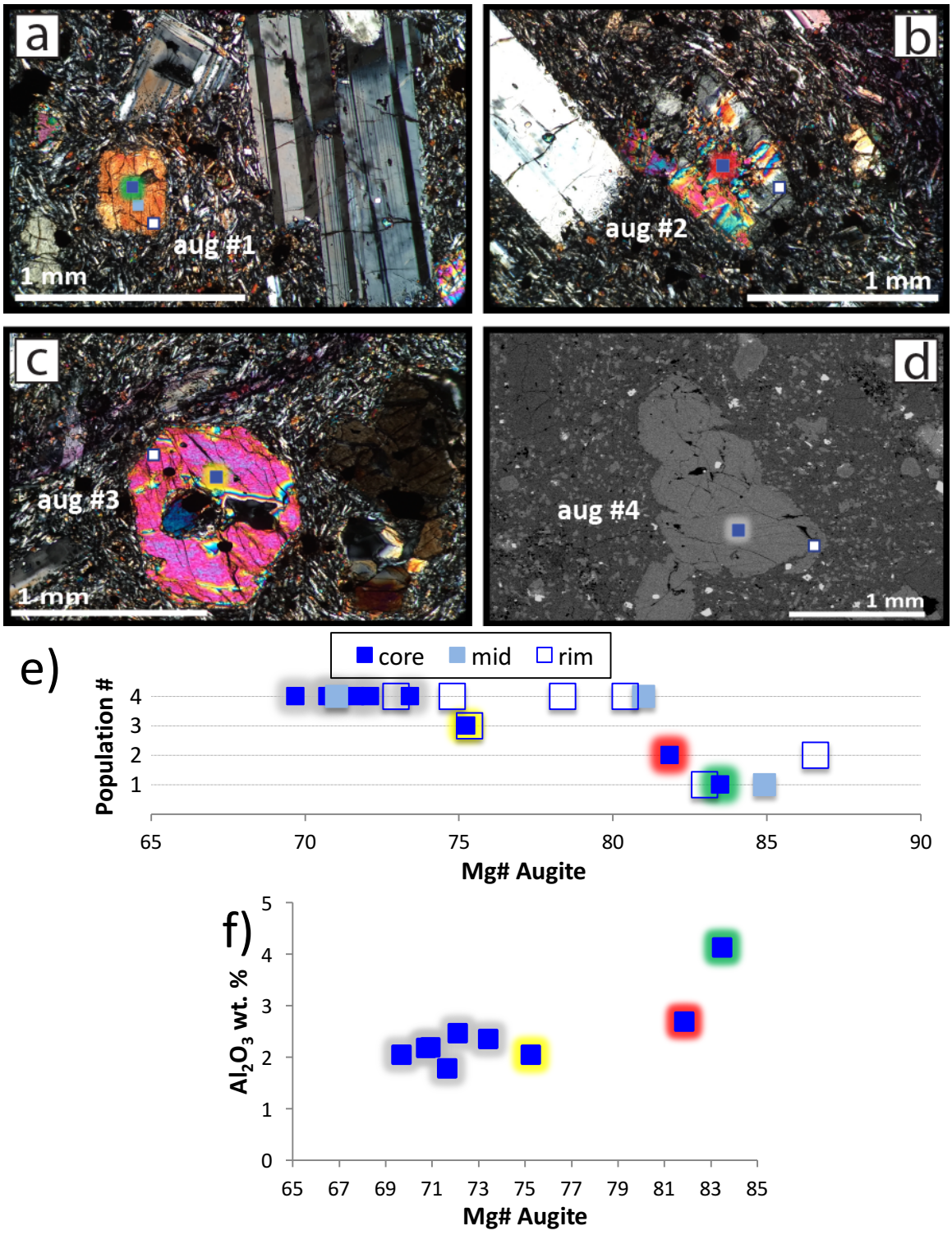

Figure 14. Augite populations of *ado* with each population assigned a color code. a) Equant, subhedral augite with high-Al concentrations and no disequilibrium textures (population 1), and also the most Mg rich population. b) Anhedral to subhedral, coarsely sieved augite with mosaic extinction (population 2). c) Unzoned, subhedral augite with resorbed core (population 3). d) Subhedral augites with strong, reversely zoned rims and minor embayments (population 4), the most Mg poor population. e) Linear plot of core-to-rim compositions of augite populations. f) Al_2O_3 (wt. %) vs. Mg# of augite populations.

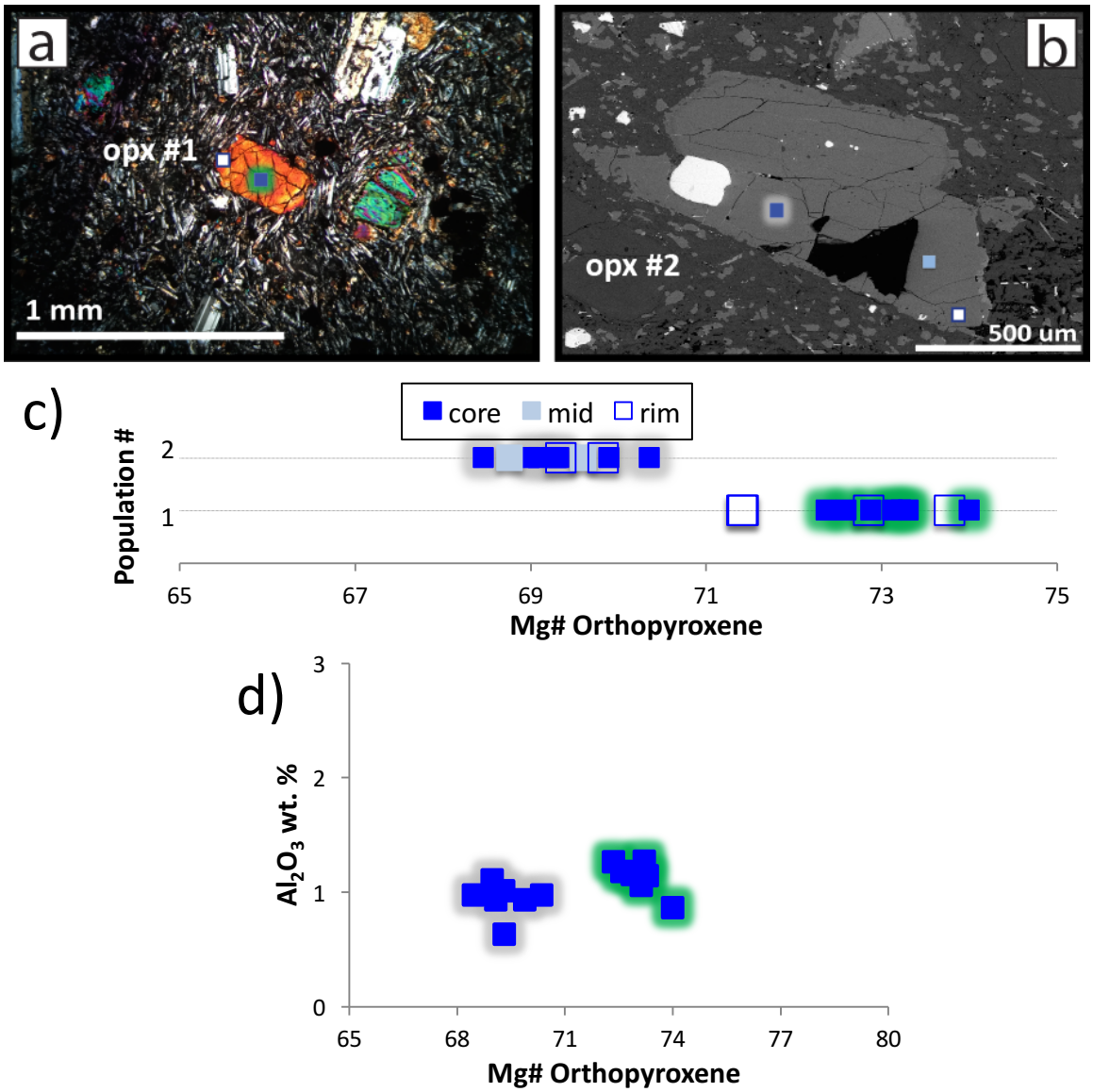

Figure 15. Orthopyroxene populations of *ado* with each population assigned a color code. a) Subhedral orthopyroxene that lacks disequilibrium textures (population 1) and is the most Mg rich population. b) Subhedral orthopyroxene with large oxide inclusion (population 2 c) Linear plot of core-to-rim compositions of orthopyroxene populations. d) Al_2O_3 (wt. %) vs. Mg# of orthopyroxene populations.

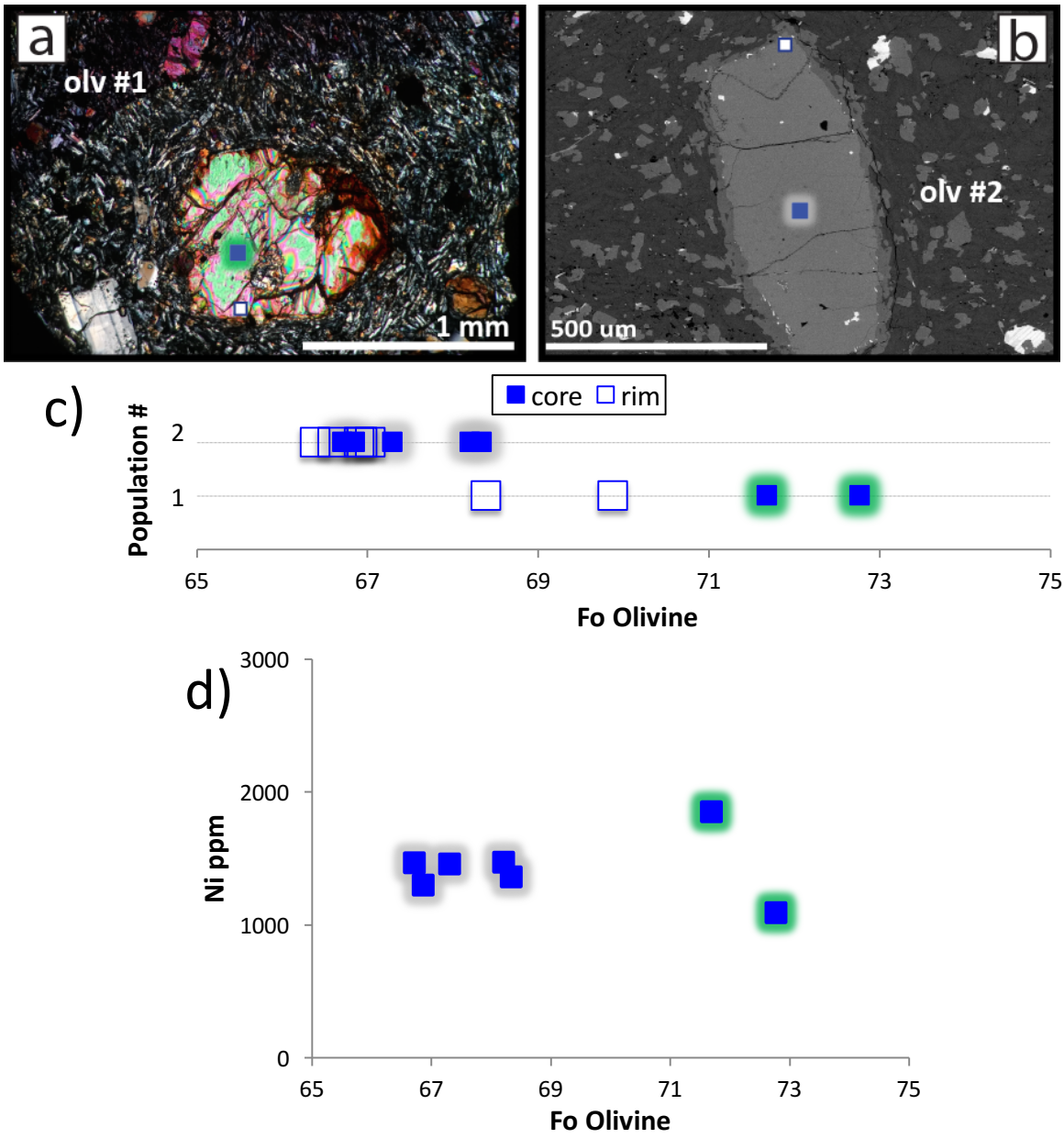

Figure 16. Olivine populations of *ado* with each population assigned a color code. a) Embayed, anhedral olivine (population 1), the most forsteritic in composition. b) Subhedral to euhedral olivine with oxide inclusions and rims of pyroxene (population 2). c) Linear plot of core-to-rim compositions of olivine populations. d) Concentrations of Ni (ppm) vs. Mg# (Fo) of olivine populations.

Clot A	
Olv (Fo)	-
Aug (Mg#)	71
Opx (Mg#)	69-70
Plag (An)	45

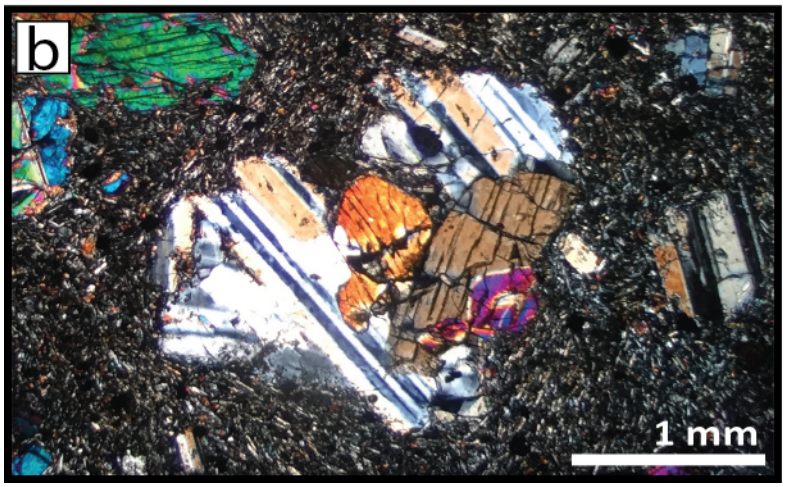

Clot B	
Olv (Fo)	-
Aug (Mg#)	-
Opx (Mg#)	72-73
Plag (An)	59

Figure 17. Crystal clots of *ado* with their core compositional ranges in tables to the right. a) Crystal clot type A. b) Crystal clot type B.

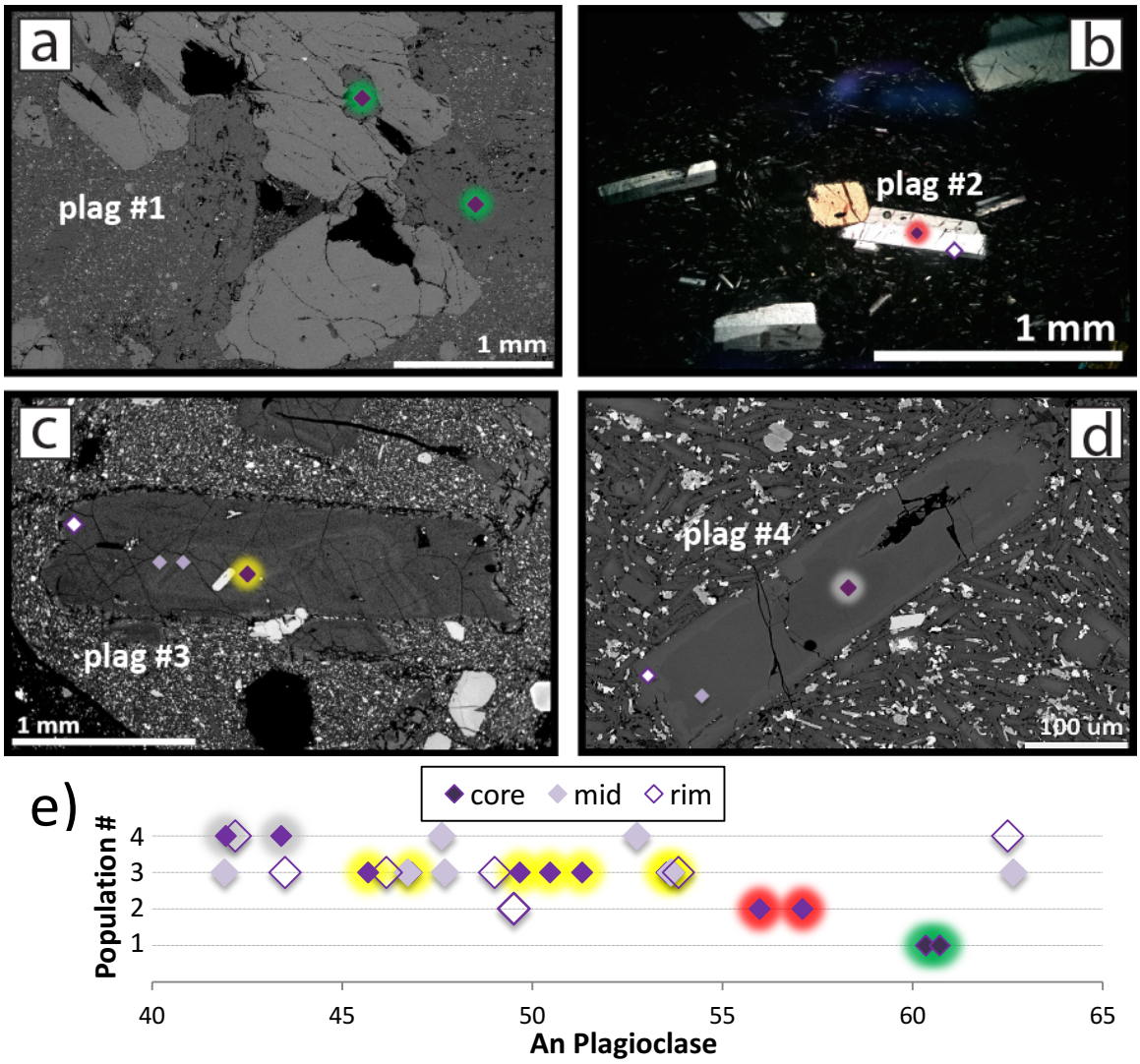

Figure 18. Plagioclase populations of andesite of Dobbs Cleaver (*adb*) with each population assigned a color code. a) Anhedral, coarsely sieved plagioclase found in crystal clots and the most calcic in composition (population 1). b) Euhedral plagioclase with no disequilibrium textures (population 2). c) Subhedral plagioclase with rounded, finely sieved rims and common apatite inclusions (population 3). d) Subhedral to euhedral plagioclase with occasional scattered sieves and the most sodic in composition (population 4). e) Linear plot of core-to-rim compositions of plagioclase populations.

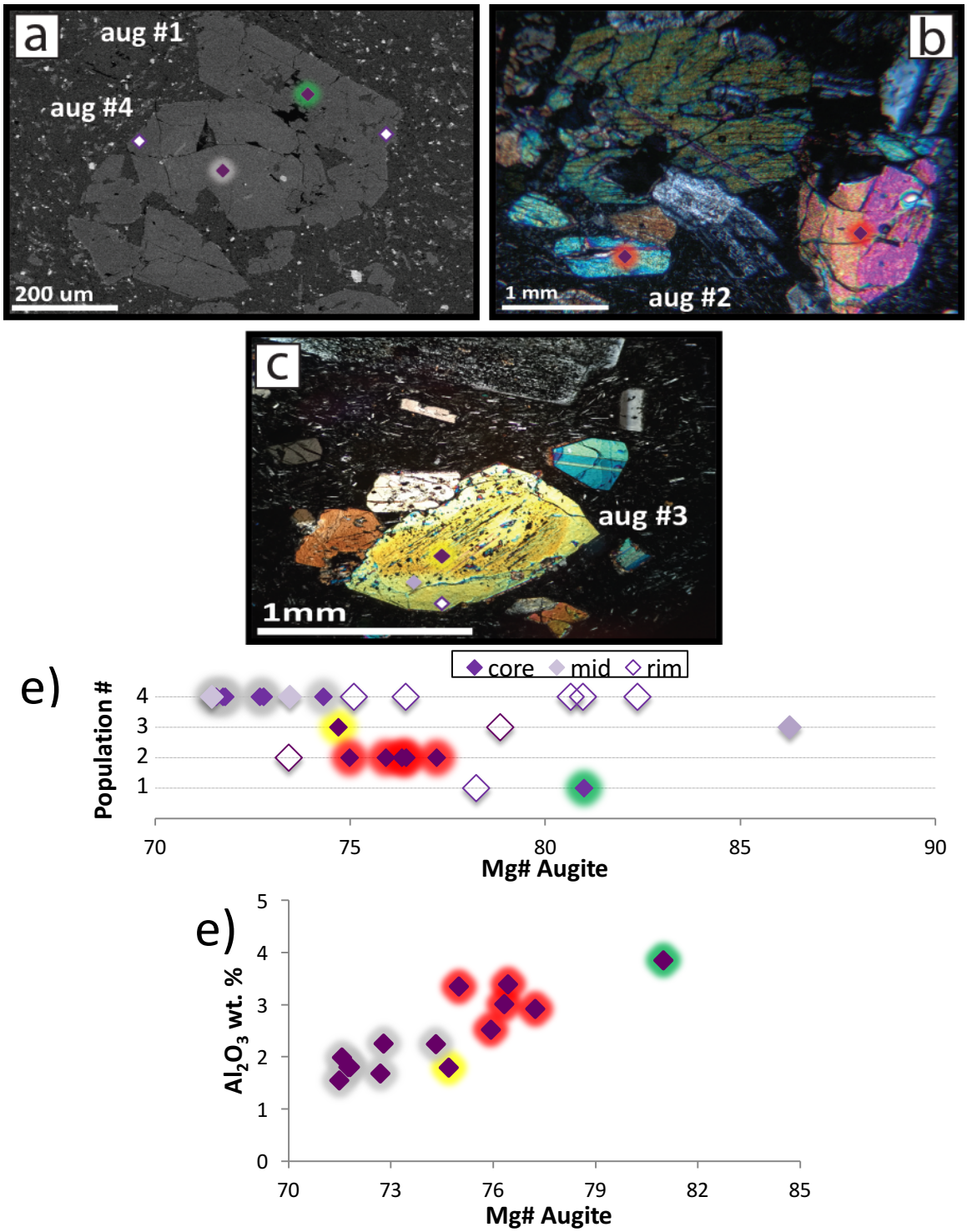

Figure 19. Augite populations of *adb* with each population assigned a color code. a) Subhedral to euhedral augite with coarse-sieved core (green, population 1), which is normally zoned and is the most Mg rich population. Heavily embayed, subhedral to euhedral augite (gray, population 4), which displays strong reverse zoning and is the most Mg poor population. b) Large, subhedral augite that lacks disequilibrium textures found in crystal clots and occasionally contains inclusions of plagioclase (population 2). c) Subhedral, finely sieved augite (population 3) with exsolution lamellae in the core. d) Linear plot of core-to-rim compositions of augite populations. e) Al_2O_3 (wt. %) vs. Mg# of augite populations.

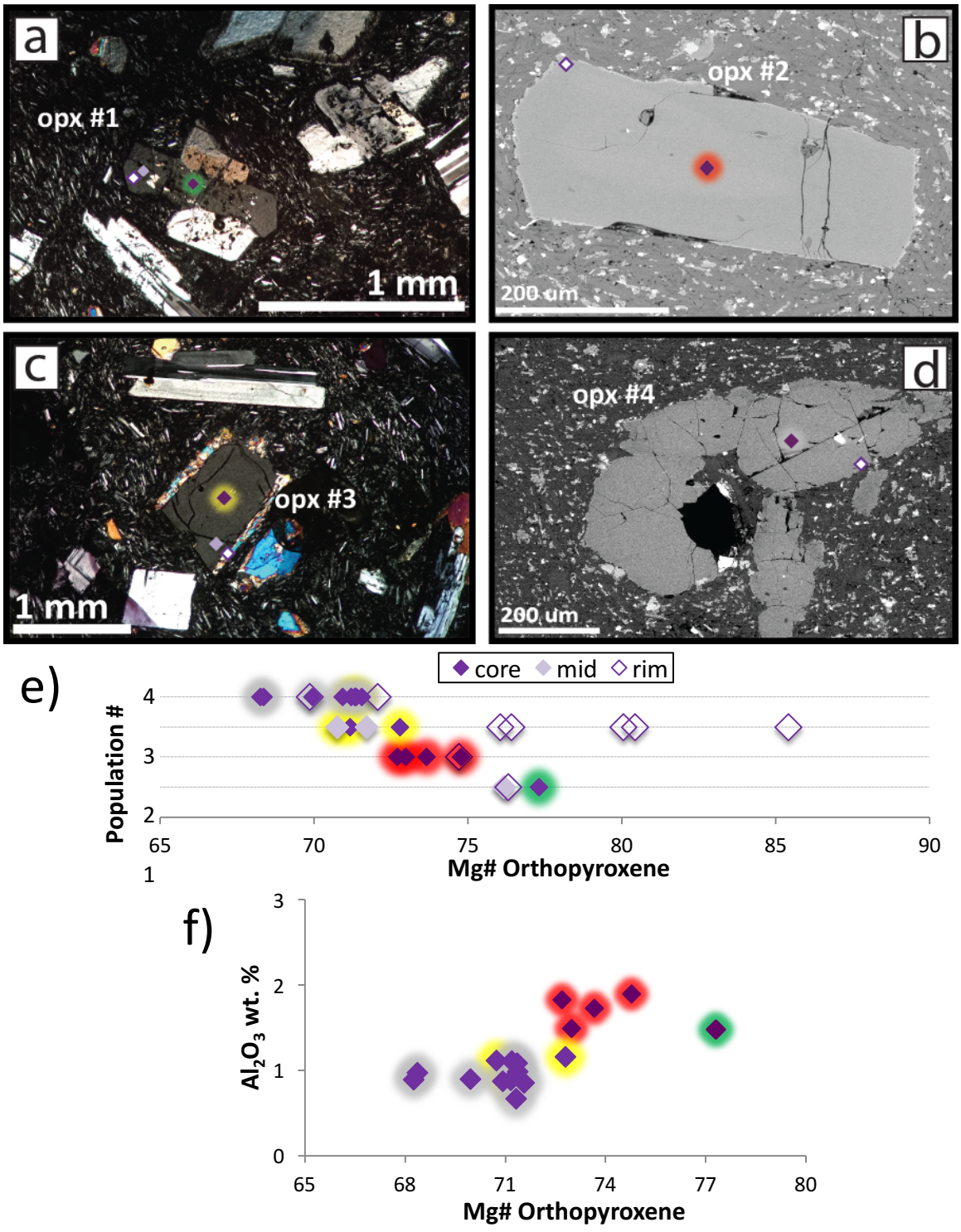

Figure 20. Orthopyroxene populations of *adb* with each population assigned a color code. a) Euhedral orthopyroxene of (oriented near full extinction) with exsolution and coarse-sieved core (population 1) and is the most Mg rich population. b) Euhedral orthopyroxene that lacks disequilibrium textures (population 2). c) Subhedral to euhedral orthopyroxene, with characteristic Mg-rich reaction rims of augite (population 3). d) Anhedral to subhedral orthopyroxene with embayments (population 4) and the most Mg poor population. e) Linear plot of core-to-rim compositions of orthopyroxene populations. f) Al_2O_3 (wt. %) vs. Mg# of orthopyroxene populations.

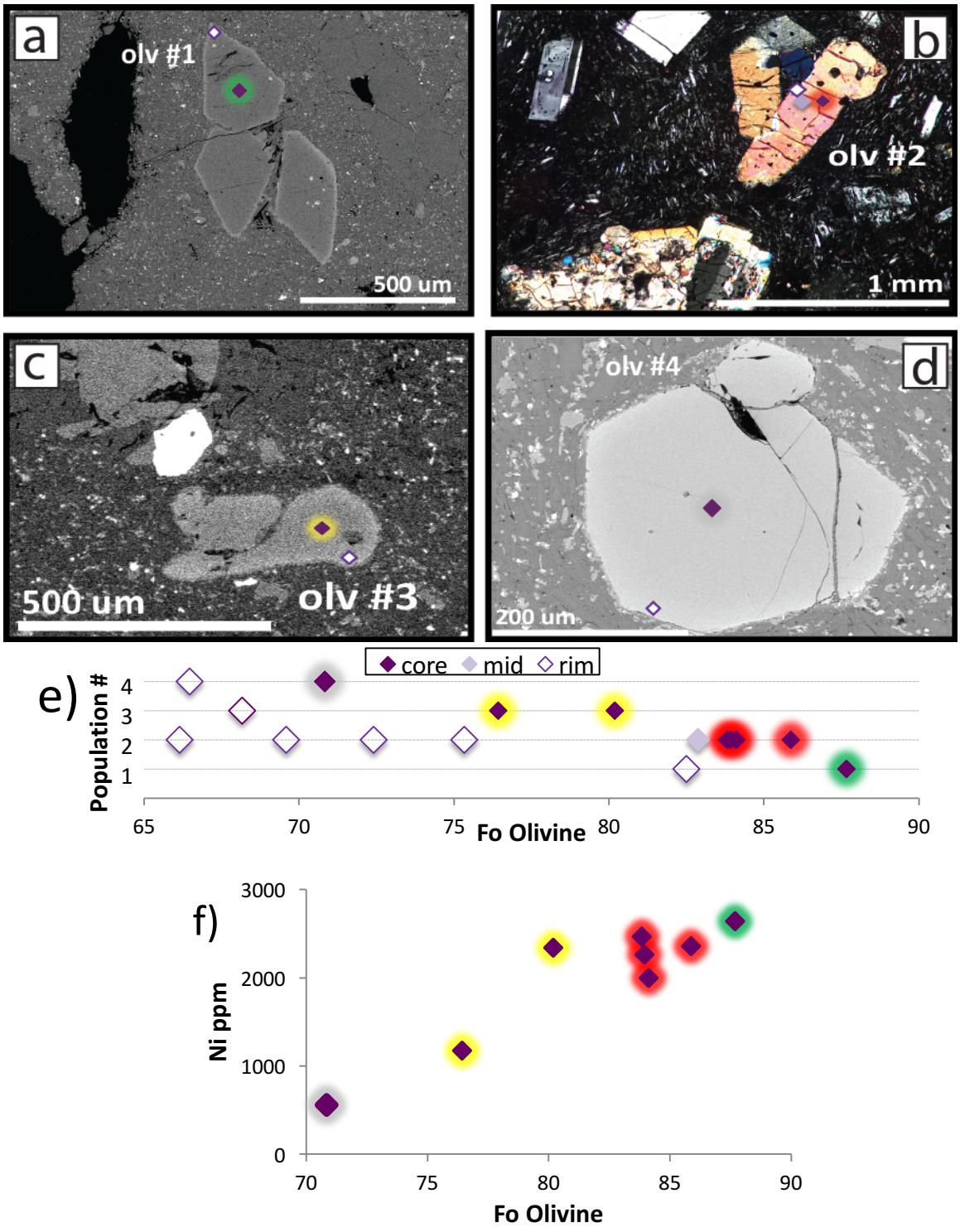

Figure 21. Olivine populations of *adb* with each population assigned a color code. a) Euhedral, glomerocrystic olivine with chromite inclusions (population 1), the most forsteritic in composition. b) Subhedral to euhedral, glomerocrystic olivine with abundant chromite inclusions (population 2). c) Embayed, anhedral olivine (population 3). d) Equant, subhedral olivine (population 4), the most fayalitic in composition. e) Linear plot of core-to-rim compositions of olivine populations. f) Concentrations of Ni (ppm) vs. Mg# (Fo) of olivine populations.

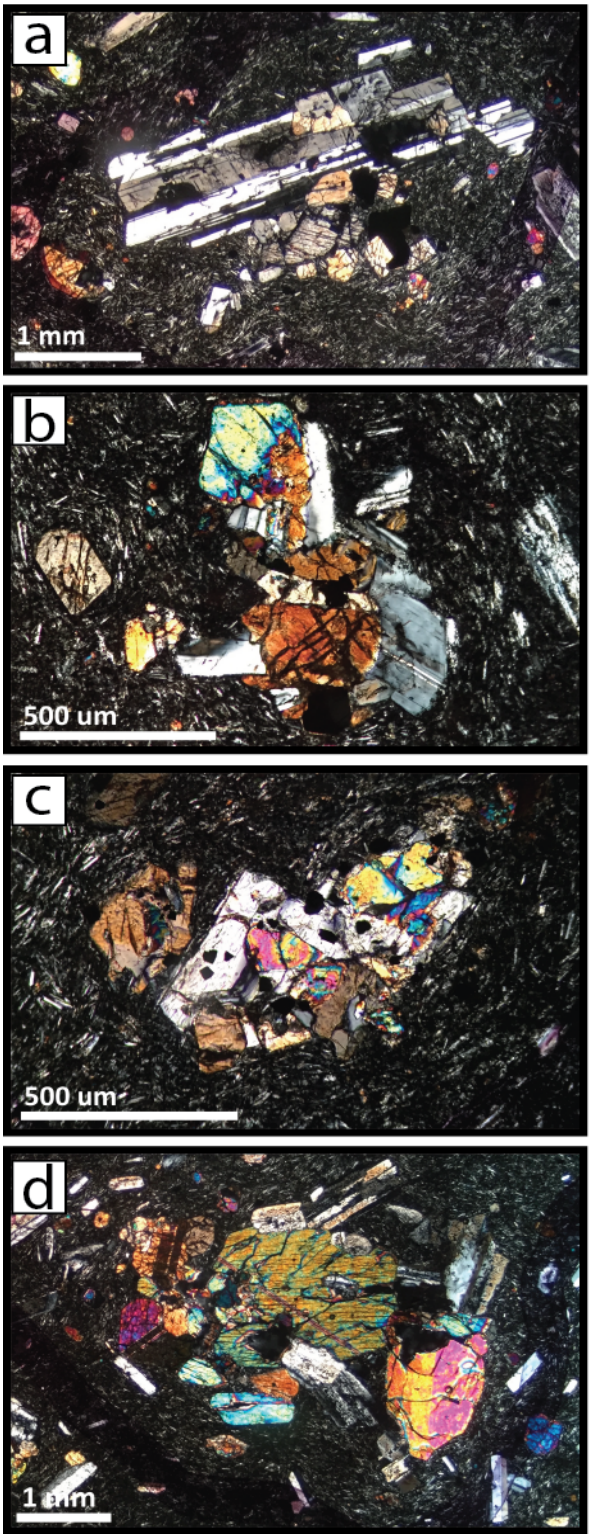

Clot A	
Olv (Fo)	-
Aug (Mg#)	71-72
Opx (Mg#)	68-72
Plag (An)	54

Clot B	
Olv (Fo)	-
Aug (Mg#)	76
Opx (Mg#)	73
Plag (An)	57

Clot C	
Olv (Fo)	80
Aug (Mg#)	-
Opx (Mg#)	73-75
Plag (An)	-

Clot D	
Olv (Fo)	-
Aug (Mg#)	75-77
Opx (Mg#)	-
Plag (An)	60-61

Figure 22. Crystal clot populations of *adb* with their core compositional ranges in tables to the right. a) Crystal clot type A. b) microphenocrystic crystal clot type B. c) microphenocrystic crystal clot type C. d) megacrystic crystal clot type D.

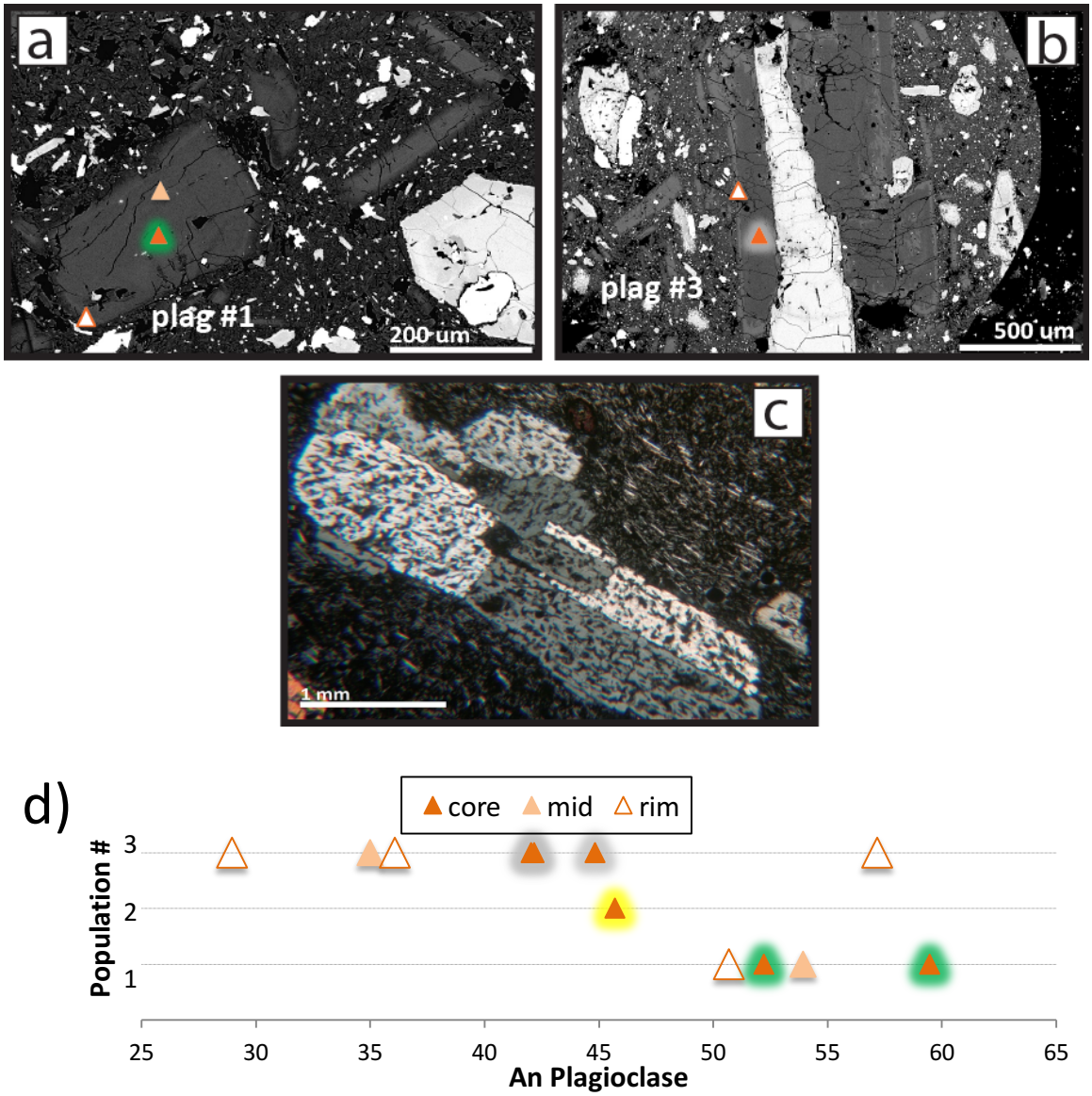

Figure 23. Plagioclase populations of andesite of Coleman Pinnacle (*acp*) with each population assigned a color code. a) Subhedral plagioclase that occurs as strictly microphenocrysts and commonly contains inclusions of apatite (population 1). b) Subhedral plagioclase with scattered coarse sieves and patchy zoning (population 3), the most calcic in composition. c) Blebby, coarse sieved plagioclase, abundant in dacitic samples (not analyzed) of *acp* and most likely related to blebby, coarse sieved plagioclase (population 2) of andesitic samples. d) Linear plot of core-to-rim compositions of plagioclase populations in andesitic samples of *acp*.

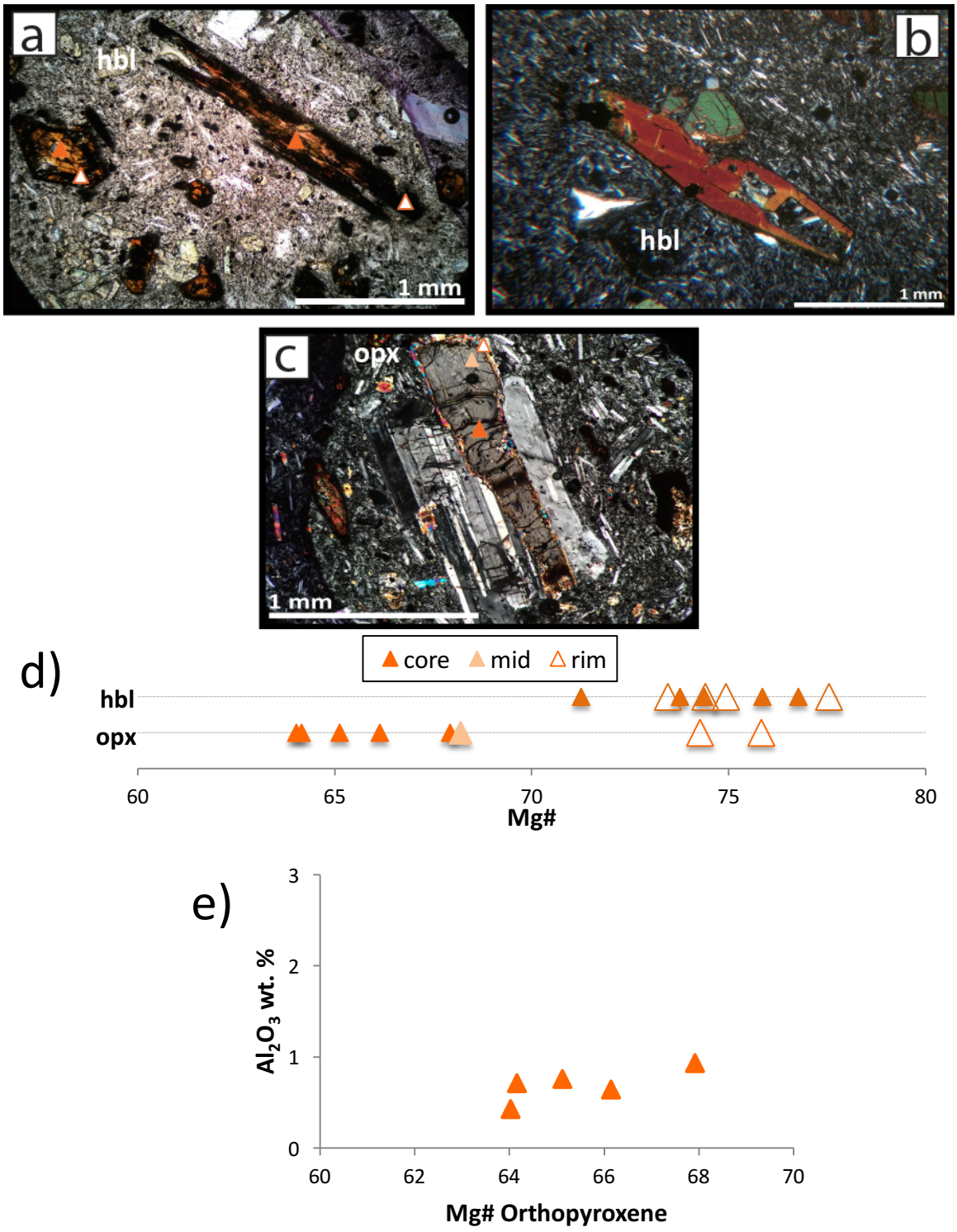

Figure 24. Notable textures and compositions of hornblende and orthopyroxene of *acp*. a) Subhedral to euhedral elongate and equant hornblende of the andesitic samples of *acp* displaying heavily oxidized rims. b) Euhedral hornblende of dacitic samples (not analyzed) of *acp* with large embayments. c) Subhedral orthopyroxene with reaction rim of augite and faint exsolution. d) Linear plot of core-to-rim compositions of andesitic hornblende (hbl) and orthopyroxene (opx). e) Al_2O_3 (wt. %) vs. Mg# of orthopyroxene.

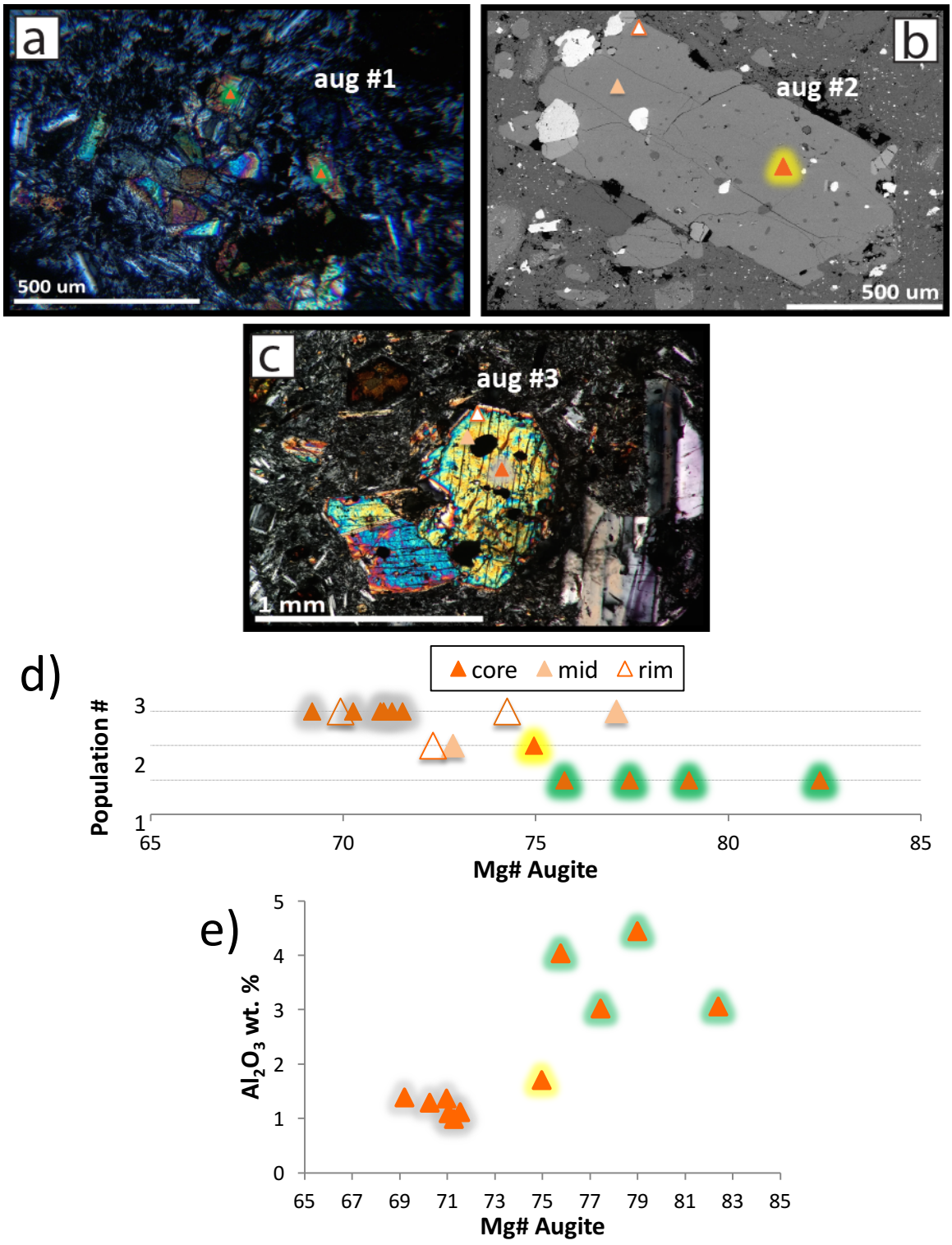

Figure 25. Augite populations of *acp* with each population assigned a color code. a) Anhedral augites found only in crystal clots that lack disequilibrium textures (population 1), the most Mg-rich population. b) Euhedral augite with abundant inclusions of oxides, plagioclase, and apatite (population 2). c) Subhedral augite with large oxide inclusions and a rim with distinct birefringence due to reverse zoning (population 3). d) Linear plot of core-to-rim compositions of augite populations. e) Al_2O_3 (wt. %) vs. Mg# of augite populations.

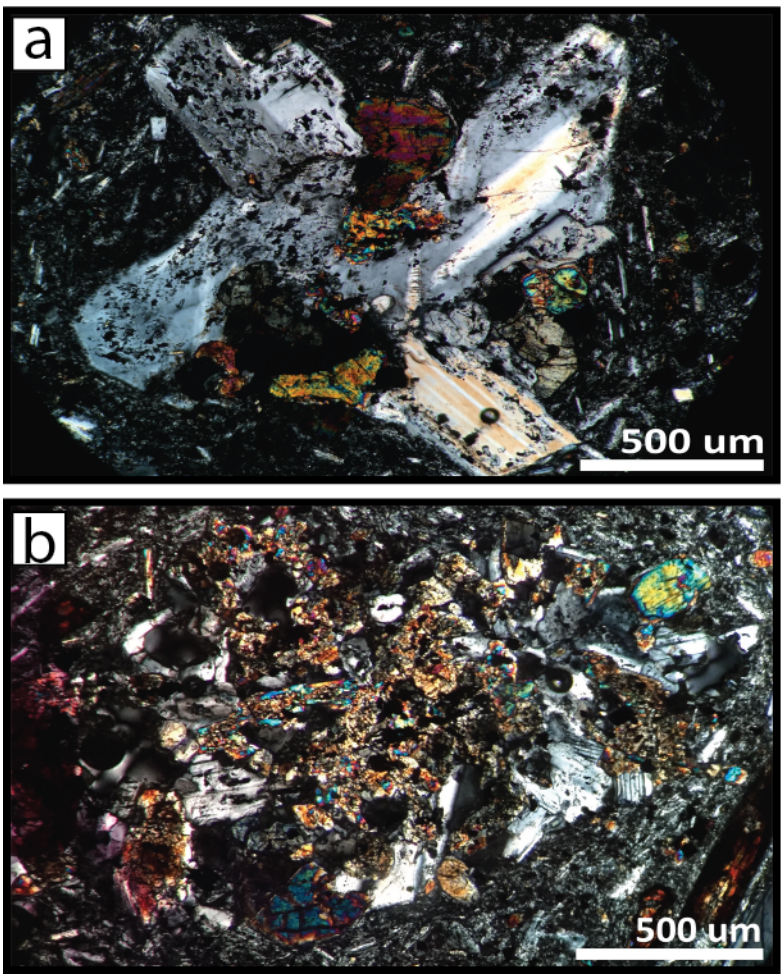

Clot A	
Hbl (Mg#)	-
Aug (Mg#)	70-72
Opx (Mg#)	64-65
Plag (An)	46

Clot B	
Hbl (Mg#)	-
Aug (Mg#)	76-82
Opx (Mg#)	66
Plag (An)	59

Figure 26. Crystal clots of the andesitic samples of *acp* with their core compositional ranges in tables to the right. a) Crystal clot type A. b) Crystal clot type B.

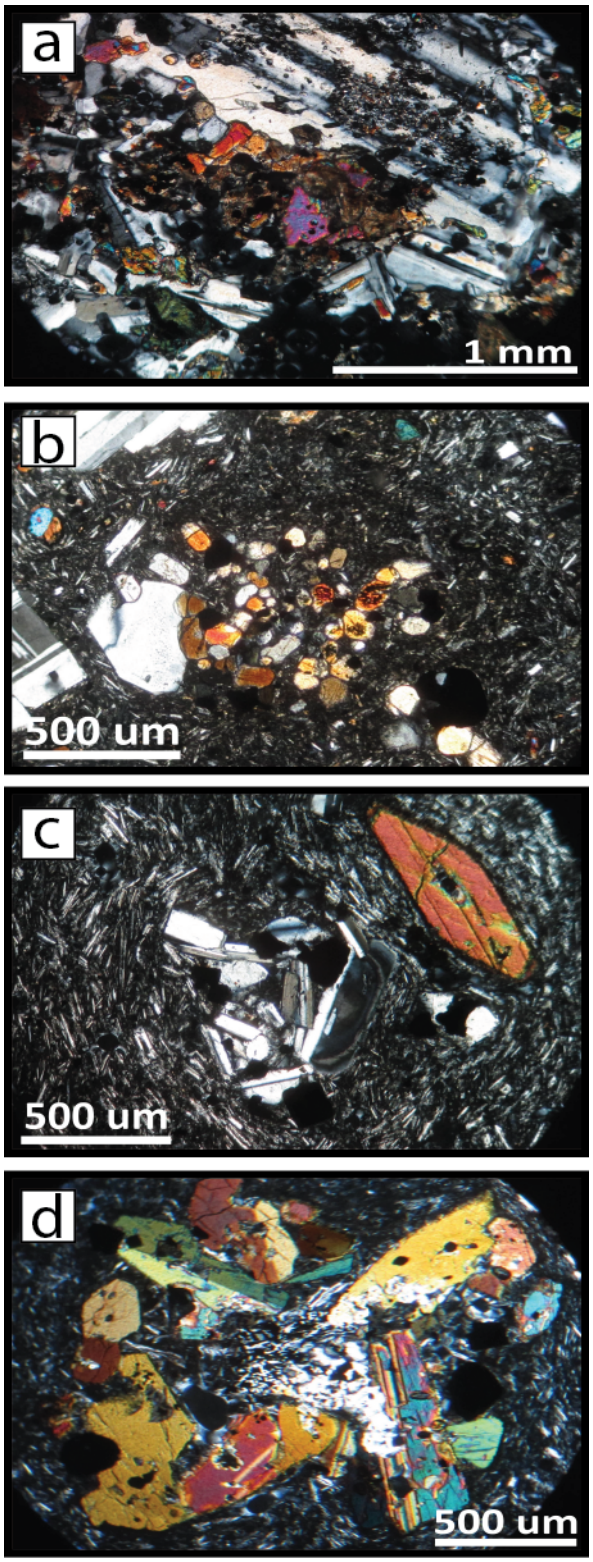

Figure 27. Unanalyzed crystal clots of both andesitic and dacitic samples of *acp.* a) An olivine-bearing version of clot type B in andesite of Coleman Pinnacle. b) Granular crystal clot composed predominantly of orthopyroxene observed in andesite of Coleman Pinnacle. c) Clot composed of strictly plagioclase and oxides in dacite of Coleman Pinnacle. d) Hornblende-bearing clot of dacite of Coleman Pinnacle.

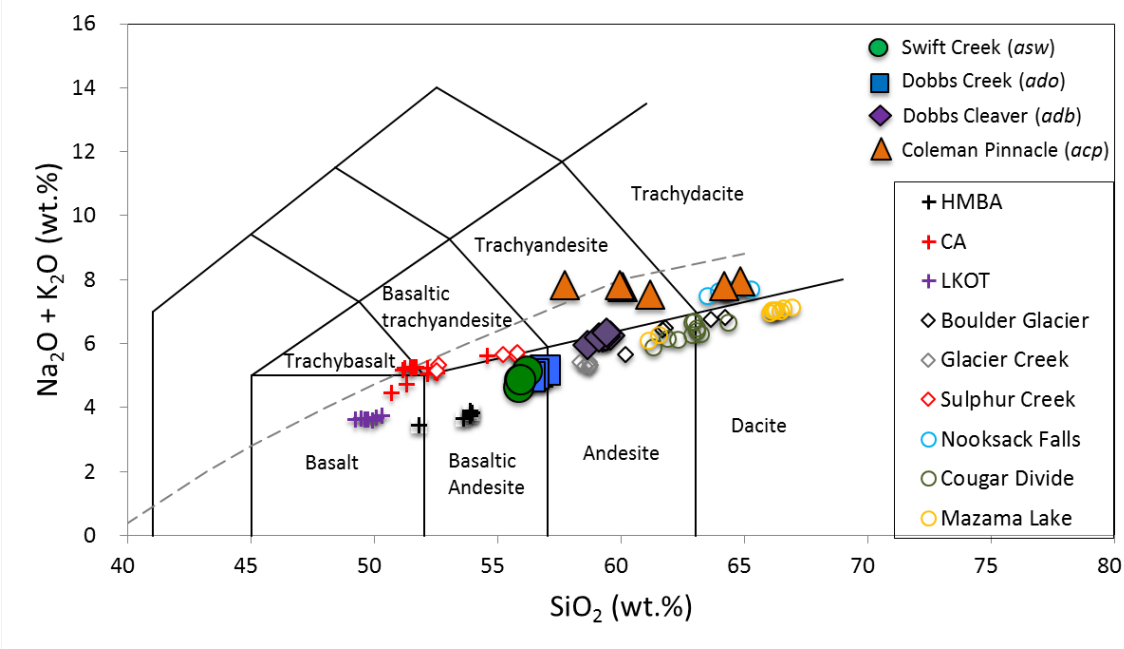

Figure 28. Total alkali vs. silica (TAS) diagram for andesites from this study, as well as compositions from Moore and DeBari (2012), Baggerman and DeBari (2011) and Gross (2012). The compositions form previous studies are enclosed by a box. Pluses represent compositions from Moore and DeBari (2012): black = high-Mg basaltic andesite (HMBA) of Tarn Plateau, red = calc-alkaline basalt (CA) of Lake Shannon and Sulphur Creek, purple = low-K tholeiitic basalt (LKOT) of Park Butte. Black outlined diamonds represent compositions from Baggerman and DeBari (2011): white = basaltic andesite of Sulphur Creek, grey = andesite of Glacier Creek, black = andesite of Boulder Glacier. Black outlined circles represent compositions from Gross (2012): blue = dacite of Nooksack Falls, olive green = dacite of Cougar Divide, yellow = andesite and dacite of Mazama Lake. Solid and larger symbols represent andesites of this study: green circle = andesite of Swift Creek (*asw*), blue square = andesite of Dobbs Creek (*ado*), purple diamond = andesite of Dobbs Cleaver (*adb*), orange triangle = andesite of Coleman Pinnacle (*acp*). Dashed line separates alkaline and subalkaline field, taken after Irvine and Baragar (1971). Plotting coordinates and nomenclature of subdivisions are taken after Le Maitre et al. (1989).

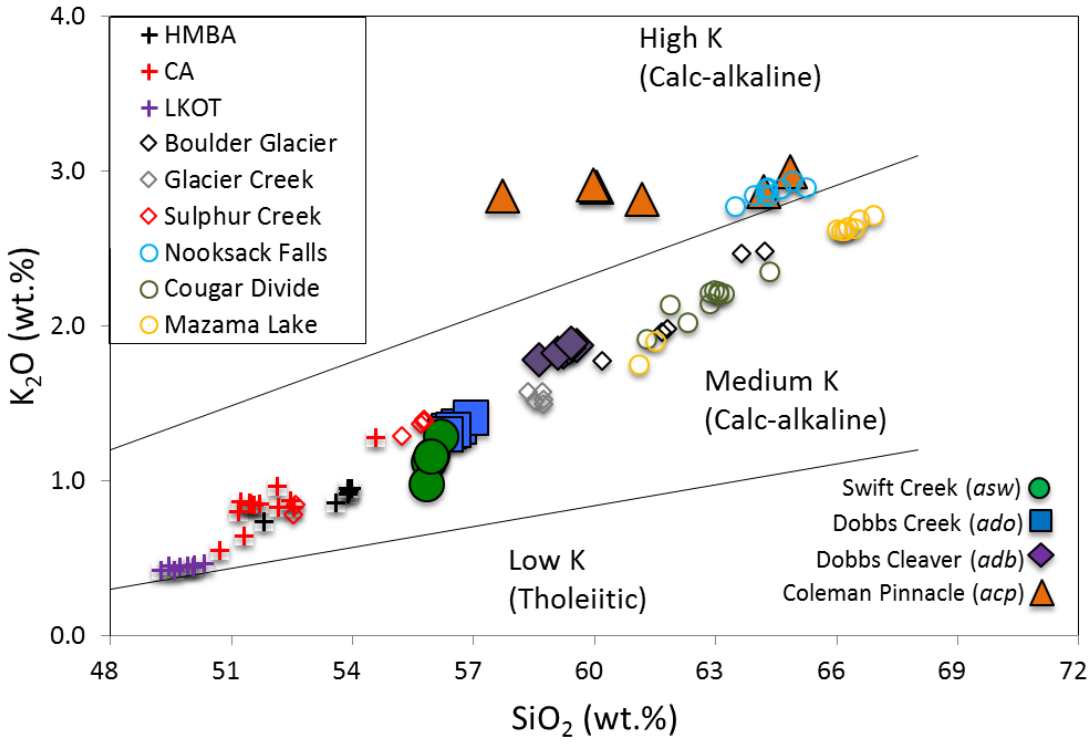

Figure 29. Total alkali vs. silica (TAS) diagram for andesites from this study, as well as compositions from Moore and DeBari (2012), Baggerman and DeBari (2011) and Gross (2012). The compositions from previous studies are enclosed by a box. Pluses represent compositions from Moore and DeBari (2012): black = high-Mg basaltic andesite (HMBA) of Tarn Plateau, red = calc-alkaline basalt (CA) of Lake Shannon and Sulphur Creek, purple = low-K tholeiitic basalt (LKOT) of Park Butte. Black outlined diamonds represent compositions from Baggerman and DeBari (2011): white = basaltic andesite of Sulphur Creek, grey = andesite of Glacier Creek, black = andesite of Boulder Glacier. Black outlined circles represent compositions from Gross (2012): blue = dacite of Nooksack Falls, olive green = dacite of Cougar Divide, yellow = andesite and dacite of Mazama Lake. Solid and larger symbols represent andesites of this study: green circle = andesite of Swift Creek (*asw*), blue square = andesite of Dobbs Creek (*ado*), purple diamond = andesite of Dobbs Cleaver (*adb*), orange triangle = andesite of Coleman Pinnacle (*acp*). Plotting coordinates for K-fields taken after Le Maitre et al. (1989).

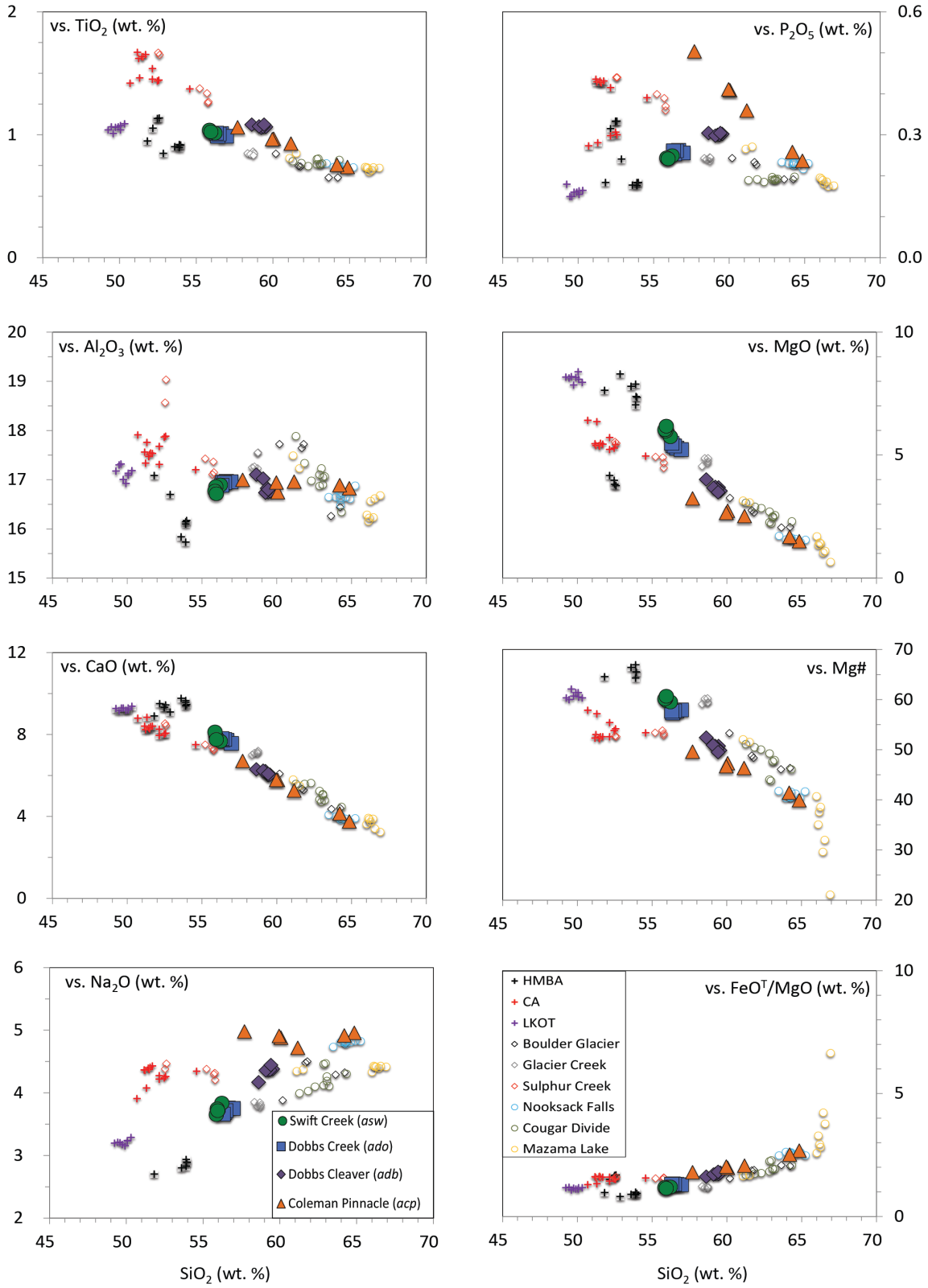

Figure 30. Whole rock major element compositions for each unit from this study, including compositions from Moore and DeBari (2012), Baggerman and DeBari (2011) and Gross (2012). All diagrams are plotted against SiO_2 (wt. %).

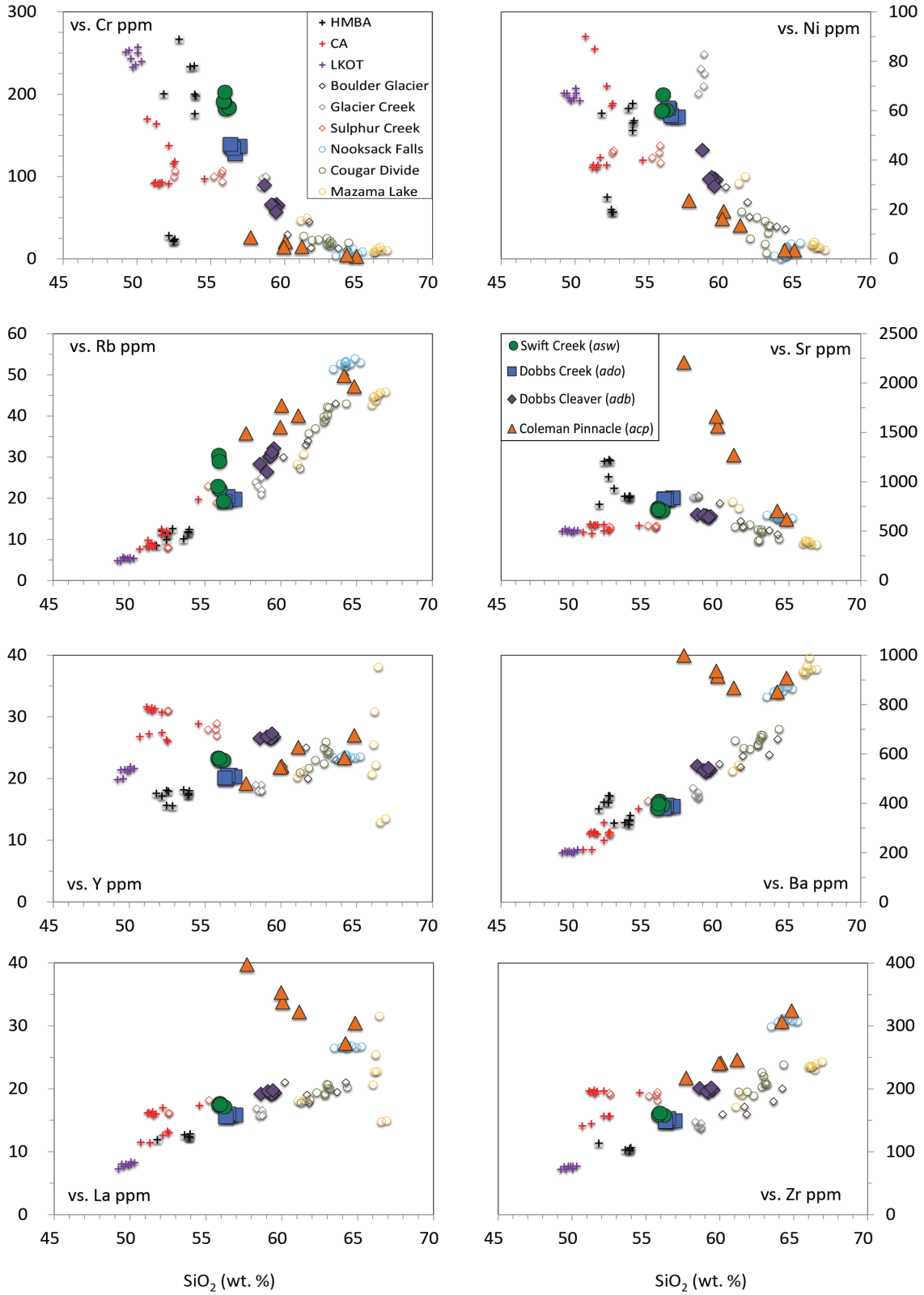

Figure 31. Trace element compositions for each unit from this study, including compositions from Moore and DeBari (2012), Baggerman and DeBari (2011) and Gross (2012). All diagrams are plotted against SiO_2 (wt. %).

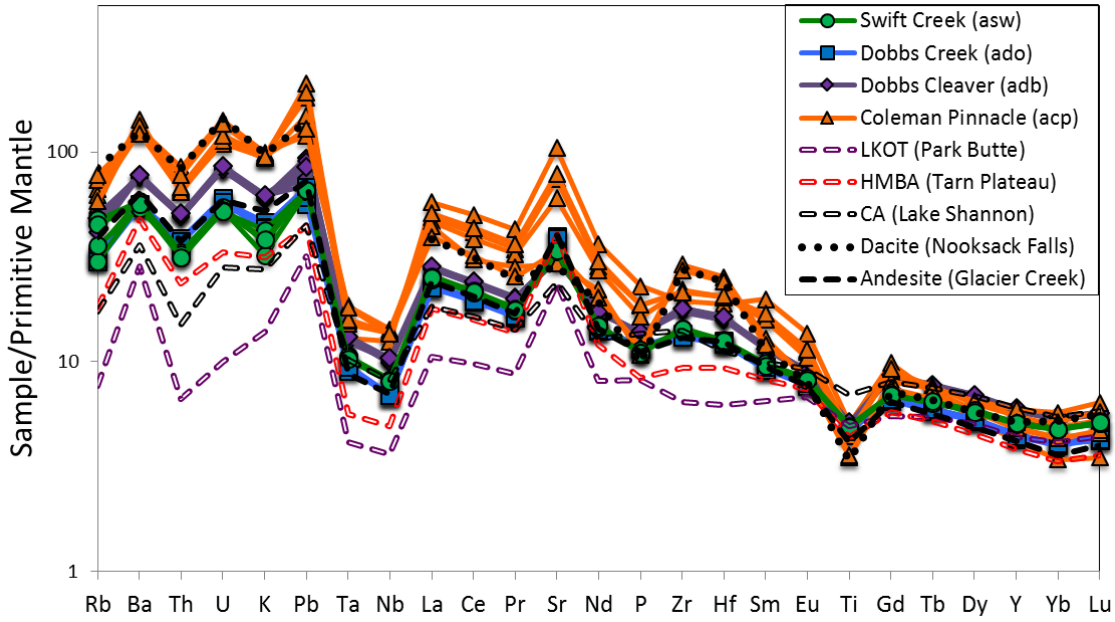

Figure 32. Primitive mantle normalized trace element diagram for all samples in this study and representative samples (LKOT of Park Butte, NM-PB3; HMBA of Tarn Plateau, NM-TP4; CA of Lake Shannon, NM-LS4; CA of Sulphur Creek, NM-SC4; dacite of Nooksack Falls, JG-NF8; andesite of Glacier Creek, TB-GC3) from previous studies of the Mount Baker volcanic field. Samples in this study are represented by the same colors assigned in all other figures. Samples are normalized after Sun and McDonough (1989) and with the exception of P and Ti after McDonough and Frey (1989).

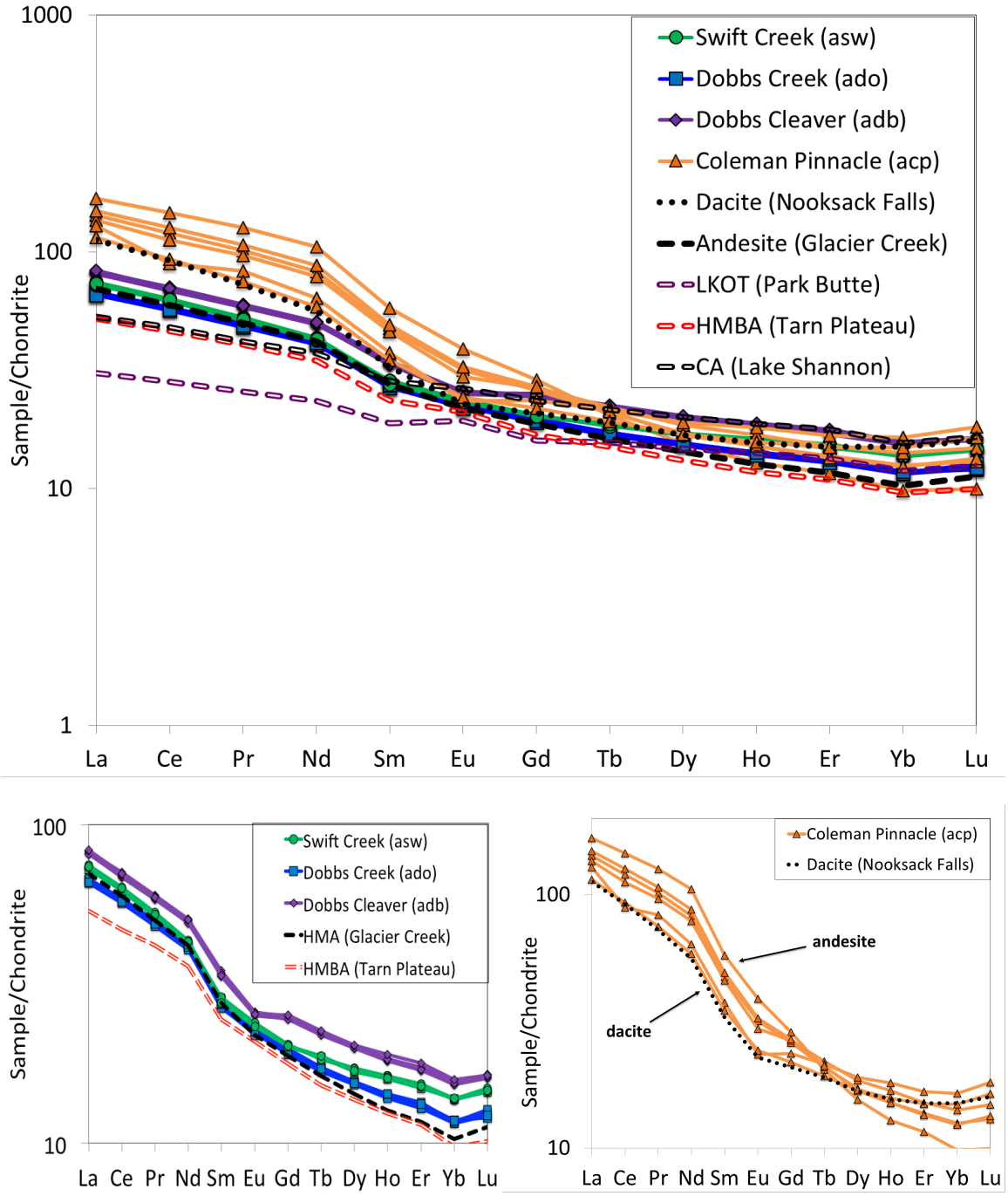

Figure 33. Chondrite normalized REE diagrams after Sun and McDonough (1989): a) REE concentrations of all samples in this study with representative samples (LKOT of Park Butte, NM-PB3; HMBA of Tarn Plateau, NM-TP4; CA of Lake Shannon, NM-LS4; CA of Sulphur Creek, NM-SC4; dacite of Nooksack Falls, JG-NF8; andesite of Glacier Creek, TB-GC3) from previous studies of Mount Baker volcanic field. b) the andesites of Dobbs Cleaver, Dobbs Creek and Swift Creek illustrating homogenous REE abundances within each flow. The andesite of Glacier Creek (TB-GC3) is included to display similarity in REE abundances. c) The andesite of Coleman Pinnacle illustrates heterogeneous REE abundances with the dacitic samples displaying the shallowest slopes and the andesitic samples the steepest slopes. The dacite of Nooksack Falls (JG-NF8) is included to demonstrate its nearly identical REE abundances to the dacitic samples of Coleman Pinnacle.

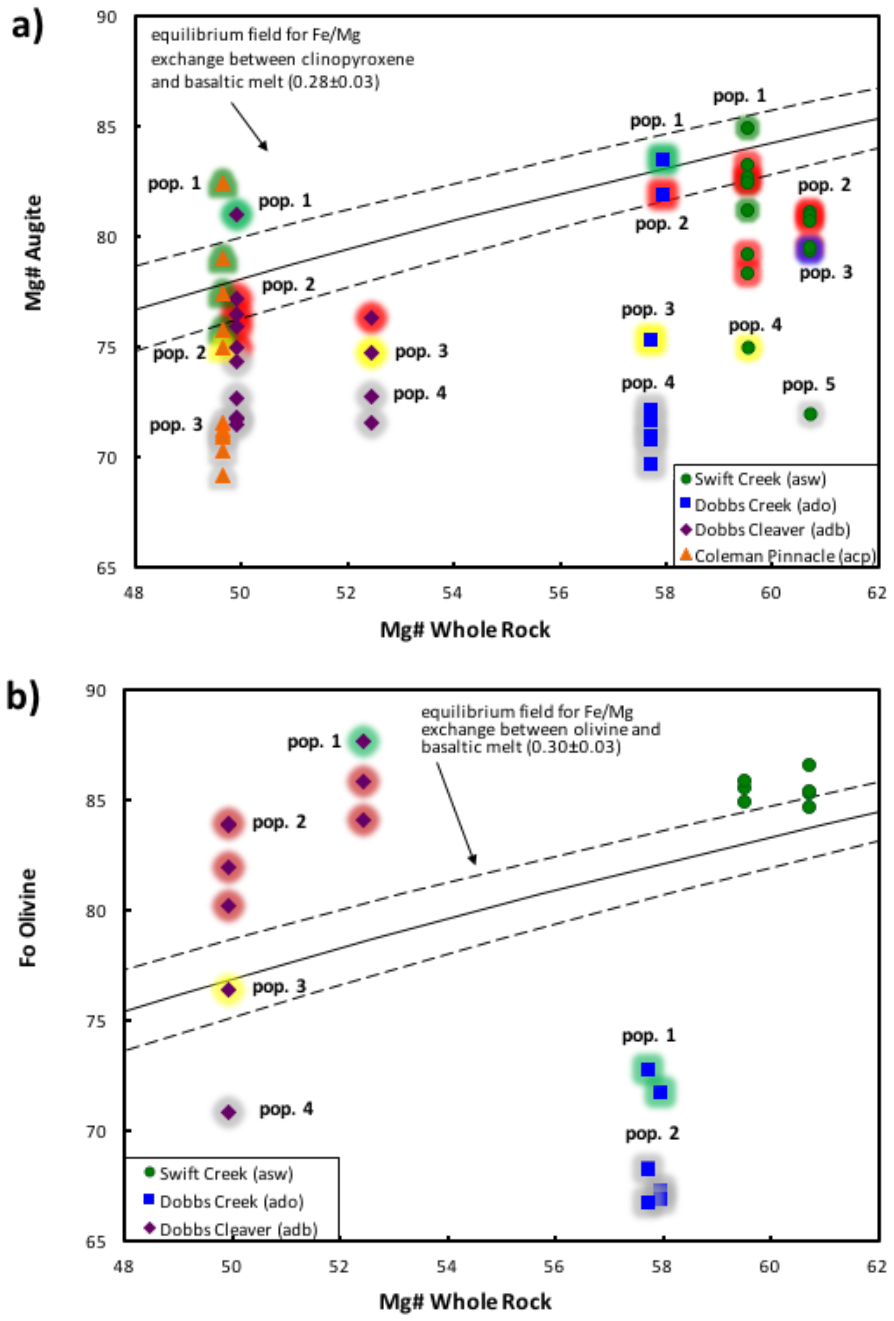

Figure 34. a) Augite core compositions from all flow units with their population colors. Colors of the rinds are as in figures 9, 14, 19 and 25: *asw* – green (population 1), red (population 2) blue (population 3), yellow (population 4), gray (population 5); *ado* – green (population 1), red (population 2), yellow (population 3), gray (population 4); *adb* – green (population 1), red (population 2), yellow (population 3), gray (population 4); *acp* – green (population 1), yellow (population 2), gray (population 3). Solid black line represents equilibrium liquid based on K_D of 0.28 (Putirka et al., 2003). Dashed lines are error margins (±0.03). b) Olivine core compositions from all flow units with their population colors. Color of the rinds are as in figures 16 and 21: *ado* – green (population 1) and gray (population 2); *adb* – green (population 1), red (population 2), yellow (population 3), gray (population 4). Solid black line represents equilibrium liquid based on K_D of 0.30 (Roeder and Emslie, 1970). Dashed line are error margins (±0.03).

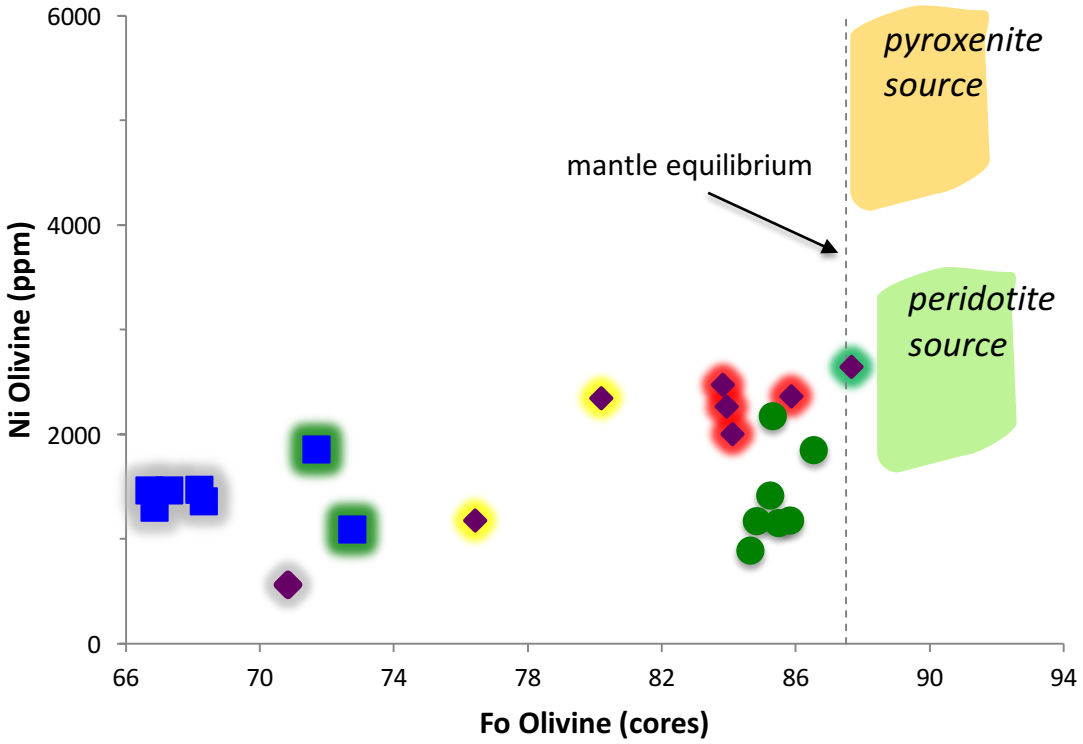

Figure 35. Olivine core Fo versus Ni (ppm) of all flow units. Colors of the rinds are as in figures 16 and 21: *ado* – green (population 1) and gray (population 2); *adb* – green (population 1), red (population 2), yellow (population 3), gray (population 4). Source fields and the mantle equilibrium line are taken after Straub et al. (2011). The most forsteritic olivine, from *adb* flow unit, is near equilibrium with a peridotite mantle source.

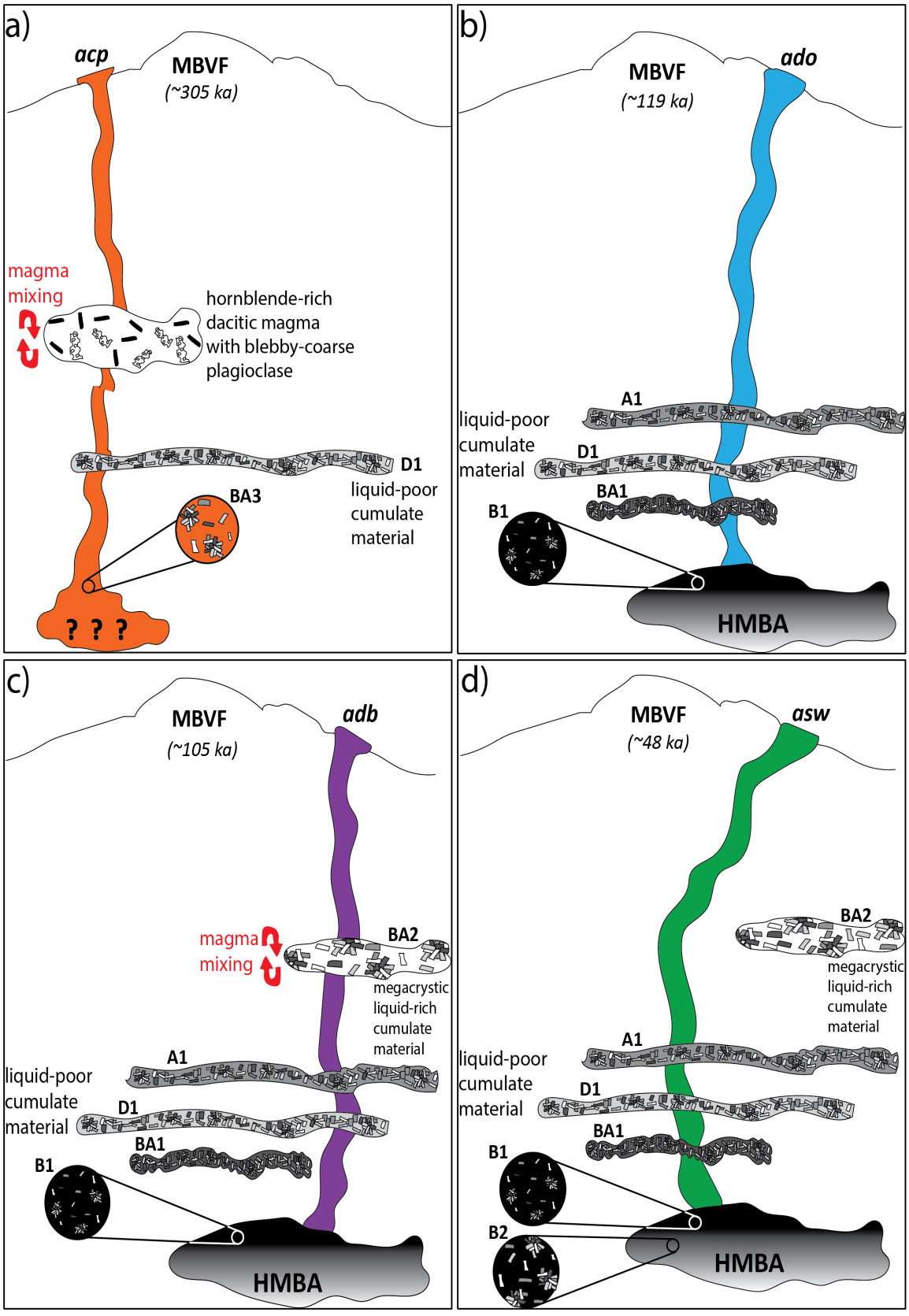
a)
acp
MBVF
(~305 ka)
magma
mixing
hornblende-rich
dacitic magma
with blebby-coarse
plagioclase
D1
liquid-poor
cumulate
material
BA3
? ? ?
b)
MBVF
(~119 ka)
ado
A1
liquid-poor
cumulate
material
D1
BA1
B1
HMBA
c)
MBVF
(~105 ka)
adb
magma
mixing
BA2
megacrystic
liquid-rich
cumulate
material
A1
liquid-poor
cumulate
material
D1
BA1
B1
HMBA
d)
MBVF
(~48 ka)
asw
BA2
megacrystic
liquid-rich
cumulate
material
A1
liquid-poor
cumulate
material
D1
BA1
B1
B2
HMBA

Figure 36 (previous page). Schematic illustration of andesite generation at MBVF from ~305-48 ka. Magmatic cumulate mushes are labeled in accordance to the crystal assemblage they carry and are color coded in accordance to the crystal assemblage (see Table 12). Placement of cumulate mushes relative to each other is based on extent of mineral disequilibrium features and qualitative Al_2O_3 barometry in pyroxenes. For example, magmatic components with high-Al pyroxenes (B1, B2 and BA3) are placed deeper in the crust. The BA1 and D1 assemblage (extensive disequilibrium features) are placed deeper than the A1 and BA2 assemblage (less disequilibrium features). a) Unknown parental magma, supplying BA3 assemblage, ascends and taps D1 magmatic sill before mixing with a hornblende-bearing dacitic chamber to produce the *acp* flow unit. b) HMBA parental magma supplies the B1 assemblage and throughout ascension taps the BA1 and A1 cumulate mushes, as well as the same D1 cumulate mush as *acp*, to produce the *ado* flow unit. c) HMBA parental magma supplies the same B1 assemblage and throughout ascension taps the same series of cumulate mushes as *ado* (BA1, A1 and D1). An additional magmatic component, the BA2 mush, is more liquid-rich and induces magma mixing to produce the *adb* flow unit. d) HMBA parental magma supplies the same B1 assemblage, as well as a crystal clot-rich B2 assemblage. Throughout ascension this magma taps the same series of cumulate mushes (BA1, A1 and D1), with the exception of the BA2 sill, to produce the *asw* flow unit.